Metal-Organic Framework and Covalent Triazine Framework Based Electrocatalysts for the Oxygen Evolution Reaction

Inaugural-Dissertation

zur Erlangung des Doktorgrades

Dr. rer. nat.
der Mathematisch-Naturwissenschaftlichen Fakultät

der Heinrich-Heine-Universität Düsseldorf

vorgelegt von

Seçil Öztürk

aus Eskişehir, Türkei

Düsseldorf, February 2021

aus dem Institut für Anorganische Chemie und Strukturchemie I
der Heinrich-Heine-Universität Düsseldorf

Gedruckt mit der Genehmigung der
Mathematisch-Naturwissenschaftlichen Fakultät der
Heinrich-Heine-Universität Düsseldorf

Referent: Prof. Dr. Christoph Janiak
Korreferent: Prof. Dr. Christian Ganter

Tag der mündlichen Prüfung: 28.05.2021

This cumulative thesis was done from May 2017 to February 2021 at the Heinrich-Heine University of Düsseldorf in the Institut für Anorganische Chemie und Strukturchemie I under the supervision of Prof. Dr. Christoph Janiak.

Publications:

S. Öztürk, Y.-X. Xiao, D. Dietrich, B. Giesen, J. Barthel, J. Ying, X.-Y. Yang and C. Janiak, Nickel nanoparticles supported on a covalent triazine framework as electrocatalyst for oxygen evolution reaction and oxygen reduction reactions

Beilstein J. Nanotechnol. **2020**, *11*, 770–781. DOI: 10.3762/bjnano.11.62

B. Moll, T. Müller, C. Schlüsener, A. Schmitz, P. Brandt, **S. Öztürk** and C. Janiak, Modulated synthesis of thiol-functionalized fcu and hcp UiO-66(Zr) for the removal of silver(I) ions from water

Materials Advances, **2021**, *2*, 804–812 DOI: 10.1039/D0MA00555J

P. Brandt, A. Nuhnen, **S. Öztürk**, G. Kurt, J. Liang and C. Janiak, Comparative evaluation of different MOF and non-MOF porous materials for SO_2 adsorption and separation

Advanced Sustainable Systems, accepted, DOI: 10.1002/adsu.202000285

S. Menzel, S. P. Höfert, **S. Öztürk**, a: Schmitz and C. Janiak, A mixed-valence copper(I/II) coordination polymer directed with a bifunctional soft-hard pyrazolate-carboxylate ligand

Z. Anorg. Allg. Chem., accepted. DOI: 10.1002/zaac.2020000428

S. Öztürk, G. H. Moon, A. Spieß, S. Roitsch, H. Tüysüz and C. Janiak, Highly-efficient oxygen evolution electrocatalyst derived from metal organic framework and ketjenblack carbon material

ChemSusChem, submitted.

J. Liang, V. Gvilava, C. Jansen, **S. Öztürk**, A. Spieß, J. Lin, R. Cao and C. Janiak, One-Pot Shaping: Cucurbituril−Encapsulating Metal−Organic Framework via Mechanochemistry

Angewandte Chemie, submitted.

Eidesstattliche Erklärung

Ich versichere an Eides statt, dass die Dissertation von mir selbstständig und ohne unzulässige fremde Hilfe unter der Beachtung der „Grundsätze zur Sicherung guter wissenschaftlicher Praxis“ an der Heinrich-Heine-Universität Düsseldorf erstellt worden ist. Die aus fremden Quellen direkt oder indirekt übernommenen Gedanken sind als solche kenntlich gemacht. Die Arbeit wurde bisher weder im Inland noch im Ausland in gleicher oder ähnlicher Form einer anderen Prüfungsbehörde vorgelegt. Es wurden keine früheren erfolglosen Promotionsversuche unternommen.

……………………………………. ……………………………………

Ort, Datum Unterschrift

If one day, my words are against science, choose science.

Mustafa Kemal Atatürk (1881-193∞)

Acknowledgments

First of all, I would like to express my deep gratitude to Prof. Dr. Christoph Janiak, for giving me the opportunity to do my doctoral studies in his research group. I am very grateful for his trust and support on this interesting and challenging topic in my dissertation. Furthermore, I thank him for the constructive discussions, corrections of the manuscripts and the great freedom during the entire time of my doctorate. I also would like to thank him for the opportunity to participate in international conferences and seminars and especially for the motivation to learn German.

I would like to thank Prof. Dr. Christian Ganter for being my co-supervisor and for his interest in my seminar presentations.

I would like to thank Claudia Schäfer and Jutta Bourgeois for their great help with all organizational questions. Likewise, I would like to thank Birgit Tommes for the guidance in many student practicals and IR measurements, Anette Ricken for AAS measurements and Marcell Demandt for the technical support.

I thank all AC1 group for their warm welcome, support and friendly atmosphere. I am grateful to a large number of people from the working group. To start with, many thanks to Dr. Dennis Dietrich for his friendly and helpful behavior, motivation while we do sport together, shared knowledge about everything and improving my German. I thank Dr. Sebastian Glomb for his very warm welcoming, giving me the best lab place ever, his support with many things and amazing memories at the inside and outside of the university. I would like to thank Dr. Simon Millan for his help and friendship as well as for teaching me very special German words and culture. A special thank goes to Dr. Alex Nuhnen, Dr. Sebastian Glomb, Dr. Simon Millan, Anna Kautz, Moritz Steinert, Simon-Patrik Höfert and Dr. Beatriz Gil-Hernandez for the best Altstadt parties, funny memories we shared together and nice dinners. I would like to say a big thank Bea Gießen, Dr. Laura Schmolke and Dr. Marvin Siebels for shared lots of fun, celebrations, parties, not forgettable happy times as well as for the support when dealing with problems. You mean so much to me! In addition, I would like to thank Jun Liang, Shang Hua Xing and Yangyang Sun, Philipp Brandt, Alex Spieß and Christian Jansen for many Chinese dinners and lots of fun we had together.

I would like to express my most special thank to my boyfriend Dr. Alex Nuhnen. You are the best thing that happened during this doctorate journey. Thank you for the best memories and for being always by my side when I needed. I am also grateful for our scientific discussions and for you being the best laboratory mate. I may also thank you for enabling me to be more advanced in cooking since I did it for two of us ☺

My greatest thanks go to my beautiful family for their love and constant support. You are the ones that encouraged me and enabled this work to be done. I am grateful to my parents Selcan Öztürk and Mehmet Ali Öztürk because of their trust and belief in me and the financial support that they worked day and night for whenever I needed. Your existence is the most valuable thing in my life. I thank very much my sister Sinem Öztürk Özsu and my brother Serdar Öztürk for being there for me and cheering me up all the time. I am very happy for still being the same kids when we come together. Another special thank goes to my little niece Beren Özsu for the happiness with her existence in our family and for making me smile everytime. I love all of you so much!

En büyük teşekkürümü ise bana olan her daim destekleri ve sevgileri için güzel aileme ediyorum. Beni cesaretlendiren ve bu tezin yazılmasını sağlayan sizlersiniz. Bana olan güveni ve inançları için, her ne zaman ihtiyacım olursa olsun gece gündüz çalışıp bana sağladıkları maddi destekleri için sevgili annem Selcan Öztürk ve sevgili babam Mehmet Ali Öztürk`e minnettarım. Sizin varlığınız benim hayatımdaki en kıymetli şey. Sevgili ablam Sinem Öztürk Özsu ve kardeşim Serdar Öztürk`e her zaman benim yanımda oldukları ve beni neşelendirdikleri için çok teşekkür ederim. Bugün bile biraraya geldiğimizde hala aynı küçük çocuklar olabildiğimiz için çok mutluyum. Özel bir teşekkürümü de ailemizde varlığı ile sağladığı mutluluk ve herdaim beni gülümsettiği için küçük yeğenim Beren Özsu`ya etmek istiyorum. Hepinizi çok seviyorum!

Kıymetli ailem için...

Kurze Zusammenfassung

In der vorliegenden Arbeit wurden kovalente Triazin-basierte Netzwerke (CTFs) und Metall-organische Gerüstverbindungen (MOFs) synthetisiert und charakterisiert, um als Katalysatoren für die elektrochemische Sauerstoffentwicklungsreaktion (OER) untersucht zu werden.

In dem ersten Teil dieser Arbeit lag der Forschungsschwerpunkt auf der Untersuchung von CTF-basierten OER-Katalysatoren. CTFs wurden aufgrund ihrer vorteilhaften Eigenschaften, wie leicht verfügbare und billige Ausgangsmaterialien, einfache Synthese, hohe chemische und thermische Stabilität und große innere Oberfläche ausgewählt. Zunächst wurden die CTF-1 Materialien, ausgehend von 1,4-Dicyanobenzen, über eine Ionothermalsynthese bei 400 °C und 600 °C synthetisiert. Anschließend wurden die CTF-1 Materialien mit unterschiedlichen Mengen an Nickel-Nanopartikeln mittels einer mikrowellenunterstützten Synthese beladen. Die Synthese wurde dabei in einer ionischen Flüssigkeit (IL) durchgeführt, die gleichzeitig als Lösungsmittel und Stabilisator dient. Nach einer gründlichen Charakterisierung der Materialien, wurde deren katalytische Aktivität bezüglich der Sauerstoffentwicklungsreaktion und der Sauerstoffreduktionsreaktion (ORR) untersucht. Unter den getesteten Materialien zeigte das Kompositmaterial Ni/CTF-1-600 die besten Eigenschaften, sowohl für die Sauerstoffentwicklungs- als auch für die Sauerstoffreduktionsreaktion. Um bei der OER eine Stromdichte von 10 mA/cm^2 zu erreichen, wurde eine geringe Überspannung von 374 mV beobachtet, während für die ORR ein Halbwellenpotential von 0.775 V gefunden wurde. Ferner zeigte Ni/CTF-1-600 eine hohe Stabilität bei allen elektrochemischen Prozessen und erreichte eine bessere OER Leistungsfähigkeit als das derzeitige Referenzmaterial RuO_2. Ni/CTF-1-600 ist außerdem der erste in der Literatur beschriebene und gleichzeitig effiziente Ni/CTF Katalysator für die Sauerstoffentwicklungsreaktion.

In einem zweiten Teil wurden MOF-basierte Materialien als mögliche OER Katalysatoren untersucht. MOFs sind aufgrund ihrer positiven Eigenschaften, wie ihrer abstimmbaren Struktur, hoher innerer Oberfläche und einzigartigen Poren/Kanal-Struktur, bereits vielfältig untersucht. Dennoch zeigen reine MOF-Materialien im Hinblick auf eine Anwendung als OER Katalysator auch Nachteile, wie zum Beispiel eine geringe Leitfähigkeit und nur mäßige Stabilität. Zunächst wurde das reine MOF Ni(Fe)-MOF-74 und das Kompositmaterial Ni(Fe)-MOF/KB über eine solvothermale Einptopf-Synthese ausgehend von $Fe(OAc)_2$, $Ni(NO_3)_2{\cdot}6H_2O$, 2,5-Dihydroxyterephthalsäure, und im Fall des Komposits mit dem Kohlenstoff-Material Ketjenblack (KB), in einer $DMF/EtOH/H_2O$ Mischung bei 120 °C über 24 h hergestellt. Die so erhaltenen Materialien wurden charakterisiert und bezüglich ihrer Leistungsfähigkeit für die elektrochemische Sauerstoffentwicklungsreaktion untersucht. Ni(Fe)-MOF/KB zeigte eine außerordentlich gute

OER Leistung, da lediglich eine Überspannung von 274 mV benötigt wurde, um eine Stromdichte von 10 mA/cm^2 zu erreichen. Des Weiteren wurde eine geringe Tafel-Steigung von 40.4 mV/dec beobachtet. Ferner zeigte Ni(Fe)-MOF/KB die höchste Stromdichte von 650 mA/cm^2 bei einer angelegten Spannung von 1.7 V_{RHE}. Zusammenfassend konnte durch die Kombination des leitfähigen und hochporösen Ketjenblack die geringe Leitfähigkeit des MOFs verbessert werden und überzeugende Ergebnisse im Bereich der OER erreicht werden. Auch hier wurde zum ersten Mal in der Literatur ein MOF/KB Komposit erfolgreich für die elektrochemische Sauerstoffentwicklungsreaktion verwendet.

Short Summary

In this thesis, the synthesis and characterization of covalent-triazine framework (CTF) and metal-organic framework (MOF) based materials are studied to develop efficient catalysts for electrochemical oxygen evolution reaction (OER).

In the first part, research focus was on the investigation of OER catalysts that are based on CTFs due to their advantages like readily available cheap starting materials, easy synthesis, high chemical and thermal stability and high surface areas. First, CTF-1 materials are synthesized from 1,4-dicyanobenzene at 400 °C and 600 °C via ionothermal method. Following, different amounts of nickel nanoparticles were supported on CTF-1 materials by rapid microwave-assisted synthesis in the ionic liquid (IL). After in depth characterization of the materials, the electrocatalytic activity towards oxygen evolution reaction and oxygen reduction reaction (ORR) were tested. Among them, Ni/CTF-1-600 showed the best performance for both OER, by requiring 374 mV to reach a current density of 10 mA/cm^2, and ORR displaying a half-wave potential of 0.775 V. Ni/CTF-1-600 showed also high stability and even better OER performance than the benchmark RuO_2 catalyst. It was also first time in the literature that a Ni/CTF catalyst was investigated for OER and found to be a highly efficient catalyst.

In the second part, MOF-based materials are investigated as OER electrocatalysts. MOFs are in focus for OER owing to their tunable structure and compositions, high surface area and unique pore/channel structures. Nevertheless, pristine MOFs have issues of low electric conductivity and stability. The pristine Ni(Fe)-MOF-74 and the Ni(Fe)-MOF/KB composite are prepared via one-step solvothermal method from $Fe(OAc)_2$, $Ni(NO_3)_2 \cdot 6H_2O$, 2,5-dihydroxyterephthalic acid and in the case of the composite with the carbon material ketjenblack (KB) in a DMF/EtOH/H_2O mixed solution at 120 °C for 24 h. The synthesized Ni(Fe)-MOF/KB composite as well as pristine Ni(Fe)-MOF-74 are characterized and tested for electrochemical OER. Ni(Fe)-MOF/KB showed a remarkable OER performance by requiring only 274 mV to reach a current density of 10 mA/cm^2 and a small Tafel slope of 40.4 mV/dec. It also displayed the highest current density of 650 mA/cm^2 at an applied voltage of 1.7 V_{RHE}. As a result, the strategy of combining the conductive and porous ketjenblack and a poor conductive MOF to get better OER performance was found very advantageous. With this research, the first example of a MOF/KB composite as an efficient OER electrocatalyst has been elucidated in the literature.

List of abbreviations and symbols

Å	Ångstrøm
a.u.	Arbitrary unit
AAS	Atomic absorption spectrometry
1,4-DCB	Dicyano benzene
BET	Brunauer-Emmett-Teller
°C	Degree Celsius
Calc.	Calculated
cm	Centimeter
CNT(s)	Carbon nanotube(s)
COF	Covalent organic framework
CTF	Covalent triazine framework
DMF	*N,N'-Dimethylformamide*
EDX	Energy-dispersive X-ray spectroscopy
Fig.	Figure
FT-IR	Fourier transform infrared
g	Gram
h	Hour
HR-TEM	High-resolution transmission electron microscopy
IL(s)	Ionic Liquid(s)
IUPAC	International Union of Pure and Applied Chemistry
j	Current density
K	Degree Kelvin
L	Liter
mg	Milligram

min	Minute
mL	Milliliter
MOF	Metal-organic framework
η	Overpotential
nm	Nanometer(s)
PXRD	Powder X-ray diffraction
RHE	Reversible hydrogen electrode
SBU	Secondary building unit
SEM	Scanning electron microscopy
STEM	Scanning transmission electron microscopy
TEM	Transmission electron microscopy
TGA	Thermogravimetric analysis
wt%	Weight percentage
XPS	X-ray photoelectron microscopy
θ	Theta, angle of diffracted wave in the Bragg's equation

Contents

1.Introduction

1.1 Solar Energy

Global energy demand due to the growing population and economy is continuously increasing in the last decades. Fossil fuels supply the biggest part of world`s energy consumption. Nevertheless, depletion of fossil fuel sources and arising environmental issues related to their consumption requires the development of sustainable, clean energy. Amongst all alternative energy sources, solar energy has the largest potential by being the most abundant clean energy source available with a 10^4 times higher capasity than the current world energy consumption.[1] Consequently, utilizing a fraction of the solar energy can provide an important improvement for energy problems.

In order to utilize the solar energy, it needs to be harnessed in forms such as chemicals, fuels or electricity. Some of the possible ways are solar thermal systems, photovoltaics and solar fuels. In solar thermal systems, sunlight radiation is converted to thermal or electrical energy for some heating applications. Photovoltaics, which are readily commercialized, can transform the solar energy into electricity, but the electrical energy cannot be stored as such. Solar fuels enable the storage of the solar energy into chemical bonds of molecules making them an alternative to fossil fuels. The solar fuels can be produced through different reactions such as photochemical, thermochemical, electrochemical or artificial photosynthesis. In artificial photosynthesis there are two general pathways to convert solar energy into chemical energy that are stored in hydrogen or hydrocarbons, namely photocatalytic water splitting and carbon dioxide (CO_2) reduction.[2,3] In CO_2 reduction, CO, methanol and other carbonaceous molecules are obtained as fuels. On the other hand, in water splitting, hydrogen is obtained as fuel.

1.1.1 Water Splitting

Overall water splitting into molecular oxygen and hydrogen is an uphill reaction where the solar energy can be stored in the chemical bond of hydrogen[4].

$$H_2O \rightarrow H_2 + 1/2O_2 \qquad \Delta G° = 237.2\ \text{kJ mol}^{-1}$$

Water splitting consists of two half reactions: anodic oxygen evolution reaction (OER) and cathodic hydrogen evolution reaction (HER) which requires a source of energy such as light or electricity. Between both reactions water oxidation is considered as the major bottleneck which obstruct the progress in storable fuels since it requires a four electron transfer and an oxygen-oxygen bond formation. This half reaction requires an extra bias of 1.23 V vs. Reference Hydrogen Electrode (RHE).

$2\,H^+ + 2\,e^- \rightarrow H_2$ $\qquad E^\circ = 0$ V vs. RHE

$2\,H_2O \rightarrow O_2 + 4H^+ + 4\,e^-$ $\qquad E^\circ = 1.23$ V vs. RHE

Beyond this thermodynamically required value, an extra potential (overpotential) needs to be applied for fuel production. Therefore, efficient water splitting is only possible by lowering the overpotential required for OER via catalysts. For this reason, many research efforts are being made to develop catalysts that enable this uphill process at the potentials close to the thermodynamic limit. Potential OER catalysts should have fast reaction rate, small overpotential, corrosion resistance, long term stability and low fabrication cost.

1.1.1.1 Electrochemical Water Splitting

Electrochemical water splitting (electrolysis of water) process was introduced in 1789 by Van Troostwijk and Deiman in Europa.[5] In early decades of the 20th century, water electrolysis was industrialized and later in the 20th century improvements resulted with more than 50% efficiency of electrolyzers.[6] This electrochemical process is splitting water into hydrogen and oxygen under applied external bias (electric voltage). In Figure 1, a typical electrochemical cell is shown, where an electrical power source is connected to the cathode and anode. Oxidation reaction occurs at the anode where the oxygen gas is generated and reduction reaction occurs at the cathode where the hydrogen gas is formed. The water splitting reactions in acidic and alkaline media are given in Table 1.

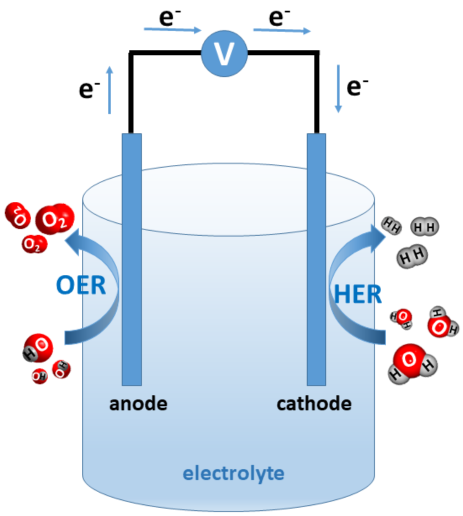

Figure 1. Schematic illustration of a typical electrochemical cell.

Table 1. HER and OER reactions in acidic and alkaline media.

	Acidic media	Alkaline media
Hydrogen Evolution Reaction (HER) at cathode	$4\ H^+(aq) + 4\ e^- \rightarrow 2H_2(g)$	$4H_2O(l) + 4\ e^- \rightarrow 2H_2(g) + 4OH^-(aq)$
Oxygen Evolution Reaction (OER) at anode	$2H_2O(l) \rightarrow O_2(g) + 4H^+(aq) + 4e^-$	$4OH^-(aq) \rightarrow O_2(g) + 4e^- + 2H_2O(l)$

In theory, in order to split water, we need a voltage difference of 1.23 V between the anode and cathode. Nevertheless, the practically required potential is significantly higher than the thermodynamic equilibrium potential due to surpassing the kinetic barrier and excess energy that is required to overcome the electrolyte resistance. The difference between the potential that we need to practically apply to split water and the theoretical potential is called as the overpotential (η). Targeting the reduced energy input to drive the water splitting, the overpotential needs to be decreased as much as possible by using the catalysts. Additionally, cell design optimization can minimize the resistance loss. When we study the performance of a catalyst for one of the half reactions with potentiostat, pH is an important parameter which can change the potential value needs to be applied for that half reaction. Consequently, the measured potential is often given referred to Reversible Hydrogen Electrode (RHE) where the redox event can be compared with the standard reduction potential of hydrogen regardless of the pH.

1.1.1.2. Oxygen Evolution Reaction

Oxygen evolution reaction consists of four electron-proton reactions that occur at the catalyst surface and results in the formation of gaseous oxygen. Different mechanisms of OER are proposed for acidic and alkaline conditions[7]. OER mechanism under acidic conditions starts with the water binding to the surface resulting in hydroxide formation by removal of one proton and one electron, whereas a binding of hydroxide ion with a one electron oxidation is the first step in alkaline media. Both mechanisms involve several steps with intermediates and results with oxygen-oxygen bond formation at the end. The proposed mechanisms for acidic and alkaline media is as follows:

In acidic conditions;

$H_2O + * \rightarrow HO^* + e^- + H^+$

$HO^* + H_2O \rightarrow O^* + H_2O + e^- + H^+$

$O^* + H_2O \rightarrow HOO^* + e^- + H^+$

$HOO^* \rightarrow {}^* + O_2 + e^- + H^+$

In alkaline conditions;

$OH^- + * \rightarrow HO^* + e^-$

$HO^* + OH^- \rightarrow O^* + H_2O + e^-$

$O^* + OH^- \rightarrow HOO^* + e^-$

$HOO^* + OH^- \rightarrow * + O_2 + H_2O + e^-$

The $*$ represents the active sites at the catalyst surface.

Despite the fact that the mechanisms of OER is still discussed, the reaction thought to be occur on the active sites via intermediates such as O^*, HO^*, HOO^*. Therefore, M-O bond strength is highly important for the overall electrocatalytic ability. The formation of the oxygen molecule necessitates transfer of four protons and multi-step reactions occur with a single electron transfer at each step during the OER. Therefore, OER kinetics are very sluggish due to the accumulation of energy at each step. An efficient OER catalyst can lower the kinetic barriers and consequently increase the rates of oxygen production. The OER catalyst ideally should have low overpotential, high stability. Also, it should be earth abundance and low in cost in order to produce hydrogen at industrial scale. Precious metal oxides such as RuO_2 and IrO_2 are the most efficient electrocatalysts for OER.[8,9] However, utilizing such less abundant precious metals increases the cost of hydrogen production and hinders the productivity on a large scale. Development of efficient, stable, low cost and abundant OER catalysts is hence a continuously ongoing hot topic. Up to know, large number of OER catalysts have been developed such as noble-metal[10,11] and earth-abundant metal based[12,13] or carbon based materials.[1415] Among these alternatives, 3d transition metal oxides[16,17], hydroxides[18] and mixed metal oxides[19] are substantially investigated and performed competitive electrochemical activities. Metal organic frameworks (MOFs) and covalent triazine frameworks (CTFs) are some of the potential candidates for OER catalysts and will be discussed in the following sections.

To evaluate the performance of the OER catalysts in lab scale, three-electrode systems equipped with a rotating disc electrode are largely used. As seen in Figure 2, three-electrode configuration consists of reference electrode (e. g. Ag/AgCl), counter electrode (e. g. Pt wire) and working electrode (e. g. glassy carbon electrode coated with ink of catalyst) which are connected to a potentiostat.

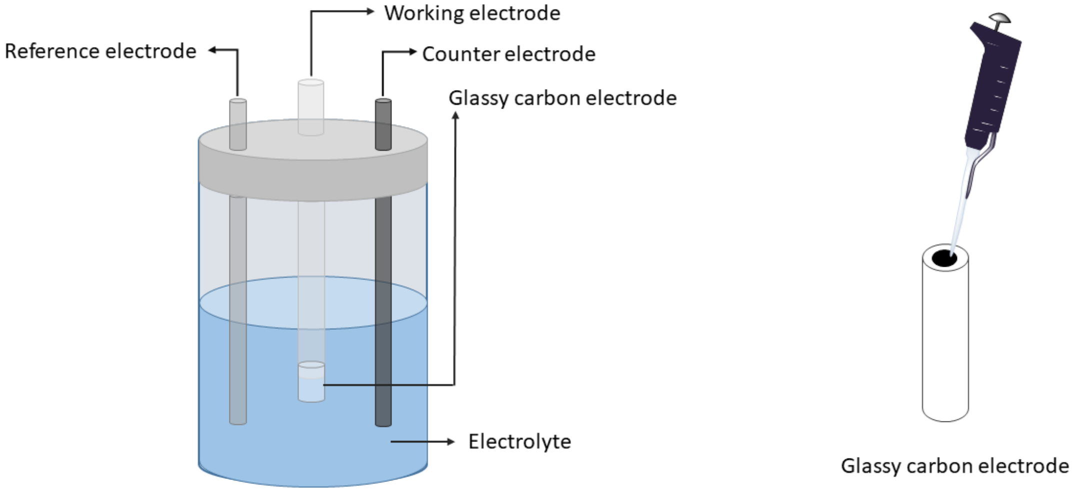

Figure 2. Schematic illustration of a standard three electrode configuration cell (left) and drop casting of the catalyst onto glassy carbon electrode (right).

The potential of the working electrode is measured with respect to the reference electrode while the current flows between working electrode and counter electrode simultaneously. Generally, for acidic media H_2SO_4 and for alkaline media KOH electrolyte solutions are used. During the measurement, the nitrogen or argon gas flow is purged through the cell to remove oxygen and other gases. The rotation of the working electrode is important for the removal of the gaseous products in order to prevent bubble accumulation which is formed during the reaction on the electrode surface. To guarantee a close to isothermal working temperature, water circulation systems can be used to maintain a constant temperature. To investigate the activity of the catalyst, a polarization scan or cyclic voltammogram is conducted.

1.1.1.3 Evaluation Parameters for OER Catalysts

Following, several parameters and terms that are used to evaluate the performance of electrocatalysts will be discussed. First, the overpotential (η) is one of the most referred descriptor for the evaluation of an OER electrocatalyst. As described before, the overpotential is the potential difference between the applied potential and the potential under equilibrium conditions to drive a specific reaction. According to Nernst equation[20], the applied potential (E, Formula 1) is given as:

$$E = E^{0'} + \frac{RT}{nF} ln \frac{C_{Ox}}{C_{Red}} \tag{1}$$

$E^{0'}$ is the formal potential of the overall reaction, R is the ideal gas constant, T is the temperature, n is the number of electrons transferred in the reaction, F is the Faraday constant and C_{Ox} and C_{Red} are the concentrations of the oxidized ad reduced reagents, respectively. The overpotential (η, 2) can be defined as follows:

$$\eta = E - E_{eq} \tag{2}$$

where E_{eq} stands for potential under equilibrium conditions. Generally, the overpotential is a value that has to be applied to achieve a specific current density. According to the 10% solar to fuel efficiency a current density of 10 mA/cm^2 is required and the overpotential to reach this value is the general key parameter for the performance of OER electrocatalyst. Consequently, a lower overpotential of an electrocatalyst in a system defines better electrocatalytic activity for the desired reaction.

Next, Tafel analysis is another primary study for the performance evaluation. For an electrical interface, the relationship between current and the overpotential is given by the Butler-Volmer equation (3)[21] as follows:

$$j = j_0\left(e^{\frac{\alpha_A nF}{RT} \times \eta} + e^{\frac{\alpha_C nF}{RT} \times \eta}\right) \tag{3}$$

j is the current, j_0 is the current at equilibrium potential (exchange current), α_A and α_C are the charge transfer coefficients for anodic and cathodic reactions respectively, n is the number of electrons transferred, F is Faraday constant, R is the ideal gas constant, T is the temperature in K and η is the overpotential. Under high overpotential conditions, Butler-Volmer equation will give the Tafel equations of the cathodic (4) and anodic polarization (5) as follows, respectively[22]:

$$ln\, j = ln j_0 + (-a_C nF/RT)\,\eta \tag{4}$$

$$ln\, j = ln j_0 + (a_A nF/RT)\eta \tag{5}$$

These equations can be written as y = b + mx and when log *j* is plotted vs. η, it will give a linear line called Tafel plot. Tafel slope of the cathodic (6) and anodic polarizations (7) would be as follows:

Tafel slope for cathodic reaction = $2.303\ RT/{-a_C nF}$ (6)

Tafel slope for anodic reaction =$2.303\ RT/a_A nF$ (7)

Tafel slope is inversely related to the charge transfer coefficient (α) and gives the information of how fast the current increases against overpotential. Specifically, the smaller the Tafel slope, the faster the charge transfer reaction occurs across the electrocatalytic interface which indicates good electrocatalytic kinetics. Additionally, Tafel slope also provides information about the mechanistic pathway of the reaction under study. Consequently, Tafel analysis is an important parameter for the evaluation of the OER catalysts to understand the reaction kinetics and mechanism and compare the catalytic activity of different catalysts.

Another important parameter is the stability of the catalyst. Obviously, a catalyst needs to be stable to be applicable in industry. Stability of a material is generally measured either by controlled current electrolysis or by chronoamperometric measurements. The catalyst that shows stability and constant performance either for the voltage to deliver a relative current density (10 mA/cm^2) or for the current density to achieve a relative voltage potential for more than 10 hours is accepted as a stable catalyst. The stability issue of a catalyst can be due to various factors such as the nature of the working electrode and electrolyte, leaching of the active sites, blocking of the active sites because of bubble accumulation occurring even at high rotation speeds or detachment of the catalyst. The used binder to anchor the catalytic material onto desired substrate, catalyst ink preparation and drying process are other important points that has great effect on the stability.

The turnover frequency (TOF, 8) can be defined as the number of reactants that get converted to the desired product per catalytic site per unit of time. It can be calculated as

$$TOF = (j * A)/(4 * F * n) \tag{8}$$

j is the current density, *A* is the working electrode area, *F* is the Faraday constant and *n* is the mol number of the active material. However, it is very hard to get exact TOF numbers since not all the catalytic sites are equally easily accessible in the material. Still, this parameter is useful for the comparison of similar catalytic materials[23].

1.2 Porous Materials

Pores are defined as the cavities or channels within or close to the surface of a solid which are deeper than they are wide and the porosity of a material is the ratio of the pore space volume to the material volume. The internal surface area of a material is defined by these pores that are classified by IUPAC according to their diameters as micropores (<2 nm), mesopores (2–50 nm) and macropores (>50 nm)[24]. The term nanoporous material is used for materials that posses pore size in a range up to 100 nm. Nanoporous materials are promising materials for a wide range of applications owing to their unique properties such as divers pore structure, high surface area, etc[25]. Porous organic polymers (POPs), specifically covalent triazine frameworks and metal-organic frameworks are categorized in the nanoporous materials classification and have an important place in many applications which will be discussed in detail in the following sections.

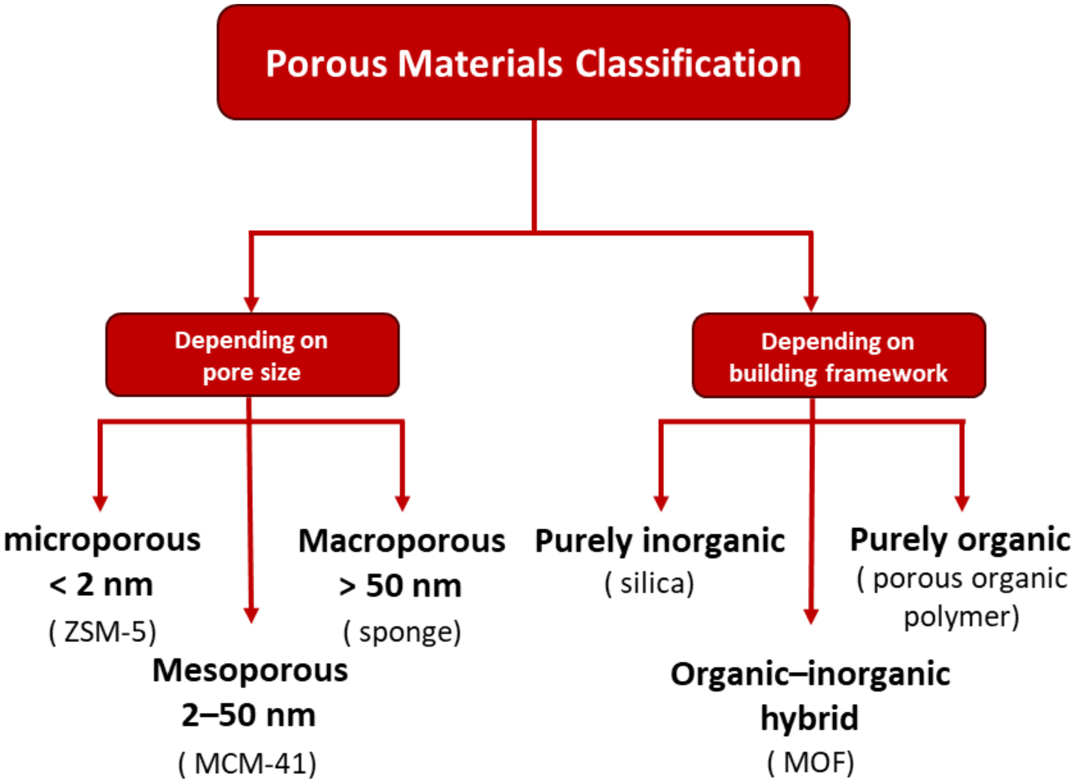

Figure 3. Classification of porous materials.

1.2.1 Porous Organic Polymers

Porous organic polymers are a class of multi-dimensional porous network materials which have covalently bonded, thermally stable backbones. POPs have great potential for applications in gas storage/separation[26,27], catalysis[28], energy conversion[29] or sensing[30] owing to their porosity, tunable pore structure, high surface area, high physicochemical stability and chemical tunability for targeted application. They consist entirely of lighter elements of the periodic table such B, C, N, O which results in low density materials with high physical and chemical stability. Additionally, they possess high specific surface areas up to 6400 m^2/g [31] and their porosity can be designed by choosing appropriate monomers[32]. Bottom-up approach for POP synthesis enables to engineer their physical and chemical properties[33]. POPs are generally divided into two categories as crystalline or amorphous according to their morphology[34]. Covalent organic frameworks (COFs)[35,36] are crystalline POPs, whereas covalent triazine frameworks (CTFs)[37], conjugated microporous polymers (CMPs)[38], porous polymer networks (PPNs)[31], porous aromatic frameworks (PAFs)[39], hypercrosslinked organic polymers (HCPs)[40] are some of mostly amorphous POPs.

1.2.1.1 Covalent Triazine Frameworks

Covalent triazine frameworks are nanoporous polymers within in the subclass of POP materials. CTFs are formed by the trimerization and subsequent oligomerization of aromatic nitriles with a catalyst. Origin of CTFs is based on 1962 when it is found that 1,3,5-triazines can be obtained from aromatic mono-nitriles at elevated temperatures in the presence of metal salt catalyst[41]. Miller extended this approach in 1973 and synthesized highly crosslinked and stable polymers with a variety of aromatic nitriles[42]. However, CTFs had their scientific breakthrough only in 2008 when Kuhn, Antonietti and Thomas reported the synthesis of CTFs by ionothermal method[37]. Since then, CTF materials are continued to be investigated as promising materials for applications such as gas storage and separation, heterogeneous catalysis, energy conversion etc[43]. The wide choice of monomers with different aromatic structure elements enables for great variety in the properties of the CTF polymer such as pore size and shape, surface area, nitrogen and heteroatom content[43].

In addition to ionothermal method, there are other synthetic routes for the CTF formation such as Brønsted acid route, Friedel-Crafts reaction, phosphorous pentoxide (P_2O_5) catalyzed method and so on[44]. The first CTF was, as described above, synthesized via ionothermal method[37]. In ionothermal method, molten $ZnCl_2$ acts as a Lewis acid catalyst and the solvent (porogen) at 400-700 °C for the trimerization of aromatic nitriles. Due to the hygroscopic properties of monomer and $ZnCl_2$, sublimation of aromatic nitriles and to keep the stoichiometry of monomer with respect to $ZnCl_2$ stable, the reaction is conducted in sealed ampoules under inert conditions. Typically, desired molar ratios of monomer and $ZnCl_2$ are transferred into an ampoule under inert conditions, then evacuated under vacuum, flame-sealed and consequently heated to 400 °C for 40-48h. High synthesis temperatures result in a substantial degree of carbonization. This can be indicated with increasing C/N and C/H ratios compared to ideal values and concomitant by increasing porosity with a possible structure loss[45]. The products of this method are black and therefore destructive for photocatalytic applications. Other disadvantages of ionothermal method are the long reaction time (>40h) and difficult removal of $ZnCl_2$ residuals from the framework. The porosity and surface area of the formed CTFs depend on reaction temperature, time and the amount of $ZnCl_2$ in respect to the aromatic nitrile monomer[37,45]. CTFs are mostly amorphous materials. The crystallinity of CTF depends to high extent on the monomer planarity or linear arrangement of the nitrile functionalities that provide a long-range order. Additionally, high reaction temperature and increasing $ZnCl_2$ to monomer ratios lead to amorphous but porous materials. In Brønsted acid route, trifluoromethane sulfonic acid is employed as a catalyst for the trimerization of aromatic nitriles. This method displays advantages such as mild reaction conditions at room temperature and ambient pressure conditions, no carbonization and photoactive materials[46]. However, the high cost of catalyst, lower activity towards heteroatomic nitrile monomers are some of the disadvantages of this method. In Friedel- Crafts reaction route, CTF materials can be synthesized by Friedel- Crafts reaction of aromatic building blocks and cyanuric chloride[47]. This method offers the advantages of simple, inexpensive, non-toxic, low reaction temperature and facile synthetic conditions. In high temperature phosphorous pentoxide catalyzed method, P_2O_5 is used to synthesize CTFs by direct condensation of primary aromatic groups into s-triazine rings[48]. This route is eco-friendly, applicable to a big variety of monomers and easy to get rid of from residuals in the catalyst. Nevertheless, the temperature of the synthesis is high and lead to carbonization as in ionothermal method.

One of the first synthesized CTFs, CTF-1 was prepared by ionothermal method via polytrimerization of 1,4-dicyanobenzene in molten $ZnCl_2$[37]. Schematic illustration of the synthesis and idealized structure of CTF-1 can be seen in Fig. 4.

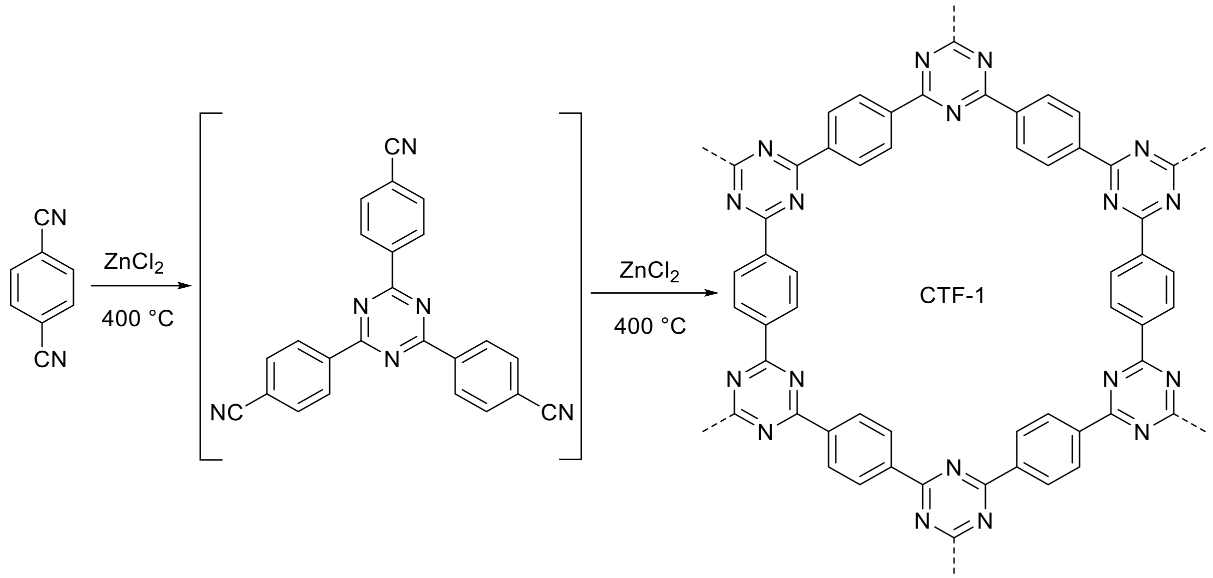

Figure 4. Schematic illustration of idealized structure of CTF-1 synthesized by ionothermal method via trimerization of 1,4-dicyanobenzene in molten $ZnCl_2$.

This resulted CTF-1 has a hexagonal packing of pores with a layered structure and interlayer distance of 3.4 Å. Here, a low $ZnCl_2$/ monomer ratio (1:1) resulted in a crystalline CTF-1. In this study, the effect of temperature and different $ZnCl_2$/ monomer ratios on the structural parameters were demonstrated. Surface area and pore volume of CTF are tunable and by increasing temperature or $ZnCl_2$/ monomer ratio, higher surface area and pore volume were obtained[45,49]. In the pore size distribution, a shift toward mesopore range without affecting the micropores is observed. At higher temperatures, irreversible reactions take place such as carbonization and decomposition which is resulted in nitrogen loss and higher porosity[45]. This observation was confirmed by elemental analysis where a rise in molar ratios of C/N and C/H with increasing temperatures was observed. Furthermore, XPS studies revealed the formation of various nitrogen configurations and change in the amounts of nitrogen moieties in the material. Increasing the synthesis temperatures resulted in additional nitrogen configurations different than pyridinic nitrogen which is expected for triazine moieties and in increased pyrrolic and quaternary nitrogen content related to the carbonization[50]. Therefore, such CTF materials can be described as amorphous triazine frameworks or N-doped carbon materials if synthesis temperatures above 400 °C are applied. Nevertheless, most CTF materials are thermally stable up to 400 °C and chemically stable under strong acidic or basic conditions.

Since 2008, several monomers with varying aromatic structures have been used for the synthesis of CTF and gave a broad range of materials with different application possibilities (Figure 5).

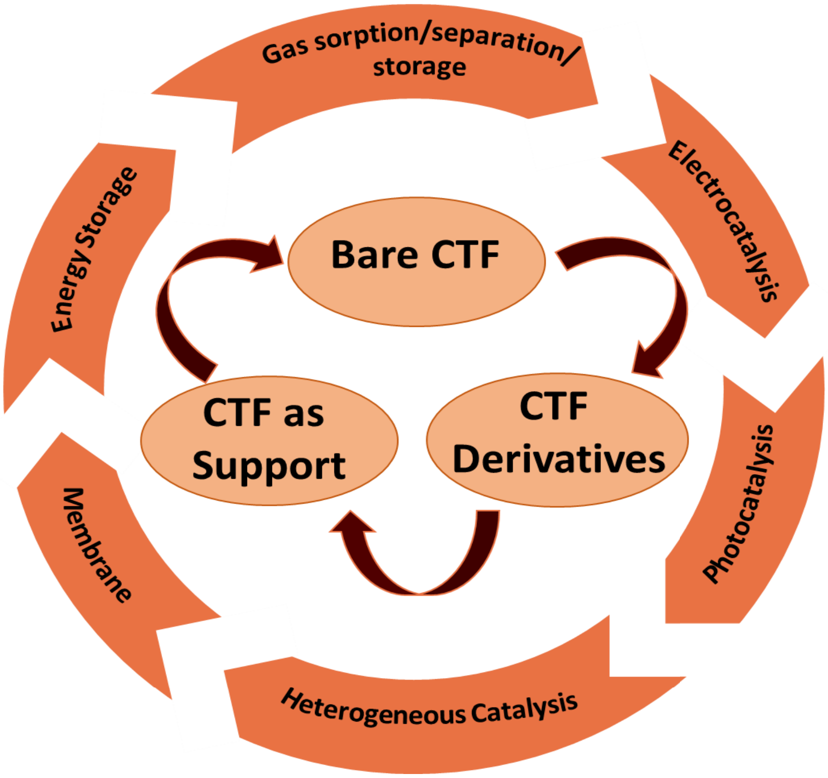

Figure 5. Application areas of CTF and CTF based catalysts.

CTFs are widely investigated for gas sorption and separation processes especially for carbon dioxide[51,52,53,54], methane[53,54] and hydrogen adsorption capacities[37,53,54,55]. CTFs were also utilized for adsorption of dyes[56], aromatic compounds[57], and surfactants[58], for sensing[59], in membranes[60], as battery materials[61] and for energy storage[62]. A major application area of CTFs is catalysis where they can be used either as catalyst themselves or as support for the catalytically active metal species. CTF was used as a direct metal free catalyst first time for the conversion of CO_2 to organic carbonates[63]. Here, the higher nitrogen content and mesoporosity resulted in the most active materials. Bare CTF materials are also widely used in photocatalysis such as water splitting[64], hydrogen evolution[65,66,67], solar fuel production[68] and photodegradation of methylene blue[69]. Another application area of bare CTFs is electrocatalysis where there are already studies on oxygen reduction reaction[50,70,71], oxygen evolution reaction[72], reduction of nitrobenzene[72] and CO_2 conversion[73]. On the other side, CTFs are also good candidates as a support for active metal species or molecular complexes, owing to their high nitrogen content, thermal and chemical stability, porosity and specific surface area. One of the pioneer work was done by Palkovits et. al. when they investigated the Pt-CTF catalyst showing high activity and high stability for low-temperature oxidation of methane to methanol[74]. Bipyridyl structure units in the CTF support enabled the coordination of Pt (II) species and the consequent catalyst showed stable activity over several turnover numbers. Hug et. al. further demonstrated the capability of the bipyridine units in CTF to coordinate various metals including palladium, platinum, copper and nickel[75]. The advantage of using CTF as a support for Pd nanoparticles over activated carbon was demonstrated by Chan-Thaw et. al[76]. This study showed that the N-heterocyclic moieties on the CTF surface are beneficial for improved stability of Pd nanoparticles during the liquid phase glycerol oxidation. Pd/CTF showed better activity and stability than typical Pd/activated carbon. Siebels et. al. showed the higher electrochemical activity of Rh@CTF-1 than commercial Pt/C for hydrogen evolution reaction[77]. In another study, Pt-modified CTF exhibited selective activity for electrochemical oxygen reduction reaction even in the presence of methanol which showed the possibility to be a potential cathode catalyst in direct methanol fuel cells[78]. The same group also studied Cu-modified CTF for electrochemical oxygen reduction reaction as more abundant and less expensive alternative catalysts. This catalyst showed lower activity compared to conventional Pt/C for ORR, but it showed the best performance among Cu based electrocatalyst reported until that time[79]. Hierarchically porous FeNC catalyst was produced via impregnation of an iron precursor into CTF and subsequent calcination under inert conditions at 800-1000 °C (Figure 6)[80]. FeNC calcined at 900 °C showed the best ORR activity and outperformed the benchmark Pt/C catalyst. The high catalytic activity of this material depends mostly on the existence of graphitic nitrogen and FeN_x species together.

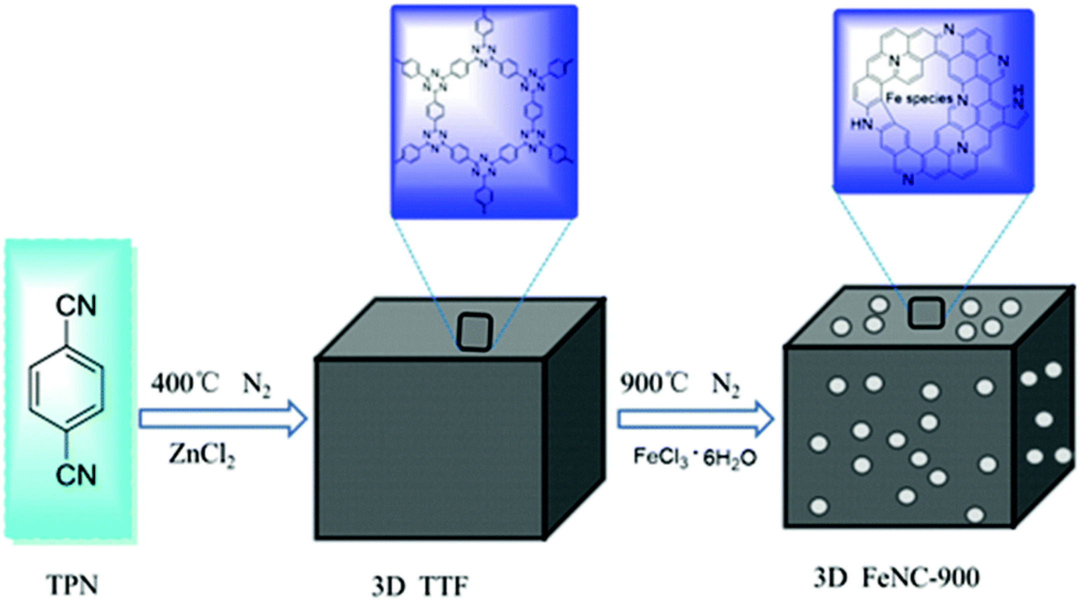

Figure 6. Schematic illustration of FeNC-900 synthesis. Reprinted from the ref 80, Copyright 2016, with the permission of The Royal Society of Chemistry (RSC).

1.2.1.2 Metal-Organic Frameworks

Metal organic frameworks (also referred as porous coordination polymers) are hybrid materials constructed from metal based inorganic secondary building units (SBUs or nodes) and organic linkers. According to the defined terminology by IUPAC in 2013, the following definition for a MOF is recommended[81]:

“A metal–organic framework, abbreviated to MOF, is a coordination network with organic ligands containing potential voids.”

Considering the origin of MOFs, MOF is a subset of a coordination network and a coordination network is a subset of a coordination polymer[81]. They are built up by metal nodes that are linked with organic ligands via coordination bonds (Figure 7)[82].

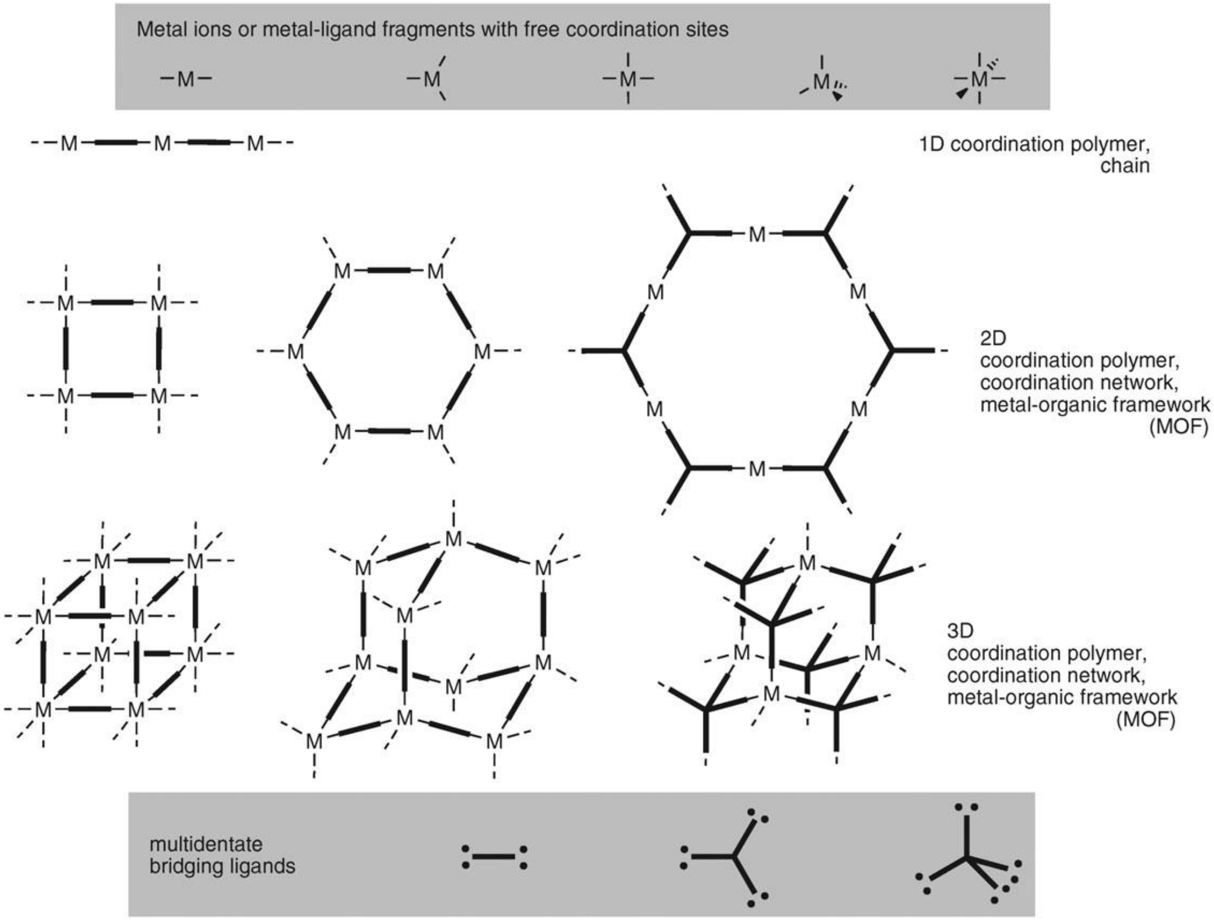

Figure 7. Schematic illustration of the construction of coordination polymers, coordination networks and metal organic frameworks. Reprinted from ref. 82, Copyright 2010, with permission of The Royal Society of Chemistry (RSC).

Hoskins and Robson had an important influence on the development of the coordination polymer chemistry in the 1990`s. They showed the construction of structures with particular topologies through the use of metals and ligands with appropriate coordination geometries[83,84]. Since then, this class of materials continued to be more studied and led to the investigation of new generation MOF materials. The term metal–organic framework was first used by Yaghi et al. in 1995 when they introduced the crystalline $[Cu(I)(4,4'\text{-}Bipy)_{1,5}NO_3]\cdot(H_2O)_{1,25}$ framework with an extended channel system and non-permanent microporosity[85]. In 1997, Kitagawa reported the first permanently porous framework $Co_2(bipy)_3(NO_3)_4$ which could reversibly adsorb the non-polar gases (N_2, O_2 and CH_4) in the framework[86]. Two years later, two very-well known MOFs, namely HKUST-1 ($Cu_3(btc)_2$, btc= 1,3,5-benzenetricarboxylate) and MOF-5 ($Zn_4O(bdc)_3$, bdc= 1,4-benzenedicarboxylicacid) were synthesized[87,88]. These MOFs led to the rapid development of further highly porous networks. The abundance of available metal ions or clusters combined with almost infinite possible organic linkers offer huge variety of MOFs and enable the control of their topology. MOFs have outstanding properties such as crystallinity, porosity, in particular uniform micro-/mesopore structures with high surface areas up to 6000 m^2/g[89], tunable pore sizes and topologies[90,91,92]. They can exhibit flexible structures in a response to external stimuli such as temperature, pressure or guest molecules[93]. All these properties show the advantages of MOFs compared to other porous materials like zeolites or activated carbon which make them potential candidates in a big variety of applications.

MOFs are typically synthesized via hydro/solvo-thermal methods. In addition, microwave-assisted, electrochemical, mechanochemical and sonochemical synthesis methods are widely used (Figure 8)[94]. In addition, the choice of metal salt and linker, the synthesis method and conditions have great influence on the final MOF structure and morphology. In traditional hydrothermal (water as solvent) and solvothermal (organic solvent) MOF synthesis, the reaction is carried out in an autoclave (gas-tight closed vessel) at autogenous pressure that enables to work above the boiling point of the solvent used. The reaction of a metal salt with the organic molecules in suitable solvents inside an autoclave at elevated temperatures leads to the as synthesized (as) MOF which contains the solvent molecules inside the framework. These solvent/guest molecules inside the pore cavity of the as synthesized MOF need to be removed by an activation process. The most used method of activation is the replacement of high-boiling solvent molecules by volatile solvents, followed by thermal activation under vacuum. In this way, the void space of the pore of so-called activated MOF is made accessible.

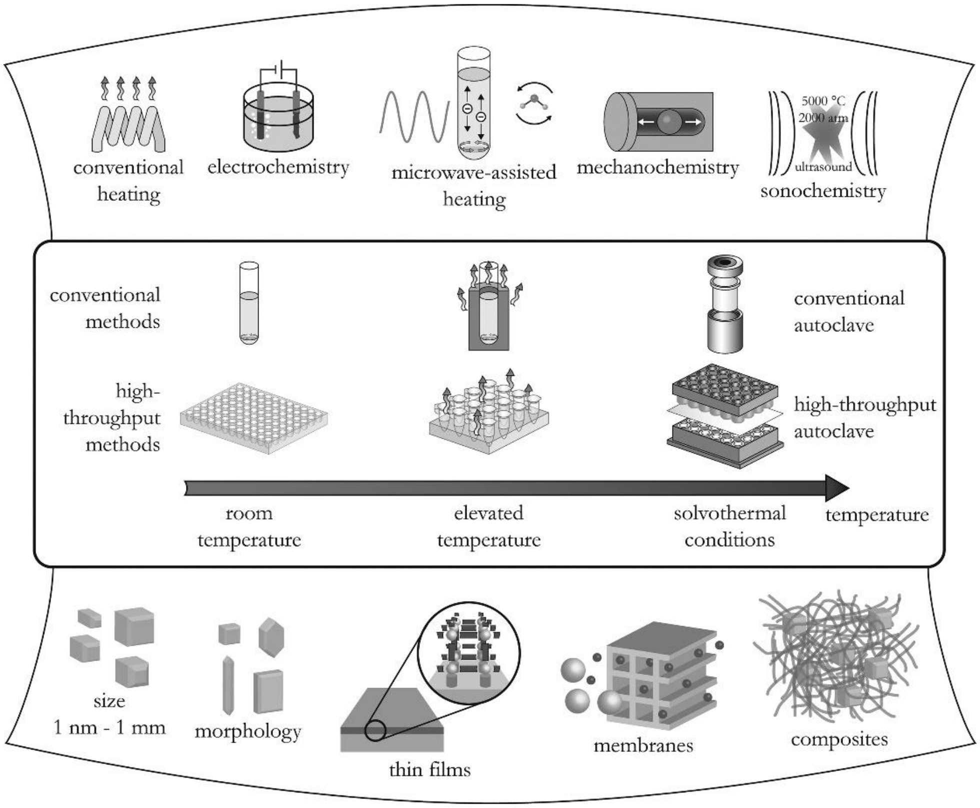

Figure 8. Overview of synthesis methods, various reaction temperatures and final reaction products in MOF synthesis. Reprinted from ref. 94, Copyright 2011, with the permission from American Chemical Society.

MOFs are very promising materials in a wide range of applications due to their diverse structure and composition, high porosity and tunable properties (Figure 9). One of the most pronounced application areas of MOF are gas storage and selective gas separation. Many MOFs showed already good performances for H_2[95], CH_4 storage[96], CO_2 capture[97] and gas separation[98]. Besides, MOFs are also potential candidates in applications such as drug delivery[99], sensing[100], electronics[101], optics[102] and water sorption for heat transformation[103]. Another pronounced and investigated area is catalysis[104]. In addition to the MOFs themselves, MOF composites and MOF derivatives can be also the catalyst for the desired reactions. Furthermore, MOFs can be used as support for the catalytically active species. In the literature, many examples of MOFs applied as catalysts in various catalytic reactions such as hydrogenation[105], photocatalysis[106], electrocatalysis[107]can be found. Furthermore, there is a growing interest to use MOFs as potential candidates for electrochemical energy storage and conversion.

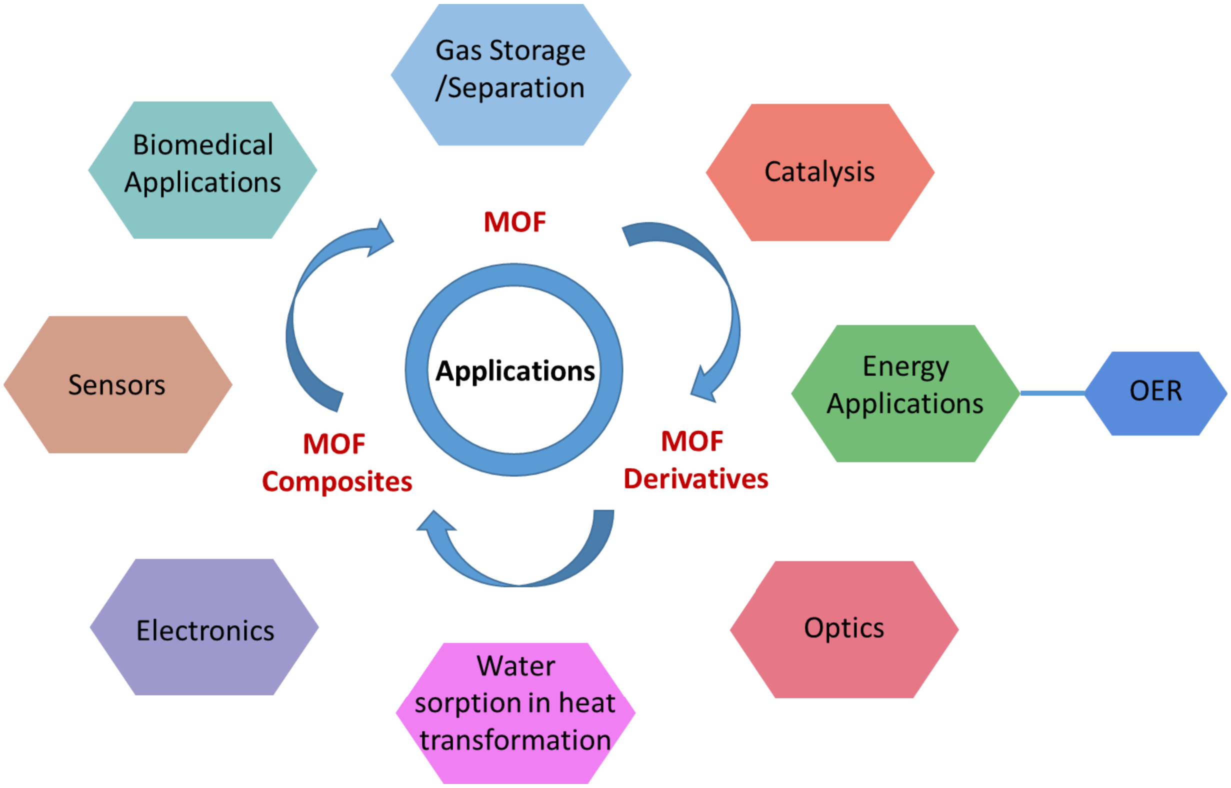

Figure 9. Application areas of MOFs, MOF composites and MOF derivatives.

Liao et al. showed the use of a pristine MOF for super capacitive charge storage which gave a high capacitance value up to 634 F g^{-1} [108]. Feng et al. demonstrated the performance of Fe_3O_4@MOF core-shell composites as anode materials in lithium-ion batteries. Fe_3O_4@MOF showed much higher discharge capacity than that of pure Fe_3O_4 [109]. Zhong et al. reported a MOF-CNT (CNT: carbon nanotube) composite for oxygen reduction reaction (ORR)[110]. Resulted catalyst showed the highest performance for ORR among the MOF composite electrocatalysts until that time and outperformed the state-of-the-art Pt/C electrocatalysts. Electrochemical oxygen evolution reaction (OER) is another widely studied research area for MOF based electrochemical catalysts. Tang et al. studied bimetallic pristine MOF (CoNi-UMOFNs) which exhibited very good performance for OER with a very low overpotential of 189 mV at 10 mA/cm^2 in an alkaline electrolyte[111]. It also showed an excellent long-term durability and a 99.3 % Faradaic efficiency. This outstanding electrocatalytic performance is mainly due to the abundant unsaturated metal active sites and the coupling effects between Co and Ni metals. MOFs can be decorated with active species to further enhance the electrocatalytic activity. One example was demonstrated by Wang et al. where α-MnO_2 nanoparticles were embedded into a MIL-101(Cr) matrix[112]. Resulting MOF composite material showed superior activity towards OER compared to the MIL-101(Cr) matrix and α-MnO_2 alone. In addition to synergistic effects between the MOF and α-MnO_2

nanoparticles, abundant micropores of MOF that covered the α-MnO_2 nanoparticles resulted in improved reactant accessibility to the catalytically active sites which together lead to improved OER performance. Although MOFs demonstrated good OER performance, the activity is negatively affected due to the poor conductive nature of many MOFs. The conductivity can be improved either by developing composites of MOFs together with conductive substrates such as graphene oxide[113], porous carbon[114], etc. or by the design and preparation of highly charge-conductive MOFs. A paddle-wheel-structured Cu-MOF and graphene oxide composite is synthesized and used as tri-functional catalyst[113]. This composite catalyst shows better OER activity than the Pt/C and corresponding pristine MOF. This high performance of the catalyst is attributed to the porous scaffold structure, larger bond polarity due to oxygen ligand in the graphene oxide and catalytically active copper which all together resulted in a facilitated charge and mass transfer and synergistic interactions. In another study, N-doped carbon is integrated with ZIF-67 (2-methylimidazole, Co^{2+}) and investigated for ORR and OER[114] (Figure 10). The hybrid showed a performance which is among the best reported bifunctional electrocatalysts that is related to the Co-N_4 in ZIF-67, electrochemical active surface area and strong interactions between ZIF-67 and N-doped carbon.

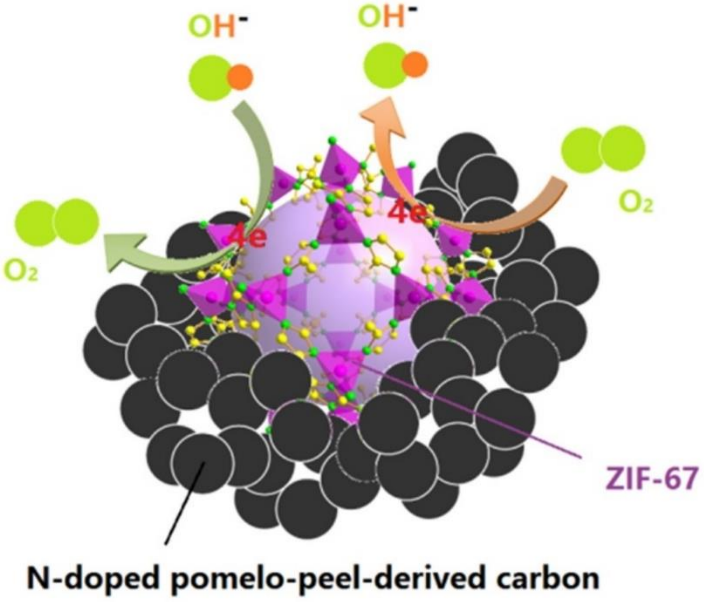

Figure 10. Illustration of a MOF carbon hybrid as bifunctional catalyst for OER and ORR. Reprinted from ref. 114, Copyright 2017, with the permission of Elsevier.

MOF derivatives are another strategy to fabricate electrocatalysts from MOFs. By using MOFs as sacrificial templates, various kinds of derivatives can be produced such as nanostructured carbon, metal oxides, metal composites, and other metal containing compounds[7,115]. A material containing

Co_3O_4 nanoparticles embedded in N-doped porous carbon was fabricated by two step thermal treatments of ZIF-67 in inert and air atmosphere[116]. The resulted porous carbon framework decorated with Co_3O_4 exhibited excellent OER catalytic activity comparable with that of commercial Ir/C catalyst. The combination of porous structure, highly conductive carbon networks, well dispersion of Co_3O_4 nanoparticles and synergistic effects between the Co_3O_4 and N-doped porous carbon were responsible for this outstanding performance.

2. Motivation

Global energy demand, depletion of fossil fuel resources and the environmental issues arising from their consumption drives researchers to develop sustainable energy sources. Solar energy, as being the most abundant energy source, has a great potential as clean energy source. One of the approaches to utilize solar energy is the conversion of solar energy into chemical energy such as through CO_2 reduction into hydrocarbons or H_2 production from water splitting.

Water splitting consist of two half reactions namely oxygen evolution reaction and hydrogen evolution reaction and it is an uphill reaction. Oxygen evolution reaction is the major bottleneck since it requires a four electron transfer and an oxygen-oxygen bond formation. Therefore, an efficient OER catalyst is the key for an efficient water splitting. Although precious metal oxides such as RuO_2 and IrO_2 are the most efficient electrocatalysts for OER, their scarcity and high cost hinders the large scale productivity. Consequently, development of efficient, stable, low cost and abundant OER catalysts are needed.

Porous materials such as CTFs and MOFs are potential candidates for OER catalysts. CTFs are nanoporous polymers based on triazine linkages and they have large surface areas, permanent porosity, high thermal and chemical stability. Additionally, the chemical structure and functionality of CTFs can be adjusted and heteroatoms or functional groups can be introduced into the framework. All these advantages make CTFs very attractive both as being direct catalyst or support for catalytically active species. On the other hand, MOFs are crystalline, porous hybrid materials constructed from inorganic secondary building units and organic linkers. The nearly unlimited chemical tunability together with high surface area and porosity of the MOFs paved the way for new OER catalysts. In addition to pristine MOF, MOF composites and MOF derivatives can be the OER electrocatalysts. Furthermore, MOFs can be also used as support for catalytically active species.

This thesis is concerned with the preparation, characterization and application of covalent-triazine framework and metal-organic framework based electrocatalysts for oxygen evolution reaction. Resulted materials will be intensively investigated by analytical methods including PXRD, N_2-physisorption, FT-IR, XPS, (HR-)TEM, SEM, STEM, EDX, AAS, TGA and elemental analysis.

In the first part of this thesis, the elecrocatalytic OER performance of CTF based materials are going to be investigated. Here, CTF-1 is going to be synthesized with different temperatures (400 °C and 600 °C) which would result in different properties for both materials. The materials are going to be characterized in detail and the differences will be pointed out. Different amount of nickel nanoparticles is going to be supported on these CTF-1s via microwave-assisted synthesis.

After detailed characterization of resulted materials, the OER and ORR performances are going to be investigated in alkaline conditions. The electrochemical performance results are going to be discussed and the possible reasons regarding the high performance are going to be explained. This is going to be the first study in the literature for investigation of a Ni/CTF catalyst for OER.

In the second part of the thesis, MOF based materials are going to be the focus for electrocatalytic OER. Since MOFs generally suffer from low electric conductivity which can hinder their catalytic performance, we aim to prepare a composite consisting MOF and electroconductive ketjenblack carbon. In this context, pure Ni(Fe)-MOF-74 and Ni(Fe)-MOF/KB are going to be prepared and characterized in detail. Additionally, for comparison the same synthesis procedure is going to be followed without the addition of linker, in other words without having a MOF structure. All differences of the materials are going to be pointed out with corresponding characterizations. The all prepared materials are going to be tested for electrochemical OER. The electrochemical results are going to be discussed in detail. With this study, we are aiming to show the first example of a MOF/KB composite as an efficient OER electrocatalyst in the literature.

3.Cumulative Part

The following chapters 3.1 and 3.2 contain the results of the dissertation which have been published/submitted in international journals. The publications are presented in chronological order, starting with the first publication as first author. Each publication contains a short introduction and summary of the work together with the assignments of tasks of the authors. Figures, tables and schemes do not follow the numbering of the main text, but the numbering of the publication itself. Each publication has its own reference list. Further unpublished work is illustrated in chapter 4.1-4.2.

3.1 Nickel nanoparticles supported on a covalent triazine framework as electrocatalyst for oxygen evolution reaction and oxygen reduction reactions

Secil Öztürk, Yu-Xuan Xiao, Dennis Dietrich, Beatriz Giesen, Juri Barthel, Jie Ying, Xiao-Yu Yang and Christoph Janiak

Beilstein J. Nanotechnol. **2020**, *11*, 770–781.

DOI: 10.3762/bjnano.11.62

Covalent triazine frameworks (CTFs) are a subclass of POPs which exhibit high surface area and porosity together with high thermal and chemical stability. The porosity and surface area of CTFs can be tuned by different synthesis temperature, time or the amount of $ZnCl_2$ in respect to aromatic nitrile monomer. All these properties make CTFs promising materials for the catalysis. Nevertheless, CTFs are marginally investigated for electrocatalysis especially for the electrochemical OER. In this work we synthesized CTF-1 with two different reaction temperatures (400°C and 600°C) resulting in different properties for each CTF. CTF synthesized at higher reaction temperature featured a higher BET surface area and total pore volume as expected. Since the nitrogen moieties within the CTFs can provide coordination anchors or stabilization of metal nanoparticles, we supported the nickel nanoparticles on synthesized CTFs via fast and efficient microwave synthesis. All synthesized materials were tested for electrochemical OER and ORR. The materials based on CTF-1-600 showed significantly higher OER activity than those based on CTF-1-400. Ni/CTF-1-600 showed a superior OER performance with 374 mV overpotential to reach 10 mA/cm^2 compared to commercial RuO_2 (403 mV) under same alkaline conditions and moderate performance for ORR (0.775 V half wave potential) compared to commercial Pt/C (0.890 V). The material also proved its superior stability via performed accelerated durability tests of 2000 cycles. The higher conductivity, surface area and the porosity of the CTF-1-600 is found to be related with the excellent electrochemical performance.

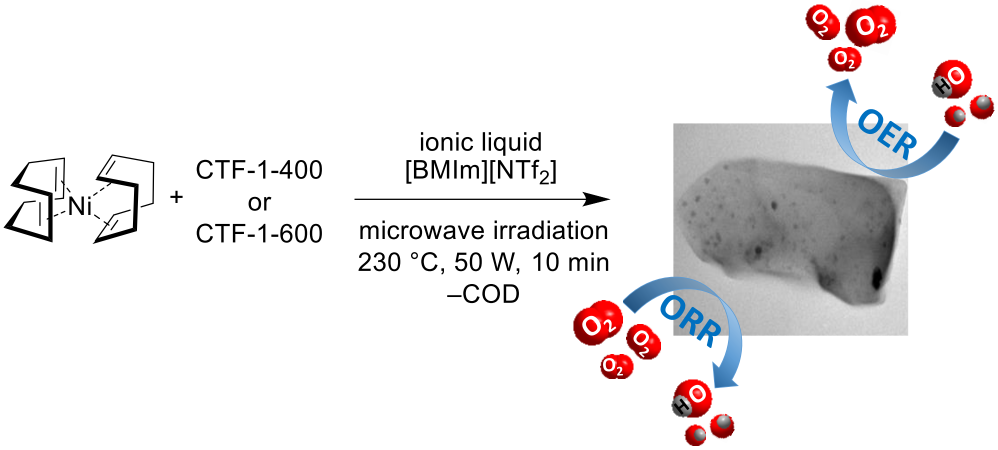

Author`s contribution to the publication:

- Comprehensive and independent literature research and planning of the research.
- Idea, concept, experimental work in the laboratory and characterization of the materials (except the work listed below).
- Drawing of all figures, graphs and tables (except the electrochemical data).
- Evaluation of all results and writing of the first draft of the manuscript.
- Editing of the manuscript regarding the reviewer`s comments.
- Electrochemical tests were performed and corresponding graphs were prepared by Mr. Yu-Xuan Xiao from the Wuhan University of Technology, China.
- TEM, STEM/EDX measurements were performed by Beatriz Giesen and Juri Barthel.
- SEM/EDX measurements were performed by Dennis Dietrich.
- Final coordination of the manuscript was done together with the comments from all co-authors.
- The manuscript draft and the revised manuscript was corrected and submitted to the international journal “Beilstein Journal of Nanotechnology” by Prof. Dr. Christoph Janiak.

BEILSTEIN JOURNAL OF NANOTECHNOLOGY

Nickel nanoparticles supported on a covalent triazine framework as electrocatalyst for oxygen evolution reaction and oxygen reduction reactions

Secil Öztürk[1], Yu-Xuan Xiao[2], Dennis Dietrich[1], Beatriz Giesen[1], Juri Barthel[3], Jie Ying[2], Xiao-Yu Yang[2] and Christoph Janiak*[1,§]

Full Research Paper

Open Access

Address:
[1]Institut für Anorganische Chemie und Strukturchemie, Heinrich-Heine-Universität Düsseldorf, 40204 Düsseldorf, Germany, [2]State Key Laboratory of Advanced Technology for Materials Synthesis and Processing and School of Materials Science and Engineering, Wuhan University of Technology, 430070 Wuhan, China and [3]Ernst Ruska-Centrum für Mikroskopie und Spektroskopie mit Elektronen, Forschungszentrum Jülich GmbH, 52425 Jülich, Germany

Email:
Christoph Janiak* - janiak@uni-duesseldorf.de

* Corresponding author
§ Fax: +49-211-81-12287; Tel: +49-211-81-12286

Keywords:
covalent triazine framework (CTF); electrocatalysis; nickel nanoparticles; oxygen evolution reaction; oxygen reduction reaction

Beilstein J. Nanotechnol. **2020,** *11,* 770–781.
doi:10.3762/bjnano.11.62

Received: 18 January 2020
Accepted: 20 April 2020
Published: 11 May 2020

Associate Editor: J. J. Schneider

Abstract

Covalent triazine frameworks (CTFs) are little investigated, albeit they are promising candidates for electrocatalysis, especially for the oxygen evolution reaction (OER). In this work, nickel nanoparticles (from $Ni(COD)_2$) were supported on CTF-1 materials, which were synthesized from 1,4-dicyanobenzene at 400 °C and 600 °C by the ionothermal method. CTF-1-600 and Ni/CTF-1-600 show high catalytic activity towards OER and a clear activity for the electrochemical oxygen reduction reaction (ORR). Ni/CTF-1-600 requires 374 mV overpotential in OER to reach 10 mA/cm^2, which outperforms the benchmark RuO_2 catalyst, which requires 403 mV under the same conditions. Ni/CTF-1-600 displays an OER catalytic activity comparable with many nickel-based electrocatalysts and is a potential candidate for OER. The same Ni/CTF-1-600 material shows a half-wave potential of 0.775 V for ORR, which is slightly lower than that of commercial Pt/C (0.890 V). Additionally, after accelerated durability tests of 2000 cycles, the material showed only a slight decrease in activity towards both OER and ORR, demonstrating its superior stability.

Introduction

A worldwide increasing energy demand combined with the depletion of fossil fuels and environmental issues requires the development of new sustainable clean energy sources [1]. In many renewable energy conversion and storage systems, the oxygen evolution reaction (OER) and the oxygen reduction reaction (ORR) are two crucial processes, which require improvements through the design of efficient catalysts. Both OER and ORR suffer from slow kinetics of the four-electron transfer process [2,3]. Thus, highly efficient electrocatalysts with enhanced performance need to be developed. Noble metals (Ir, Ru) and their oxides are the current commercial electrocatalysts for the OER, whereas Pt metal is the benchmark catalyst for the ORR [4,5]. Yet, all these catalysts have drawbacks such as scarcity and high cost, which are disadvantageous for their large-scale production and application. Consequently, researchers are working on discovering and developing catalysts for OER and ORR that are metal-free or based on non-noble metals, stable and earth-abundant [6-10].

Among the transition-metal-based OER and ORR catalysts, Ni-containing catalysts are promising candidates [7,11-13]. The performance of the nickel catalysts could be further enhanced via modifications, such as the usage of carbon supports including N-doped graphene [14], active carbon [15], graphene oxide [16,17], carbon nanotubes [12,18] and covalent triazine frameworks (CTFs) [19,20].

CTFs are nitrogen-containing aromatic polymer frameworks with triazine rings, which exhibit high surface area, porosity, and thermal and chemical stability [21,22]. CTFs are promising materials for applications such as catalysts or catalyst support [23-25] and for energy storage and conversion [26-28]. CTFs can be synthesized through different methods and under different reaction conditions, which enables the control over porosity and surface area [29-32]. The nitrogen moieties within the CTFs can provide coordination anchors or support for metal species [33,34]. They allow for the stabilization of metal nanoparticles and for a good dispersion of active species that are formed upon reduction of coordinated or impregnated metal precursors while minimizing their agglomeration and leaching [35]. In the literature we can find some studies that are focused on CTFs as catalysts for ORR. In the group of Prof. Fan, Co_3O_4/CTF1-700-1:1 has been studied as ORR catalyst and showed a half-wave potential of 0.84 V vs a reversible hydrogen electrode (RHE) [20]. Kamiya et. al. synthesized a Pt-atom-modified CTF hybridized with conductive carbon nanoparticles and used it as an ORR catalyst [36]. The same group also produced a Cu-modified CTF hybridized with carbon nanoparticles and it showed the highest reported value among Cu-based electrocatalysts with 810 mV onset potential vs RHE for the ORR at neutral pH value [37]. In contrast, up to now there are only few studies that investigated CTFs as OER catalysts or catalyst support and the activities were far lower than that of benchmark OER catalysts [38,39]. At present, there are no reports about nickel/CTF catalysts for electrochemical OER studies, to the best of our knowledge. Although various carbon materials or nitrogen-doped carbon materials have been utilized to support nickel as electrocatalyst for the OER, novel materials with high catalytic activity and strong durability still need to be investigated (Table S3, Supporting Information File 1). In our study, by using CTFs we have the advantages of abundant aromatic nitrogen atoms with lone electron pairs, which enable a coordination of nickel, a high chemical and thermal stability arising from the covalently bonded framework as well as high surface area and large pore volume, which allow for a facile molecular transport of reactants and products.

We report a route to Ni nanoparticles supported on CTF-1 in the ionic liquid (IL) [BMIm][NTf_2] using a microwave-assisted synthesis. The obtained material Ni/CTF-1 was investigated as a catalyst for electrochemical OER and ORR for the first time and showed a superior OER performance compared to commercial RuO_2 under alkaline conditions and moderate ORR performance compared with commercial Pt/C.

Results and Discussion

Synthesis and characterization of CTF

A number of studies have already shown that CTFs as catalyst support show a better catalytic performance than other carbon-based materials [40,41]. We synthesized CTF-1 according to the literature by the ionothermal method [32,42]. Since the synthesis parameters, such as reaction temperature, affect texture, porosity and nitrogen content of the framework, two different reaction temperatures (400 and 600 °C) have been used for the synthesis (Scheme S1, Supporting Information File 1).

As expected, both CTF-1-400 and CTF-1-600 (as-synthesized) showed limited long-range order according to powder X-ray diffraction (PXRD) measurements (Figure S1, Supporting Information File 1) [32,42]. Nitrogen sorption measurements for CTF-1-400 showed a type-I isotherm with 954 m^2/g Brunauer–Emmett–Teller (BET) surface area, whereas CTF-1-600 showed a mixture of type-I and type-IV isotherms (H2-type hysteresis) with a BET surface area of 1796 m^2/g (Figure S2, Supporting Information File 1). The total pore volume (at p/p_0 = 0.95) increased from 0.45 cm^3/g for CTF-1-400 to 1.06 cm^3/g for CTF-1-600 (see Table S2, Supporting Information File 1, for details). Elemental analyses, thermogravimetric analyses (TGA) and scanning electron microscopy (SEM) characterization data of the materials can be found in Table S1 and Figures S3–S5 in Supporting Information File 1.

Synthesis and characterization of Ni/CTF

For the synthesis of Ni nanoparticles (NPs) on the CTFs, the precursors bis(cycloocta-1,5-diene)nickel(0) (Ni(COD)$_2$) and CTF were suspended in [BMIm][NTf_2] by stirring under inert conditions for 12 h. The homogenized suspension was irradiated with microwaves and yielded Ni NPs immobilized on the

CTFs via the decomposition of the metal precursor in the IL (Scheme 1). The composites were designated Ni/CTF-1-400-X and Ni/CTF-1-600-X, where X represents the weight percentage of nickel in the composite material based on flame atomic absorption spectroscopy (AAS). Nickel loadings of 20 to 35 wt % on CTF-1 were obtained. The initial Ni/CTF mass ratios were 1:2 and 1:1. Thus, a large fraction of the nickel precursor was indeed deposited on the CTF. The starting mass ratio of 1:2 (or 33 wt % Ni) yielded 20–22 wt % Ni/CTF-1; the ratio of 1:1 (corresponding to 50 wt % Ni) gave 33–35 wt % Ni/CTF-1. This means that only a small part of the Ni NPs remains in the IL dispersion and supports the suggested role of nitrogen atoms in the CTFs as anchor points for the Ni NPs. The obtained nickel loadings on CTF-1 are similar to what has been reported for Ni nanoparticles encased in graphitic layers (25.2 wt %), Ni encapsulated within single-layer graphene (32.8 wt %), but higher than that of nickel nanoparticles encapsulated in N-doped carbon nanotubes (14.5 wt %), and much lower than those of with N-doped carbon shells coated face-centered cubic (fcc) or hexagonal closed packed (hcp) nickel (69 and 71 wt %, respectively, see Table S3, Supporting Information File 1).

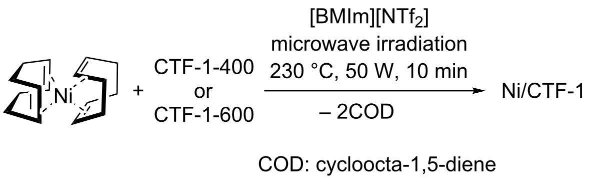

Scheme 1: Schematic representation of Ni/CTF-1 composite synthesis via microwave-assisted thermal decomposition of Ni(COD)$_2$ in the presence of CTF-1 and the ionic liquid [BMIm][NTf$_2$].

In the literature, there are various reports on Ni/carbon and Ni/N-doped carbon composites (Table S3, Supporting Information File 1). These composites are largely obtained by pyrolysis of Ni precursors or Ni-containing metal organic frameworks (MOF) with or without a nitrogen source [13,43,44]. An important step in these syntheses is high-temperature pyrolysis under inert atmosphere for a few hours. However, these methods often cannot control the nitrogen microstructure and composition. In contrast, Ni/CTF-1 is obtained in a fast and efficient microwave synthesis within 10 min from Ni(COD)$_2$ and the CTF substrate in an ionic liquid. The choice of the CTF substrate enables the control over nitrogen doping by selecting appropriate aromatic nitriles as monomers [32,37,40]. Also, it has been proven that the use of CTFs as support for nanoparticles can yield an advantage in terms of metal–support interactions compared to activated carbon [40].

In PXRD measurements, both cubic (fcc) and hexagonal (hcp) crystalline phases of nickel [45] were observed in all composites (Figure 1). When the nickel loading was low (20–22 wt %), the characteristic broad reflections for amorphous CTF could also be seen.

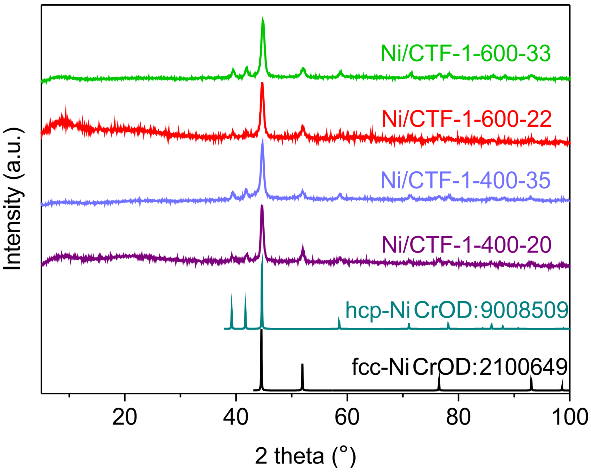

Figure 1: PXRD patterns of Ni/CTF-1 composite materials. The simulated diffractograms for hexagonal close-packed (hcp) and face-centered cubic (fcc) nickel are included, based on the crystallographic open database (CrOD) files.

Size and morphology of the synthesized Ni NPs on CTFs were characterized by transmission electron microscopy (TEM) and SEM. Figure 2 shows TEM images of Ni/CTF-1-600-22 recorded at different magnifications. Ni nanoparticles supported on CTF-1 can be observed. For images of the other Ni/CTF-1 composites see Figures S6–S8 and Figure S10, Supporting Information File 1. Figure 2c shows that nickel nanoparticles with an average diameter of 10 ± 2 nm are localized on the shard-like structures of CTF and appear to form aggregates with an average diameter of 72 ± 16 nm (see Figure S9, Supporting Information File 1 for size distributions). In high-resolution TEM images of the primary small Ni NPs (Figure 2d), interplanar spacings of the lattice fringes of 0.21 nm and 0.23 nm could be measured, which corresponds to the {111} lattice spacing of face-centered cubic (fcc) Ni and the {100} lattice spacing of hexagonal close-packed (hcp) Ni, respectively. These results are in good agreement with the PXRD data of Ni/CTF-1-600-22 shown in Figure 1, where both fcc and hcp Ni were observed.

The nickel loading on the CTF structures was further investigated by SEM-EDX elemental mapping (Figure 3), which also shows well-dispersed nickel nanoparticles on CTF. Given that nickel was detected by EDX on the whole surface of the CTF and not only on the agglomerate Ni NPs areas, further studies were performed using scanning transmission electron microsco-

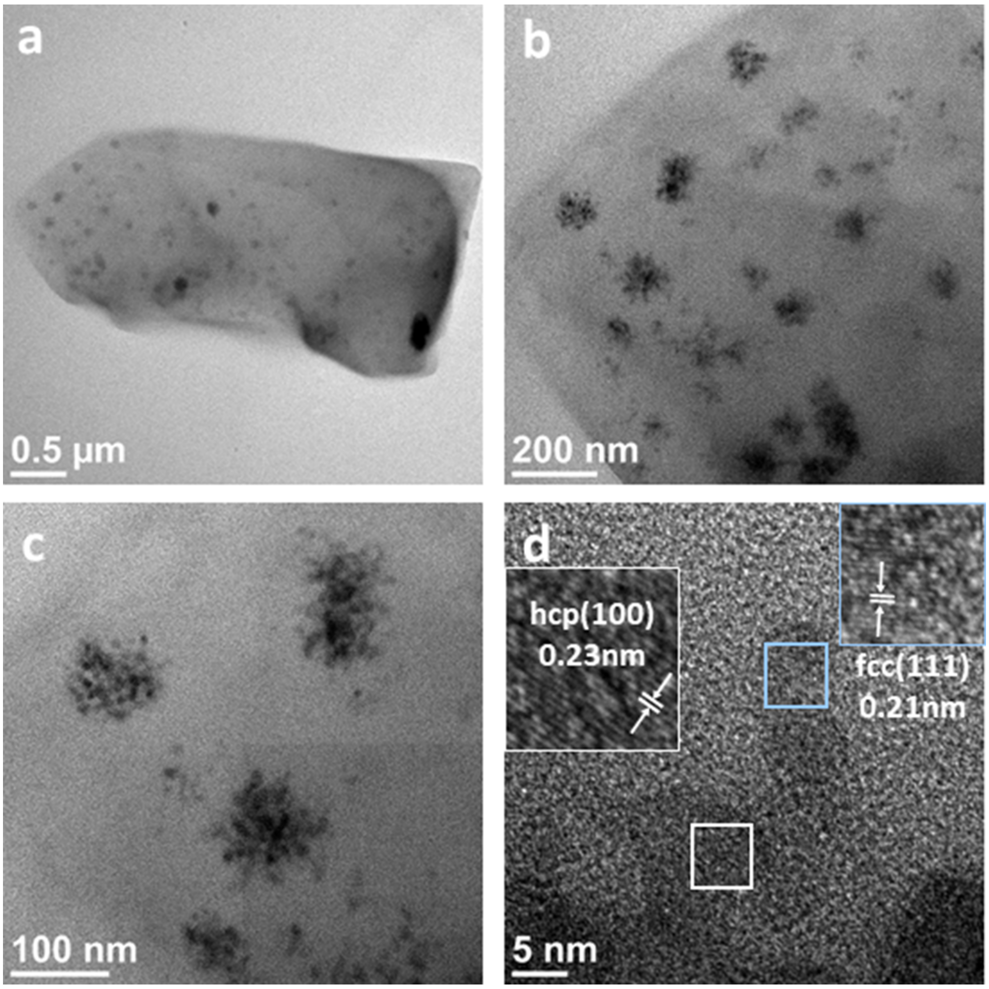

Figure 2: TEM images of Ni/CTF-1-600-22 showing (a) Ni nanoparticles supported on CTF, (b,c) the aggregation of the primary Ni nanoparticles and (d) the lattice planes of the Ni nanoparticles.

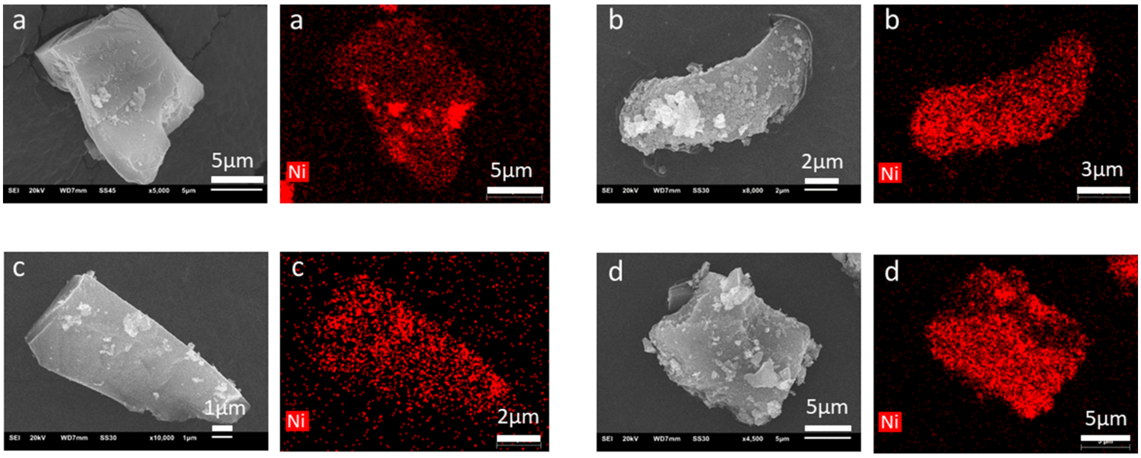

Figure 3: SEM images and EDX elemental mappings of Ni for (a) Ni/CTF-1-400-20, (b) Ni/CTF1-400-35, (c) Ni/CTF-1-600-22 and (d) Ni/CTF-1-600-33. Ni atoms are depicted in red.

py (STEM)-EDX elemental mapping. The element compositions of defined areas (orange square) showing both a single Ni particle and its CTF support in the background are displayed in Figure S11, Supporting Information File 1.

A possible reason why Ni NPs outside the NP agglomerates are not visible in the TEM images (Figure 2) can be either their small size or the fact that they lie between the CTF sheets (Figure S10c, Supporting Information File 1). Additional EDX studies (Figure S12, Supporting Information File 1) showed a higher content of Ni in the "brighter" agglomerates (point 1), as well as a lower but still measurable Ni count on the seemingly bare CTF shards (point 2). Thus, we conclude that nickel atoms are both found accumulated as larger NP agglomerates on the surface and as smaller nickel clusters. The smaller clusters can either reside on the surface or be included in the CTF framework. Furthermore, examination of the edges of the framework and of the nickel NPs revealed a partial oxidation. Figure S11d,f shows a correlation between Ni and O for the Ni/CTF-1-600-22 composite. This cannot be avoided, since the material was not handled under inert atmosphere (Figure S11 and Figure S13, Supporting Information File 1). The EDX point spectrum in Figure S12 for point 1 shows that the intensity of the Ni signal is stronger than the intensity of the O signal. An estimation of the atomic Ni/O ratio indicates that a significant amount of Ni at point 1 is not oxidized.

N_2 sorption isotherms were collected to obtain information about the porosity and the BET surface area of the materials. As shown in Figure 4, the BET surface area decreases as the nickel loading increases for each CTF-1-400 and CTF-1-600 support. Ni/CTF-1-400-20 exhibits a BET surface area of 486 m^2/g whereas Ni/CTF-1-400-35 shows a BET surface area of 300 m^2/g. For Ni/CTF-1-600-22 and Ni/CTF-1-600-33, the BET surface area is 816 m^2/g and 752 m^2/g, respectively. All CTFs with Ni show a lower BET surface area and pore volume than the corresponding pristine CTF materials, which can be attributed to the incorporation of nickel into the voids of CTF-1 (Table S2, Supporting Information File 1). Still, surface area and porosity of the Ni/CTF-1 composites are high, which are important features. It is accepted that conductivity plays a more important role, yet high surface area and porosity are known to enhance the exposure of active sites and to improve the ion and charge transfer through nanochannels together with the electron-conductive medium [46]. Here, the increase of conductivity and surface area from CTF-1-400 to CTF-1-600 go in the same direction and cannot be differentiated regarding their role in improving the activity of the CTF-1-600.

X-ray photoelectron spectroscopy (XPS) provides information about the chemical composition and chemical state of elements.

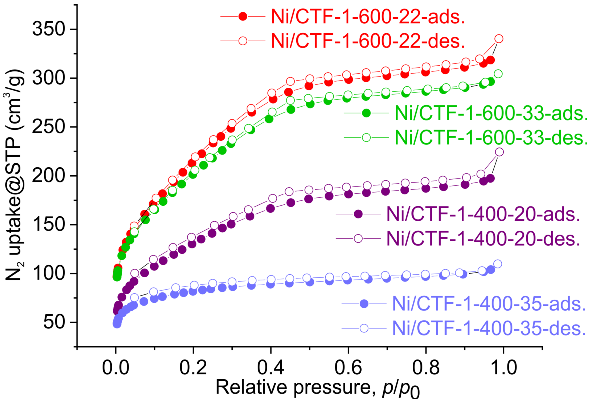

Figure 4: Nitrogen adsorption and desorption isotherms (at 77 K) of Ni/CTF-1 composites.

The Ni 2p and N 1s spectra of the materials are shown in Figure 5 and Figure S15–S18, Supporting Information File 1. The Ni 2p spectrum of Ni/CTF-1-600-22 consists of the main peak of Ni^0, of which only the more intense $2p_{3/2}$ peak at 852.7 eV is visible, because of the overall small amount of Ni^0. The Ni spectrum is dominated by the two main peaks of Ni^{2+} at 856.9 and 874.9 eV. The two peaks at 862.5 and 880.8 eV are satellite peaks of Ni^{2+}. Ni always shows strong satellites about 6 eV above the main electronic lines [47]. In composite materials, Ni^{2+} can arise from the combination of nickel coordinated with nitrogen and from the oxidation/hydroxylation of nickel (since the samples need to be briefly handled in air to be introduced into the XPS instrument).

Deconvolution of the N 1s XPS spectrum of Ni/CTF-1-600-22 reveals five peaks at about 398.5, 399.3, 400.6, 401.2 and 402.3 eV, which can be assigned pyridinic nitrogen, Ni-coordinated nitrogen, pyrrolic nitrogen, graphitic or quaternary nitrogen and oxidized nitrogen, respectively [26,48]. The formation of pyridinic N and graphitic or quaternary N have been demonstrated to improve the activity of N-modified carbon-based materials such as N-doped ordered porous carbon and N-doped carbon nanotubes [49,50]. According to our evaluation of the XPS data, 8 atom % N is involved in bonding to Ni for Ni/CTF-1-400-20, whereas 7 atom % N is involved in bonding to Ni for Ni/CTF-1-600-22.

Electrochemical catalysis

In order to investigate the activity of the synthesized materials in the OER, rotating disc electrode (RDE) experiments were conducted in 1 mol/L KOH solution in a three-electrode cell. Figure 6a shows the OER polarization curves of the catalysts measured with a sweep rate of 5 mV/s at room temperature. We note that there should be a nickel oxidation process visible before the onset of the OER. Yet, the oxidation process of Ni

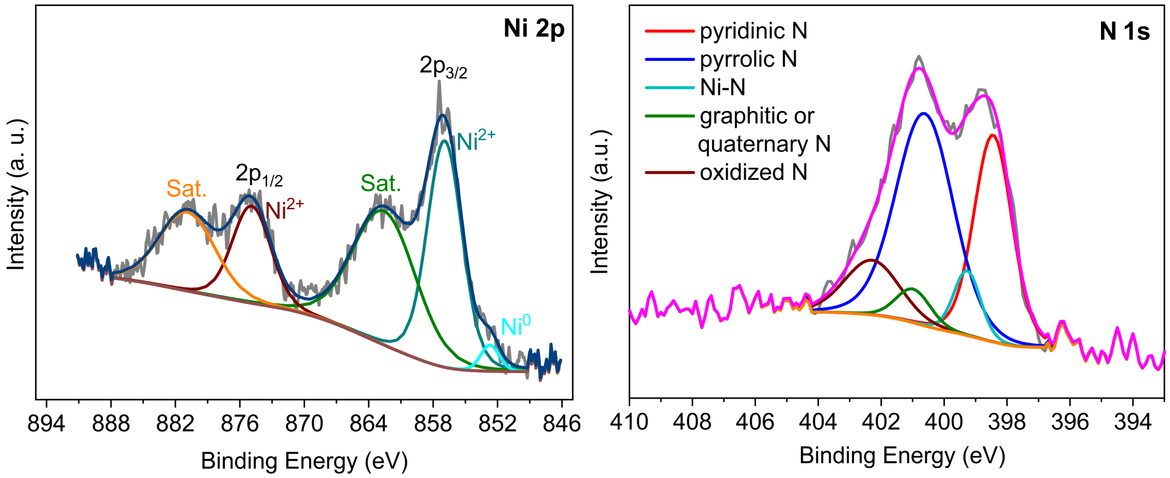

Figure 5: XPS measurements of Ni/CTF-1-600-22 with deconvoluted Ni 2p (left) (Sat. = satellite) and N 1s spectra (right).

for OER may be not evident [51,52]. Further, from XPS (Figure 5 and Supporting Information S15–S18, Supporting Information File 1) we can confirm the presence of Ni species on the surface of the composite materials but it is evident that nickel nanoparticles are already oxidized due to the handling of the sample in air.

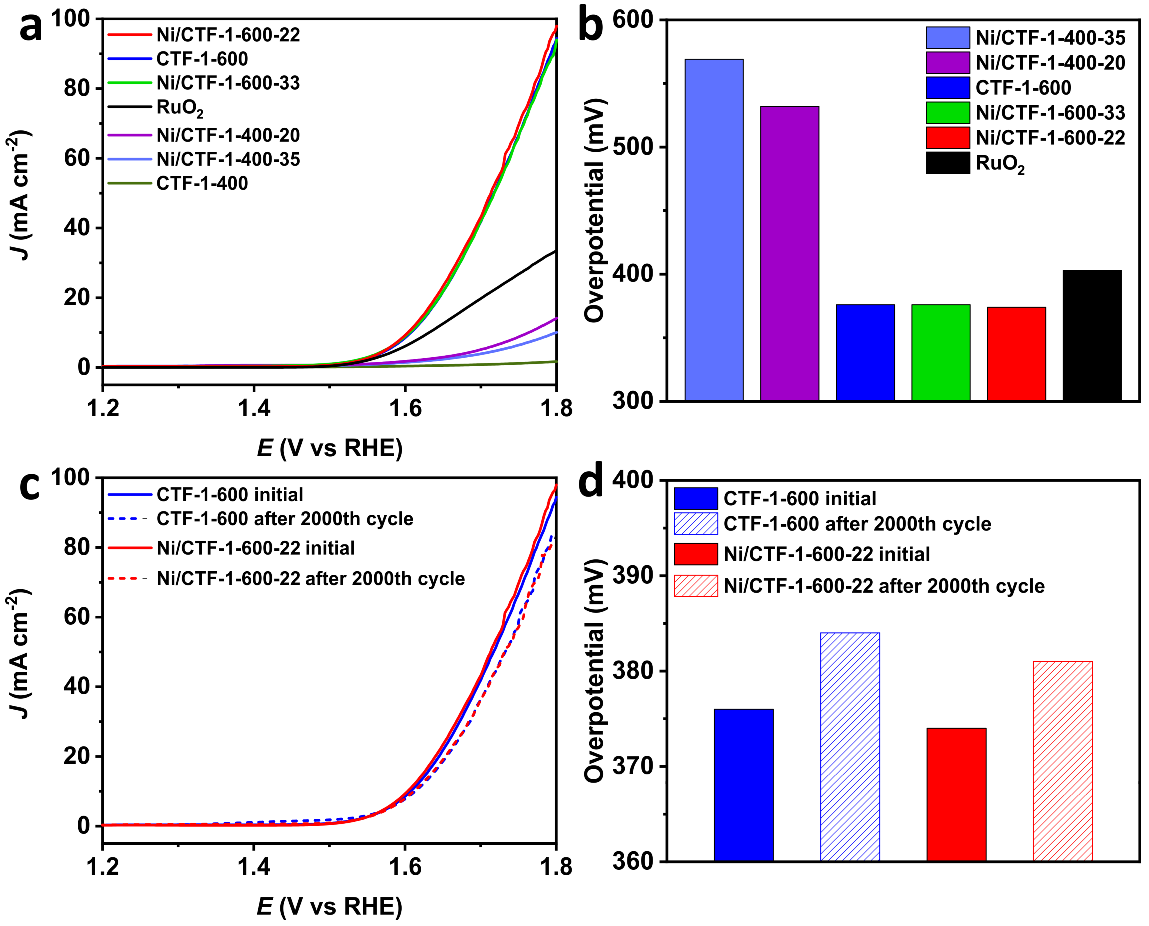

Figure 6: (a) OER polarization curves of various materials, (b) overpotential values calculated from (a); (c) OER polarization curves for CTF-1-600 and Ni/CTF-1-600-22 after 2000 cycles, (d) overpotential values calculated from (c).

The materials based on CTF-1-600 show a significantly higher OER activity than those based on CTF-1-400. Pristine CTF-1-400 showed almost no activity towards OER, whereas Ni/CTF-1-400-35 and Ni/CTF-1-400-20 showed higher activity with a required overpotential of 569 and 532 mV to reach 10 mA/cm^2, respectively. Nevertheless, all three samples showed much lower catalytic OER activity than the benchmark RuO_2 catalyst, which requires 403 mV under the same conditions. In contrast, pure CTF-1-600, Ni/CTF-1-600-33 and Ni/CTF-1-600-22 all show essentially identical OER activities with overpotentials of 376 mV for CTF-1-600, 374 mV for Ni/CTF-1-600-22 and 376 mV for Ni/CTF-1-600-33, which is better than the 403 mV for RuO_2 (Figure 6b). Moreover, the Tafel plots confirm the identical OER behavior of pure CTF-1-600, Ni/CTF-1-600-33 and Ni/CTF-1-600-22 (Figure S19, Supporting Information File 1). The very similar behavior among the CTF-1-600 series also suggests that the presence of Ni has no significant effect on CTF-1-600 for OER. Bare CTF-1-600 is found to be a good OER catalyst to begin with. At the same time, bare nickel was already shown not to be a good OER catalyst, having an overpotential of around 390 mV at 10 mA/cm^2 (vs RHE) or showing a current density of 0.25 mA/cm^2 at 1.70 V (vs RHE) [53,54]. The OER activity of Ni oxide and hydroxides in combination with carbon materials is ambiguous. NiO nanoparticles have an overpotential of 331 mV at 10 mA/cm^2 (vs RHE) [55], which increases to 422 mV at 10 mA/cm^2 (vs RHE) for a NiO nanoarray grown on carbon cloth [56]. Similarly, $Ni(OH)_2$ nanoparticles have an overpotential of only 299 mV to reach 10 mA/cm^2 (vs RHE) [55]. But this value increases to 462 mV for $Ni(OH)_2$ grown on carbon cloth [56]. Thus, the high electrocatalytic activity of the bare CTF-1-600 support is adversely affected by the admixture of Ni species with low activity in the composite materials. The better OER performance of CTF-1-600 over the CTF-1-400 materials is attributed to the better conductivity of the former (as given by the Nyquist plot in Figure 7) and its faster ion and charge transfer together with its higher porosity (Table S2, Supporting Information File 1). It is therefore understandable that the less conductive CTF-1-400 shows improved OER characteristics after the deposition of Ni.

Although Ni/CTF-1-600-22 is not the best catalyst compared to other carbon-supported nickel electrocatalysts (Table S3, Supporting Information File 1), its performance is better than many of these catalysts and its synthesis does not require special techniques or sophisticated equipment. The modifiable nitrogen functionalities enable stabilization and dispersion of metal sites throughout the support. The high chemical and thermal stability of the CTF support is another advantage, as this is often a problem of many other catalysts. CTF-1-600, as a metal-free electrocatalyst, showed better performance than N-doped carbon nanomaterials, which required an overpotential of 0.38 V vs RHE at 10 mA/cm^2 [57], better performance than N-doped carbon sheets requiring 0.41 V vs RHE [58] and better performance than nitrogen-doped graphene/carbon nanotube hybrids requiring an overpotential of 0.4 V vs RHE at 10 mA/cm^2 [59]. In comparison with the literature, CTF-1-600 and Ni/CTF-1-600-22 appear to be highly active OER electrocatalysts (cf. Table S3, Supporting Information File 1).

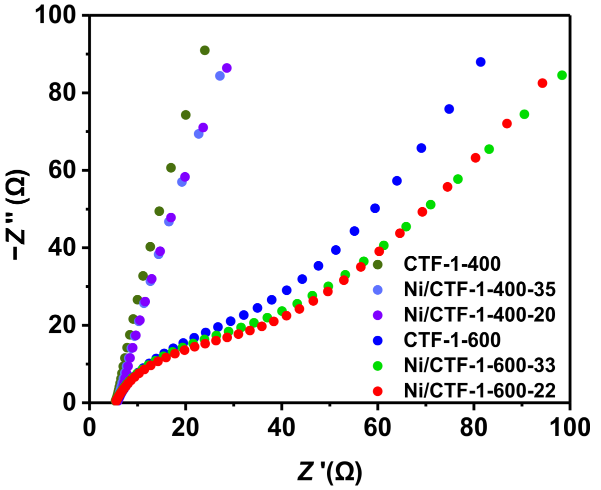

Figure 7: Nyquist plots recorded in 1 mol/L KOH solution.

Accelerated durability tests (ADTs) for cyclic potential sweeps were carried out for CTF-1-600 and Ni/CTF-1-600-22 in order to examine the durability of the catalysts. As shown in Figure 6c, the slope of CTF-1-600 and Ni/CTF-1-600-22 only shows a slight change after 2000 cycles. After 2000 cycles, the overpotential of CTF-1-600 changed from 376 to 384 mV, while the overpotential of Ni/CTF-1-600-22 changed from 374 to 381 mV (Figure 6d). The small change in the overpotential reveals the superior stability of these two materials.

To examine the electrocatalytic ORR activity of the materials, polarization curves were collected in O_2-saturated 1 mol/L KOH solution with a sweep rate of 10 mV/s at room temperature. The half-wave potentials are shown in Figure 8a. CTF-1-400, Ni/CTF-1-400-20 and Ni/CTF-1-400-35 show similar ORR polarization curves and their half-wave potentials of 0.573 V, 0.570 V and 0.576 V, respectively, are far smaller than those of the CTF-1-600 samples. The very similar potentials of the CTF-1-400 materials suggest that the presence of Ni has no significant effect on CTF-1-400 for ORR. The better ORR performance of CTF-1-600 over the CTF-1-400 materials is attributed to the better conductivity of the former (as obtained from the Nyquist plot in Figure 7).

The half-wave potential of Ni/CTF-1-600-22 (0.775 V) was larger than that of CTF-1-600 (0.724 V) and that of Ni/CTF-1-

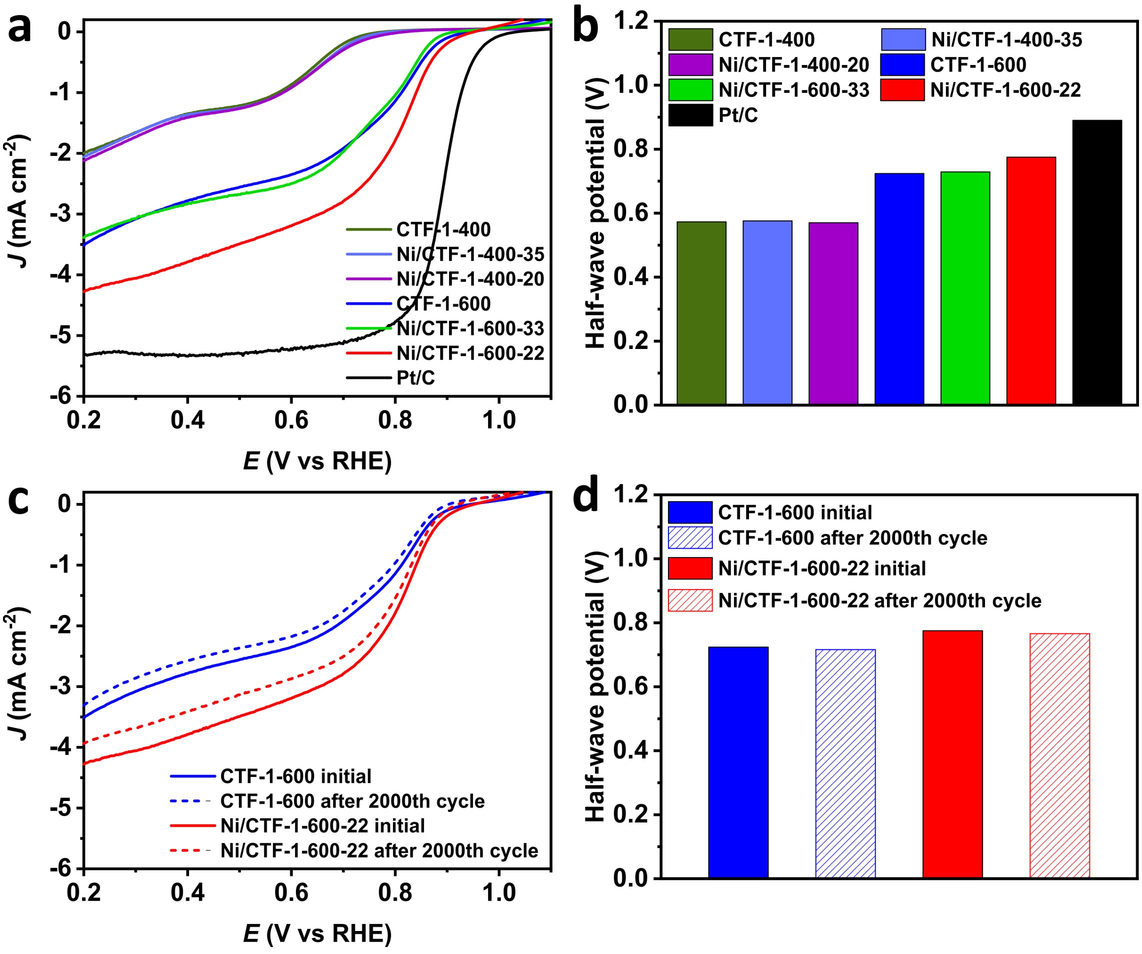

Figure 8: (a) ORR polarization curves of various materials, (b) half-wave potential values calculated from (a); (c) ORR polarization curves for CTF-1-600 and Ni/CTF-1-600-22 after 2000 cycles, (d) half-wave potential values calculated from (c).

600-33 (0.729 V), indicating a faster dynamic process regarding ORR activity for Ni/CTF-1-600-22. Compared to the half-wave potential of 0.890 V for commercial Pt/C, Ni/CTF-1-600-22 showed the best ORR performance among all tested Ni/CTF-1 and CTF-1 catalysts (Figure 8b). The Tafel plots also show that Ni/CTF-1-600-22 exhibits the best ORR activity and the performance (among Ni/CTF-1 materials) closest to commercial Pt/C (Figure S19, Supporting Information File 1). The half-wave potential of Ni/CTF-1-600-22 (0.775 V) is comparable to those given in the literature, such as nickel encapsulated in nitrogen-doped carbon nanotubes with a half-wave potential of 0.73 V (vs RHE) [60], nickel nanoparticles encased in graphitic layers with a half-wave potential of 0.78 V (vs RHE) [61] and nickel/nitrogen co-doped carbon nanocubes with a half-wave potential of 0.835 V (vs RHE) [62]. ADTs were performed to evaluate the stability of CTF-1-600 and Ni/CTF-1-600-22. The slope of both materials after 2000 cycles is shown in Figure 8c. The half-wave potential of CTF-1-600 dropped slightly from 0.724 V to 0.716 V, while the half-wave potential of Ni/CTF-1-600-22 dropped from 0.775 V to 0.766 V, indicating a good stability of both materials (Figure 8d).

The reason for the good electrochemical ORR performance of Ni/CTF-1-600-22 was investigated by electrochemical impedance spectroscopy (EIS). As shown in Figure 7, all CTF-1-600 materials exhibited a higher conductivity than CTF-1-400. This could be ascribed to the higher graphitization degree achieved through the higher synthesis temperature. Moreover, for the CTF-1-600 samples, the conductivity shows a trend of Ni/CTF-1-600-22 > Ni/CTF-1-600-33 > CTF-1-600, which is in accordance with the ORR results. In other words, the highest conductivity of Ni/CTF-1-600-22 coincided with the highest electrochemical ORR activity among all CTF species. ORR and OER are two reverse reaction sequences. In alkaline electrolyte, the mechanism of OER/ORR goes through the following elementary steps where S* is an active surface site or a surface-bound/adsorbed intermediate species, such as S–OH*, S–O* (in the literature often only * is used) [63]:

$$\begin{gathered}
\text{OER} \rightarrow \\
\text{OH}^- + \text{S*} \rightleftharpoons \text{S-OH*} + \text{e}^- \\
\text{S-OH*} + \text{OH}^- \rightleftharpoons \text{S-O*} + \text{H}_2\text{O} + \text{e}^- \\
\text{S-O*} + \text{OH}^- \rightleftharpoons \text{S-OOH*} + \text{e}^- \\
\text{S-OOH*} + \text{OH}^- \rightleftharpoons S* + \text{O}_2 + \text{H}_2\text{O} + \text{e}^- \\
\leftarrow \text{ORR}\,.
\end{gathered}$$

The OER proceeds through the formation of S-OH* and the ORR proceeds through the formation of S-OOH* in the reverse direction. Considering the mechanisms, the ORR and OER activity is limited by different rate-limiting steps for each reaction. The OER activity is limited by the S-O* and S-OOH* formation steps, whereas the ORR activity is limited by the S-OH* and O_2 reduction steps. In this regard, ORR and OER catalysts need to have different binding energies for intermediates for optimum activity. In addition to this, metal species undergo oxidation at the high positive potentials required for OER, which gives a positively charged more oxidized surface that is different than under reductive ORR conditions. Consequently, the best ORR catalyst may not simultaneously be the best OER catalyst [63].

For a Co_3O_4/CTF700-1:1 composite it has been founded that it exhibits improved ORR activity (half-wave potential of 0.84 V) compared to pure CTF700 and Co_3O_4 nanoparticles. The amount of Co_3O_4 in the composite material played an important role since it changed the activity of the composite but no activity trend related to the different used amounts was observed [20]. We observed a better activity of Ni/CTF-1-600-22, which means that a fraction of 22 wt % Ni is apparently more suitable than the 33 wt % in Ni/CTF-1-600-33.

In the literature, $Ni(OH)_2$/graphene oxide showed a significant enhancement of the ORR activity compared to unsupported $Ni(OH)_2$ and graphene oxide alone. The hybrid material $Ni(OH)_2$/graphene oxide has an onset potential of −0.17 V vs Ag/AgCl for ORR, which is 80 to 100 mV more positive than the corresponding onset potentials of unsupported $Ni(OH)_2$ (−0.25 V vs Ag/AgCl) and exfoliated graphite oxide sheets (−0.27 V vs Ag/AgCl) [64]. In another study, Ni-N/C (nickel nanoparticles/amino-N-doped carbon) exhibited an onset potential of 0.88 V vs RHE for the ORR [65] and showed a better activity than the pure amino-N-doped carbon with an onset potential of 0.82 V vs RHE [66]. Consequently, it is expected that nickel species improve the ORR activity of the catalysts.

Conclusion

We produced CTF-1-400 and CTF-1-600 (400 and 600 being the synthesis temperature in °C) to study them as direct electrocatalysts and as supports for nickel nanoparticles to give Ni/CTF-1 materials. The latter were also tested as electrocatalysts for OER and ORR. As a result of the different synthesis temperatures, different properties in CTF-1 were obtained. The CTF-1-600 material outperformed the less conductive CTF-1-400 material and the benchmark RuO_2 (403 mV) by reaching 10 mA/cm^2 with an overpotential of 374 mV. It also showed high stability. The CTF-based materials were also investigated for ORR and Ni/CTF-1-600-22 with 22 wt % Ni showed the best performance with a half-wave potential of 0.775 V, reaching the performance closest to the benchmark Pt/C catalyst, which shows a half-wave potential of 0.890 V under the same working conditions. The high electrochemical performance of Ni/CTF-1-600-22 can be traced to the best conductivity among all the CTF-based electrocatalysts as investigated by EIS tests. Consequently, we believe that CTFs are potential candidates for electrochemical OER and offer room for improvement. In the future, we anticipate that this study should inspire further investigations on CTF materials for electrocatalytic applications.

Experimental

Materials

Bis(cycloocta-1,5-diene)nickel(0) ($Ni(COD)_2$), 1,4 dicyanobenzene (98%) and 1-chlorobutane (>99%) were obtained from Sigma Aldrich, $ZnCl_2$ (>98%) from Alfa Aesar and bis(trifluoromethane)sulfonimide lithium salt (99%) from ABCR. All materials were used without further purification. 1-Methylimidazole (>99%) was obtained from Sigma Aldrich, purified via fractional distillation and dried over molecular sieves for several days. Water was purified using the Millipore® system. The ionic liquid (IL) 1-butyl-3-methylimidazolium bis(trifluoromethylsulfonyl)imide ([BMIm][NTf_2]) was synthesized in two steps following a literature procedure [67]. The anion purity of IL by ion chromatography was found to be above 99% and the water content of the IL by Karl-Fischer titration was less than 10 ppm.

Methods

Powder X-ray diffraction (PXRD) patterns were obtained at ambient temperature on a Bruker D2 Phaser powder diffractometer with a flat rotating silicon, low-background sample holder, at 30 kV, 10 mA for Cu Kα radiation (λ = 1.5418 Å). The diffractograms were analyzed with Match 3.11 software. All samples were measured between 5° and 100° 2θ with a scan speed of 2 s/step and 0.057° (2θ) step size. Nitrogen sorption measurements were performed with a Nova 4000e from Quantachrome at 77 K and evaluated with the NovaWin 11.03 software. The materials were first degassed under vacuum ($<10^{-2}$ mbar) at 120 °C overnight. The Brunauer–Emmett–Teller (BET) surface areas were calculated from five adsorption points in the range of p/p_0 = 0.02–0.1 for CTF-1-400 and Ni/CTF-1-400-20, of p/p_0 = 0.1–0.3 for Ni/CTF-1-400-35 and of p/p_0 = 0.1–0.2 for CTF-1-600 and its corresponding composites. The pore size distribution was derived by NLDFT calculations based on N_2 at 77 K on carbon with slit pores. Thermogravimetric analysis (TGA) was done with a Netzsch TG 209 F3 Tarsus device equipped with an Al crucible applying a heating rate of 10 K/min under inert atmosphere. Elemental analyses (CHN) were performed with a Perkin Elmer 2400 apparatus. Flame atomic absorption spectroscopy (AAS) for the determination of the metal content was conducted with a Vario 6 from Analytic Jena. For AAS the sample was treated with aqua regia. Ion chromatography (IC) measurements were performed with a Dionex ICS 1100 instrument with an IonPac AS 22column, combined with suppressed conductivity detection. Karl-Fischer titration (KFT) was carried out with an ECH/ANALYTIK JENA AQUA 40:00 Karl Fischer titrator. A Carbolite Gero tube furnace has been used for the CTF synthesis. Scanning electron microscopy (SEM) images were recorded with a Jeol JSM-65 10 LV QSEM advanced electron microscope with a LaB_6 cathode at 5–20 keV and a Bruker Xflash 410 silicon drift detector for energy-dispersive X-ray spectrometric (EDX) elemental composition analysis. M/CTF-IL suspension samples for transmission electron microscopy (TEM) were dripped on a carbon-coated copper grid and excess IL was washed off three times with acetonitrile and left to dry. Images were recorded on a FEI Tecnai G2 F20 electron microscope operated at 200 kV accelerating voltage equipped with a Gatan UltraScan 1000P detector [68]. Scanning transmission electron microscopy (STEM) images and EDX elemental mapping were conducted with the same instrument. High-resolution TEM images were recorded with an FEI Titan 80-300 transmission electron microscope [69] operated at 300 kV accelerating voltage. The microscope is equipped with an image CS corrector and a 2k × 2k GATAN UltraScan 1000 CCD. Nanoparticle size and size distribution were determined using the Digital Micrograph software from Gatan analyzing over 100 particles.

X-ray photoelectron spectroscopy (XPS) was performed using a ULVAC-PHI VersaProbe II microfocus X-ray photoelectron spectrometer. The spectra were recorded using a polychromatic Al Kα X-ray source (1486.8 eV). The C 1s orbital with a binding energy of 284.8 eV was taken as a reference for the evaluation of the spectra. CasaXPS, version 2.3.19PR1.0, copyright 1999-2018 Casa Software Ltd. program was used for the fit of the experimental XP spectra.

Synthesis of CTF-1

CTF-1-400 and CTF-1-600 were synthesized by ionothermal reaction at 400 and 600 °C, respectively, according to the literature [32,42]. For the synthesis of CTF-1-400, 1.28 g (10 mmol, 1 equiv) of dicyanobenzene (DCB) and 6.80 g (50 mmol, 5 equiv) anhydrous $ZnCl_2$ were mixed in a Duran glass ampoule under inert conditions. The ampoule was evacuated, flame-sealed and heated in a tube oven at 400 °C for 48 h. After the ampoule was cooled down to ambient temperature, it was opened and the black solid product was ground. The product was washed first with 200 mL Millipore water for 72 h. After isolation of the product by filtration, it was washed with 200 mL diluted hydrochloric acid (HCl) (2 mol/L) for 24 h. The washing process was further continued with millipore water (3 × 75 mL), tetrahydrofuran (THF) (3 × 75 mL) and acetone (3 × 75 mL). The resulted product was dried under high vacuum at 120 °C overnight. The same procedure has been followed for CTF-1-600 by first heating to 400 °C for 40 h and subsequently to 600 °C for 20 h.

Synthesis of Ni/CTF-1 in [BMIm][NTf_2]

$Ni(COD)_2$ (23.4 mg, 0.085 mmol or 46.8 mg, 0.17 mmol) and 10 mg of CTF-1-400 or CTF-1-600 were stirred in 1 g of IL in a microwave tube at room temperature and in a glovebox for 12 h. The mass of the nickel precursor was set to yield 0.5 or 1.0 wt % metal nanoparticles in IL, whereas 1.0 wt % CTF was used for all syntheses in IL dispersions. This dispersion was placed in a microwave (CEM Discover) and irradiated with a power of 50 W to 230 °C for 10 min. The volatiles from the Ni/CTF-1 product were removed under vacuum and then the product was handled in air, washed with acetonitrile (3 × 4 mL) centrifuged (6000 rpm), and then dried under vacuum. All reactions and the analysis of the products by PXRD have been repeated several times in order to confirm the reproducibility. The obtained materials were designated as Ni/CTF-1-400-X and Ni/CTF-1-600-X, where X represents the weight percentage of nickel in the composite materials according to AAS.

Electrochemical measurements

A three-electrode cell was used for the electrochemical measurements on a Autolab working station from Metrohm, Switzerland. Typically, a Ag/AgCl electrode (with saturated KCl solution) was used as a reference electrode, a carbon rod was used as a counter electrode, and a glassy-carbon rotating disk electrode (RDE, diameter: 5 mm, area: 0.196 cm^2) was used as the working electrode. The loading amount of all catalysts was 0.255 mg/cm^2. The OER measurements were carried out in 1 mol/L KOH using the glassy-carbon RDE at a rotation rate of 1600 rpm with a 5 mV/s sweep rate. The accelerated durability tests (ADTs) for OER were performed in 1 mol/L KOH solution with cyclic potential sweeps between 1.23 and 1.53 V vs reversible hydrogen electrode (RHE) at a 100 mV/s sweep rate for 2000 cycles. The ORR measurements were carried out in 1 mol/L O_2-saturated KOH solution under O_2

flow using the glassy-carbon RDE at a rotation rate of 1600 rpm with a 10 mV/s sweep rate. The ADTs for ORR were performed in 1 mol/L KOH solution under air with cyclic potential sweeps between 0.6 and 1.1 V versus RHE at a 50 mV/s sweep rate for 2000 cycles. The electrochemical impedance spectroscopy (EIS) measurements were performed in 1 mol/L KOH, in a frequency range of (0.1–1) × 10^5 Hz and a small sine-wave distortion (AC signal) of 10 mV amplitude. All potentials were converted to values with reference to RHE.

Supporting Information

Supporting Information File 1

Additional experimental data.
[https://www.beilstein-journals.org/bjnano/content/supplementary/2190-4286-11-62-S1.pdf]

Funding

We acknowledge a joint DFG-NSFC project to C.J. and X.-Y.Y. (DFG JA466/39-1, NSFC grant 51861135313).

ORCID® iDs

Secil Öztürk - https://orcid.org/0000-0001-6236-4385
Beatriz Giesen - https://orcid.org/0000-0002-3858-6460
Juri Barthel - https://orcid.org/0000-0003-3914-4346
Xiao-Yu Yang - https://orcid.org/0000-0003-3454-3604
Christoph Janiak - https://orcid.org/0000-0002-6288-9605

References

1. Lewis, N. S.; Nocera, D. G. *Proc. Natl. Acad. Sci. U. S. A.* **2006,** *103,* 15729–15735. doi:10.1073/pnas.0603395103
2. Cook, T. R.; Dogutan, D. K.; Reece, S. Y.; Surendranath, Y.; Teets, T. S.; Nocera, D. G. *Chem. Rev.* **2010,** *110,* 6474–6502. doi:10.1021/cr100246c
3. Xu, H.; Ci, S.; Ding, Y.; Wang, G.; Wen, Z. *J. Mater. Chem. A* **2019,** *7,* 8006–8029. doi:10.1039/c9ta00833k
4. Wang, Y.-J.; Zhao, N.; Fang, B.; Li, H.; Bi, X. T.; Wang, H. *Chem. Rev.* **2015,** *115,* 3433–3467. doi:10.1021/cr500519c
5. Lee, Y.; Suntivich, J.; May, K. J.; Perry, E. E.; Shao-Horn, Y. *J. Phys. Chem. Lett.* **2012,** *3,* 399–404. doi:10.1021/jz2016507
6. Deng, X.; Tüysüz, H. *ACS Catal.* **2014,** *4,* 3701–3714. doi:10.1021/cs500713d
7. Deng, X.; Öztürk, S.; Weidenthaler, C.; Tüysüz, H. *ACS Appl. Mater. Interfaces* **2017,** *9,* 21225–21233. doi:10.1021/acsami.7b02571
8. Song, F.; Hu, X. *J. Am. Chem. Soc.* **2014,** *136,* 16481–16484. doi:10.1021/ja5096733
9. Wu, G.; Zelenay, P. *Acc. Chem. Res.* **2013,** *46,* 1878–1889. doi:10.1021/ar400011z
10. Wu, G.; Santandreu, A.; Kellogg, W.; Gupta, S.; Ogoke, O.; Zhang, H.; Wang, H.-L.; Dai, L. *Nano Energy* **2016,** *29,* 83–110. doi:10.1016/j.nanoen.2015.12.032
11. Osgood, H.; Devaguptapu, S. V.; Xu, H.; Cho, J.; Wu, G. *Nano Today* **2016,** *11,* 601–625. doi:10.1016/j.nantod.2016.09.001
12. Zhong, G.; Li, S.; Xu, S.; Liao, W.; Fu, X.; Peng, F. *ACS Sustainable Chem. Eng.* **2018,** *6,* 15108–15118. doi:10.1021/acssuschemeng.8b03582
13. Wang, C.; Wang, Y.; Yang, H.; Zhang, Y.; Zhao, H.; Wang, Q. *Small* **2018,** *14,* 1802895. doi:10.1002/smll.201802895
14. Chen, S.; Duan, J.; Ran, J.; Jaroniec, M.; Qiao, S. Z. *Energy Environ. Sci.* **2013,** *6,* 3693–3699. doi:10.1039/c3ee42383b
15. Hoang, V. C.; Dinh, K. N.; Gomes, V. G. *Carbon* **2019,** *157,* 515–524. doi:10.1016/j.carbon.2019.09.080
16. Park, S.; Shao, Y.; Wan, H.; Rieke, P. C.; Viswanathan, V. V.; Towne, S. A.; Saraf, L. V.; Liu, J.; Lin, Y.; Wang, Y. *Electrochem. Commun.* **2011,** *13,* 258–261. doi:10.1016/j.elecom.2010.12.028
17. Liu, Q.; Jin, J.; Zhang, J. *ACS Appl. Mater. Interfaces* **2013,** *5,* 5002–5008. doi:10.1021/am4007897
18. Liang, Y.; Wang, H.; Diao, P.; Chang, W.; Hong, G.; Li, Y.; Gong, M.; Xie, L.; Zhou, J.; Wang, J.; Reiger, T. Z.; Wie, F.; Dai, H. *J. Am. Chem. Soc.* **2012,** *134,* 15849–15857. doi:10.1021/ja305623m
19. Chan-Thaw, C. E.; Villa, A.; Prati, L.; Thomas, A. *Chem. – Eur. J.* **2011,** *17,* 1052–1057. doi:10.1002/chem.201000675
20. Chen, S.; Zhu, Y.; Xu, D.; Peng, W.; Li, Y.; Zhang, G.; Zhang, F.; Fan, X. *ChemElectroChem* **2018,** *5,* 717–721. doi:10.1002/celc.201701085
21. Kuhn, P.; Antonietti, M.; Thomas, A. *Angew. Chem., Int. Ed.* **2008,** *47,* 3450–3453. doi:10.1002/anie.200705710
22. Kuhn, P.; Thomas, A.; Antonietti, M. *Macromolecules* **2009,** *42,* 319–326. doi:10.1021/ma802322j
23. Siebels, M.; Schlüsener, C.; Thomas, J.; Xiao, Y.-X.; Yang, X.-Y.; Janiak, C. *J. Mater. Chem. A* **2019,** *7,* 11934–11943. doi:10.1039/c8ta12353e
24. Katekomol, P.; Roeser, J.; Bojdys, M.; Weber, J.; Thomas, A. *Chem. Mater.* **2013,** *25,* 1542–1548. doi:10.1021/cm303751n
25. Wang, Z.; Liu, C.; Huang, Y.; Hu, Y.; Zhang, B. *Chem. Commun.* **2016,** *52,* 2960–2963. doi:10.1039/c5cc10389d
26. Lu, C.; Yang, J.; Wei, S.; Bi, S.; Xia, Y.; Chen, M.; Hou, Y.; Qiu, M.; Yuan, C.; Su, Y.; Zhang, F.; Liang, H.; Zhuang, X. *Adv. Funct. Mater.* **2019,** *29,* 1806884. doi:10.1002/adfm.201806884
27. Zhang, Y.; Jin, S. *Polymers (Basel, Switz.)* **2018,** *11,* 31. doi:10.3390/polym11010031
28. Lan, X.; Du, C.; Cao, L.; She, T.; Li, Y.; Bai, G. *ACS Appl. Mater. Interfaces* **2018,** *10,* 38953–38962. doi:10.1021/acsami.8b14743
29. Bhunia, A.; Boldog, I.; Möller, A.; Janiak, C. *J. Mater. Chem. A* **2013,** *1,* 14990–14999. doi:10.1039/c3ta13407e
30. Wang, K.; Yang, L.-M.; Wang, X.; Guo, L.; Cheng, G.; Zhang, C.; Jin, S.; Tan, B.; Cooper, A. *Angew. Chem., Int. Ed.* **2017,** *56,* 14149–14153. doi:10.1002/anie.201708548
31. Ren, S.; Bojdys, M. J.; Dawson, R.; Laybourn, A.; Khimyak, Y. Z.; Adams, D. J.; Cooper, A. I. *Adv. Mater. (Weinheim, Ger.)* **2012,** *24,* 2357–2361. doi:10.1002/adma.201200751
32. Kuhn, P.; Forget, A.; Su, D.; Thomas, A.; Antonietti, M. *J. Am. Chem. Soc.* **2008,** *130,* 13333–13337. doi:10.1021/ja803708s
33. Li, J.; Zhang, L.; Liu, X.; Shang, N.; Gao, S.; Feng, C.; Wang, C.; Wang, Z. *New J. Chem.* **2018,** *42,* 9684–9689. doi:10.1039/c8nj01404c
34. Su, P.; Iwase, K.; Harada, T.; Kamiya, K.; Nakanishi, S. *Chem. Sci.* **2018,** *9,* 3941–3947. doi:10.1039/c8sc00604k
35. Artz, J. *ChemCatChem* **2018,** *10,* 1753–1771. doi:10.1002/cctc.201701820

36. Kamiya, K.; Kamai, R.; Hahimoto, K.; Nakanishi, S. *Nat. Commun.* **2014,** *5,* 5040. doi:10.1038/ncomms6040
37. Iwase, K.; Yoshioka, T.; Nakanishi, S.; Hashimoto, K.; Kamiya, K. *Angew. Chem., Int. Ed.* **2015,** *54,* 11068–11072. doi:10.1002/anie.201503637
38. Gopi, S.; Kathiresan, M. *Polymer* **2017,** *109,* 315–320. doi:10.1016/j.polymer.2016.12.052
39. Yamaguchi, S.; Kamiya, K.; Hashimoto, K.; Nakanishi, S. *Chem. Commun.* **2017,** *53,* 10437–10440. doi:10.1039/c7cc05841a
40. Chan-Thaw, C. E.; Villa, A.; Katekomol, P.; Su, D.; Thomas, A.; Prati, L. *Nano Lett.* **2010,** *10,* 537–541. doi:10.1021/nl904082k
41. Li, Z.; He, T.; Liu, L.; Chen, W.; Zhang, M.; Wu, G.; Chen, P. *Chem. Sci.* **2017,** *8,* 781–788. doi:10.1039/c6sc02456d
42. Bhunia, A.; Dey, S.; Bous, M.; Zhang, C.; von Rybinski, W.; Janiak, C. *Chem. Commun.* **2015,** *51,* 484–486. doi:10.1039/c4cc06393g
43. Han, H.; Chao, S.; Yang, X.; Wang, X.; Wang, K.; Bai, Z.; Yang, L. *Int. J. Hydrogen Energy* **2017,** *42,* 16149–16156. doi:10.1016/j.ijhydene.2017.05.043
44. Zhang, X.; Xu, H.; Li, X.; Li, Y.; Yang, T.; Liang, Y. *ACS Catal.* **2016,** *6,* 580–588. doi:10.1021/acscatal.5b02291
45. Wegner, S.; Rutz, C.; Schütte, K.; Barthel, J.; Bushmelev, A.; Schmidt, A.; Dilchert, K.; Fischer, R. A.; Janiak, C. *Chem. – Eur. J.* **2017,** *23,* 6330–6340. doi:10.1002/chem.201605251
46. Hao, L.; Zhang, S.; Liu, R.; Ning, J.; Zhang, G.; Zhi, L. *Adv. Mater. (Weinheim, Ger.)* **2015,** *27,* 3190–3195. doi:10.1002/adma.201500863
47. Nassr, A. B. A. A.; Sinev, I.; Pohl, M.-M.; Grünert, W.; Bron, M. *ACS Catal.* **2014,** *4,* 2449–2462. doi:10.1021/cs401140g
48. Kundu, S.; Nagaiah, T. C.; Xia, W.; Wang, Y.; Van Dommele, S.; Bitter, J. H.; Santa, M.; Grundmeier, G.; Bron, M.; Schuhmann, W.; Muhler, M. *J. Phys. Chem. C* **2009,** *113,* 14302–14310. doi:10.1021/jp811320d
49. Liu, G.; Li, X.; Ganesan, P.; Popov, B. N. *Appl. Catal., B* **2009,** *93,* 156–165. doi:10.1016/j.apcatb.2009.09.025
50. Sun, J.; Wang, S.; Wang, Y.; Li, H.; Zhou, H.; Chen, B.; Zhang, X.; Chen, H.; Qu, K.; Zhao, J. *Catalysts* **2019,** *9,* 159. doi:10.3390/catal9020159
51. Gong, M.; Dai, H. *Nano Res.* **2015,** *8,* 23–39. doi:10.1007/s12274-014-0591-z
52. Zhu, K.; Wu, T.; Li, M.; Lu, R.; Zhu, X.; Yang, W. *J. Mater. Chem. A* **2017,** *5,* 19836–19845. doi:10.1039/c7ta05404a
53. Dong, C.; Liu, X.; Wang, X.; Yuan, X.; Xu, Z.; Dong, W.; Riaz, M. S.; Li, G.; Huang, F. *J. Mater. Chem. A* **2017,** *5,* 24767–24774. doi:10.1039/c7ta08440d
54. Xu, K.; Ding, H.; Lv, H.; Tao, S.; Chen, P.; Wu, X.; Chu, W.; Wu, C.; Xie, Y. *ACS Catal.* **2017,** *7,* 310–315. doi:10.1021/acscatal.6b02884
55. Cheng, N.; Liu, Q.; Tian, J.; Sun, X.; He, Y.; Zhai, S.; Asiri, A. M. *Int. J. Hydrogen Energy* **2015,** *40,* 9866–9871. doi:10.1016/j.ijhydene.2015.06.105
56. Stern, L.-A.; Hu, X. *Faraday Discuss.* **2014,** *176,* 363–379. doi:10.1039/c4fd00120f
57. Zhao, Y.; Nakamura, R.; Kamiya, K.; Nakanishi, S.; Hashimoto, K. *Nat. Commun.* **2013,** *4,* 2390. doi:10.1038/ncomms3390
58. Yuan, H.; Deng, L.; Cai, X.; Zhou, S.; Chen, Y.; Yuan, Y. *RSC Adv.* **2015,** *5,* 56121–56129. doi:10.1039/c5ra05461c
59. Tian, G.-L.; Zhao, M.-Q.; Yu, D.; Kong, X.-Y.; Huang, J.-Q.; Zhang, Q.; Wei, F. *Small* **2014,** *10,* 2251–2259. doi:10.1002/smll.201303715
60. Liu, Y.; Jiang, H.; Zhu, Y.; Yang, X.; Li, C. *J. Mater. Chem. A* **2016,** *4,* 1694–1701. doi:10.1039/c5ta10551j
61. Zhu, J.; Xiao, M.; Zhang, Y.; Jin, Z.; Peng, Z.; Liu, C.; Chen, S.; Ge, J.; Xing, W. *ACS Catal.* **2016,** *6,* 6335–6342. doi:10.1021/acscatal.6b01503
62. Mao, J.; Liu, P.; Li, J.; Liang, D.; Yan, J.; Song, W. *Adv. Mater. Interfaces* **2019,** *6,* 1901186. doi:10.1002/admi.201901186
63. Huang, Z.-F.; Wang, J.; Peng, Y.; Jung, C.-Y.; Fisher, A.; Wang, X. *Adv. Energy Mater.* **2017,** *7,* 1700544. doi:10.1002/aenm.201700544
64. Farjami, E.; Rottmayer, M. A.; Jay Deiner, L. *J. Mater. Chem. A* **2013,** *1,* 15501–15508. doi:10.1039/c3ta13351f
65. Kim, S.; Kato, S.; Ishizaki, T.; Li, O. L.; Kang, J. *Nanomaterials* **2019,** *9,* 742–753. doi:10.3390/nano9050742
66. Kim, D.-w.; Li, O. L.; Pootawang, P.; Saito, N. *RSC Adv.* **2014,** *4,* 16813–16819. doi:10.1039/c4ra02380c
67. Wasserscheid, P.; Welton, T. *Ionic Liquids in Synthesis,* 1st ed.; Wiley-VCH: Weinheim, Germany, 2002. doi:10.1002/3527600701
68. Ernst Ruska-Centre for Microscopy and Spectroscopy with Electrons. *J. Large-Scale Res. Facil.* **2016,** *2,* A77. doi:10.17815/jlsrf-2-138
69. Ernst Ruska-Centre for Microscopy and Spectroscopy with Electrons. *J. Large-Scale Res. Facil.* **2016,** *2,* A41. doi:10.17815/jlsrf-2-66

License and Terms

The definitive version of this article is the electronic one which can be found at:
doi:10.3762/bjnano.11.62

BEILSTEIN JOURNAL OF NANOTECHNOLOGY

Supporting Information

for

Nickel nanoparticles supported on a covalent triazine framework as electrocatalyst for oxygen evolution reaction and oxygen reduction reactions

Secil Öztürk, Yu-Xuan Xiao, Dennis Dietrich, Beatriz Giesen, Juri Barthel, Jie Ying, Xiao-Yu Yang and Christoph Janiak

Beilstein J. Nanotechnol. **2020,** *11,* 770–781. doi:10.3762/bjnano.11.62

Additional experimental data

Synthesis and characterization of CTFs

CTF-1-400 was synthesized mixing 1,4-dicyanobenzene (DCB) and zinc chloride ($ZnCl_2$) with a 1:5 monomer-to-salt ratio in a sealed glass ampoule at 400 °C for 48 h. CTF-1-600 was synthesized by the same route as CTF-1-400 except that the temperature was first held at 400 °C for 40 h and then at 600 °C for 20 h.

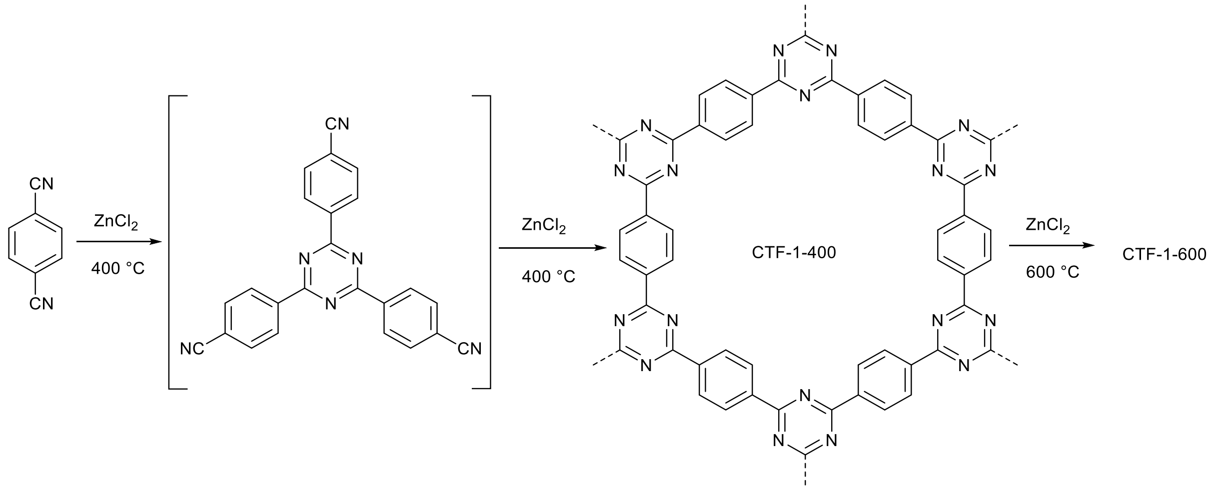

Scheme S1: Idealized schematic formation of CTF-1-400/600 starting from 1,4-dicyanobenzene via ionothermal method.

CTFs are only called and accepted as such if the temperature does not exceed 400 °C during the ionothermal synthesis. Even up to 400 °C the loss of nitrogen and the subsequent nitrogen deficit is quite high compared to the ideal structure. Above 400 °C nitrogen loss and deficit increase drastically such that the materials become essentially nitrogen-doped carbon materials. These materials must be compared to active carbon and no longer to CTFs that were prepared at 400 °C. Generally, at 600 °C higher surface areas and total pore volumes for the resulting “CTF” products are found than after comparable syntheses at 400 °C [1-3].

In PXRD, only two broad diffraction reflexes at around 8° and 22° 2θ, corresponding to the (100) and (001) planes, can be observed (Figure S1). Kuhn et. al. showed, that the broad reflex at 26.1° 2θ corresponds to the (001) interlayer distance of 3.4 Å of the aromatic sheets [4]. In our case, the maximum of this broad reflex is shifted towards 2θ = 21.9°, which was explained by Bhunia et. al [5] as an increase of the layer distance between the triazine sheets to 4.1 Å.

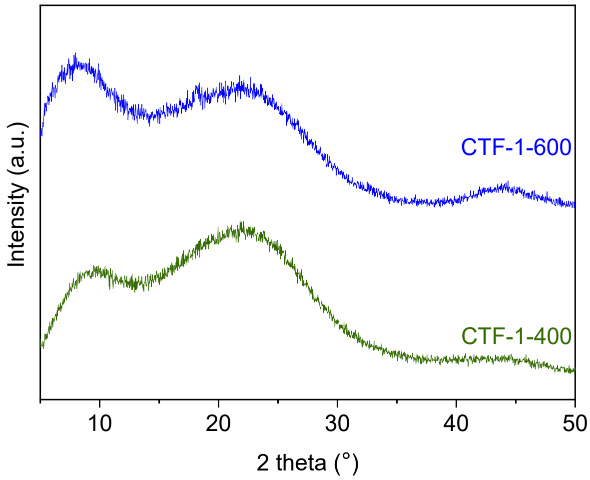

Figure S1: PXRD patterns of CTF-1-400 and CTF-1-600.

As a result of increased synthesis temperature, higher porosity and enhanced surface area have been observed for CTF-1-600 (Figure S2) as expected from earlier studies, where a surface area of 920 and 1750 or 2660 m^2/g (depending on the reaction time) was reported for CTF-1-400 and CTF-1-600, respectively [2]. The surface area for CTFs does not only vary with temperature but also with reaction time. The increase in surface area with temperature is a result of nitrogen loss and occurring defects due to the high temperature. This results in a higher pore volume and the formation of mesopores in the material [2].

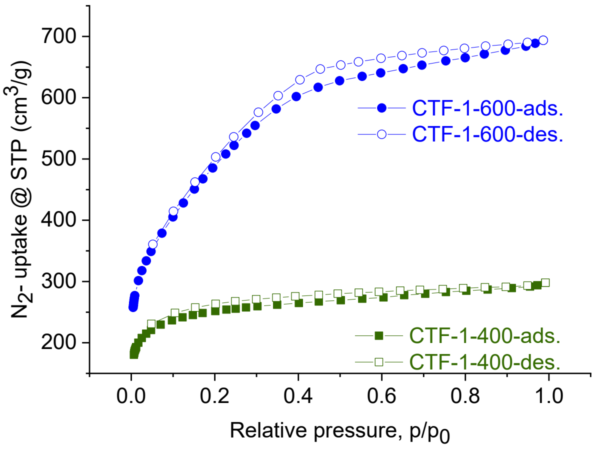

Figure S2: Nitrogen adsorption and desorption isotherms (at 77 K) of CTF-1-400 and CTF-1-600. See Table S2 and Figure S14 for the pore volumes and pore size distribution, respectively.

Elemental analyses yielded the expected C, H and N content (Table S1), in agreement with previous literature sources [2,5]. Increasing the synthesis temperature to 600 °C resulted in an increased C content and decreased N and H contents, which is explained by further linkage of the aromatic building blocks at higher temperatures, which occurs via [CN] and H_2 elimination [2].

Table S1: Elemental analysis of CTF-1-400 and CTF-1-600.[a]

	C [wt. %]	N [wt. %]	H [wt. %]	Rest [wt. %]	atom C/N
CTF-1 calculated*	74.99	21.86	3.15	—	4
CTF-1-400	75.92	14.54	2.75	6.79	6.1
CTF-1-600	79.27	9.43	1.09	10.21	9.8

[a] Calculation based on the idealized structure of CTF-1.

Thermogravimetric analyses under nitrogen atmosphere revealed the decomposition of the materials above 400 °C and 600 °C for CTF-1-400 and CTF-1-600, respectively. (Figure S3).

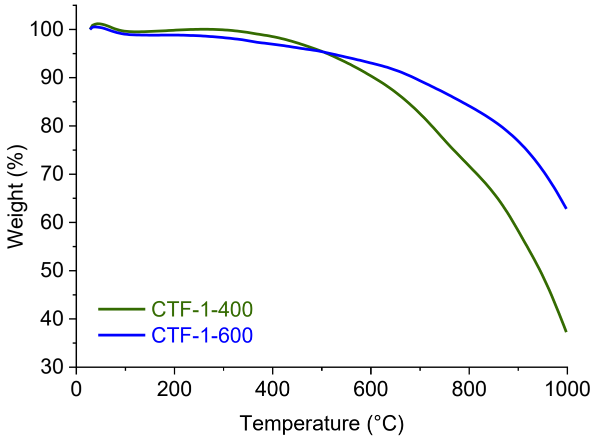

Figure S3: Thermogravimetric analysis (TGA) of CTF-1-400 and CTF-1-600 in the temperature range of 25–1000 °C under N_2 atmosphere with a heating rate of 10 K/min.

Scanning electron microscopy (SEM) showed a shard morphology with a wide particle size distribution for both CTFs (Figure S4) and slight impurities of chlorine and zinc have been found by energy dispersive X-ray spectrometry (EDX), which can be seen in Figure S5.

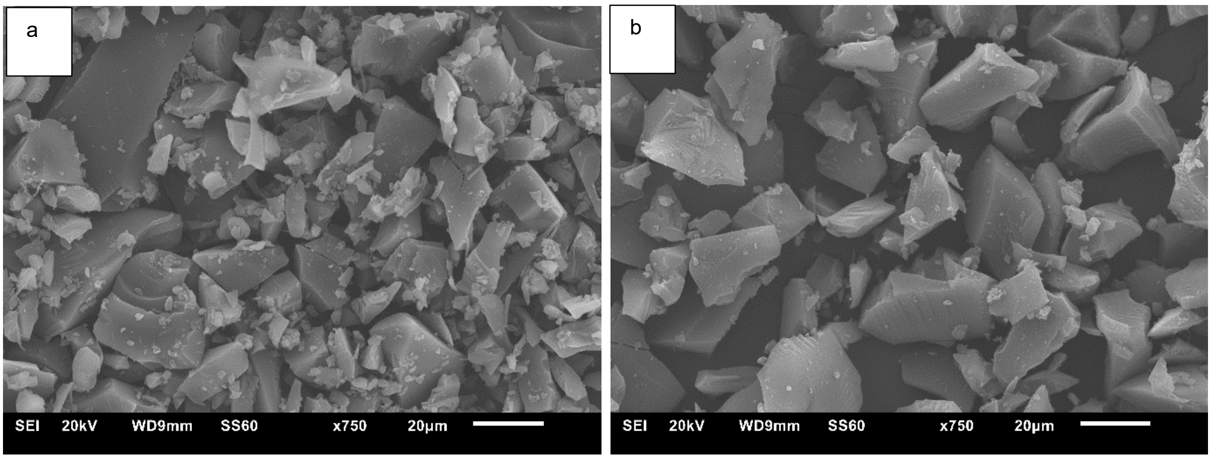

Figure S4: SEM images for a) CTF-1-400 and b) CTF-1-600.

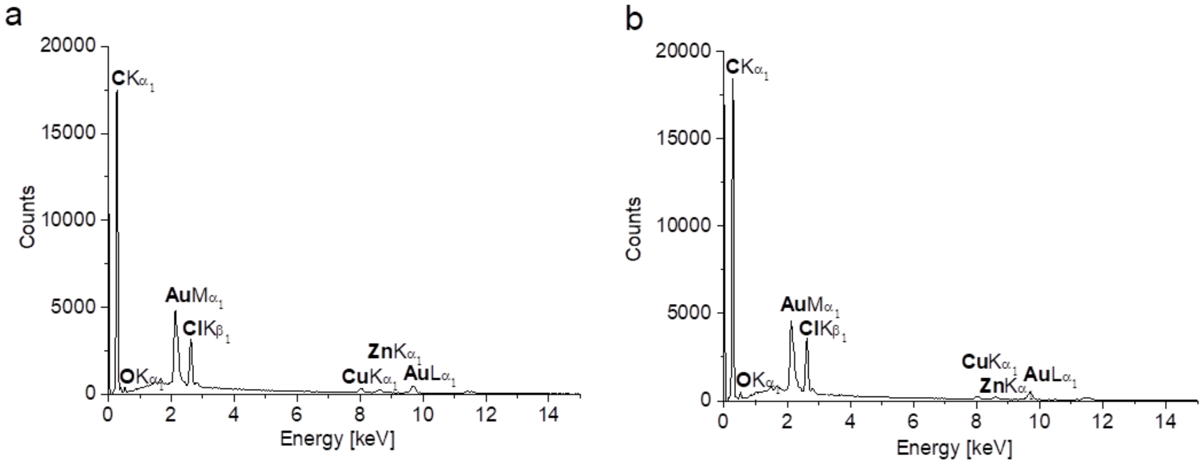

Figure S5: EDX analysis for (a) CTF-1-400 and (b) CTF-1-600.

Characterization of Ni/CTF-1 composites

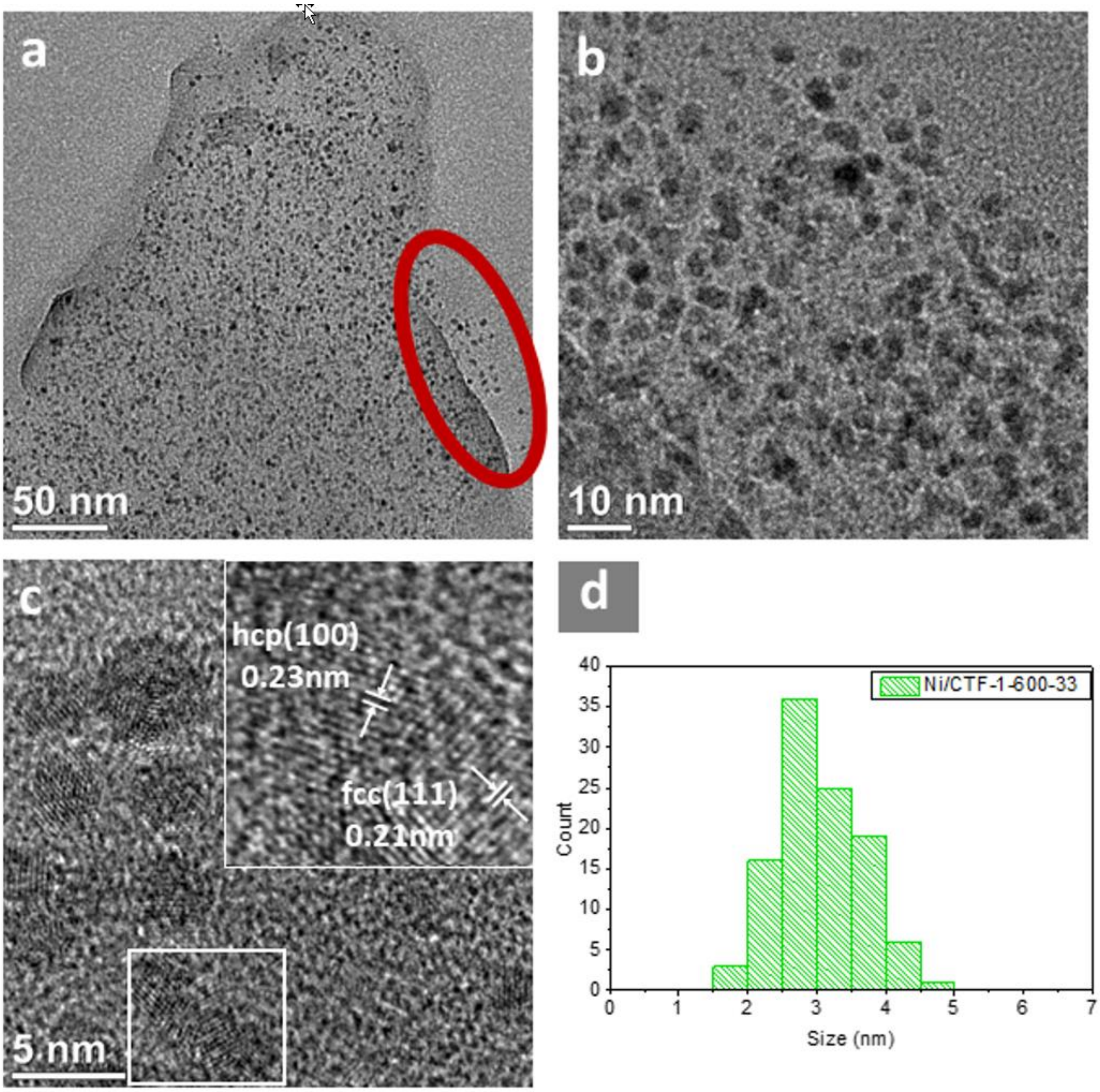

Figure S6: (a–c) TEM images of Ni/CTF-1-600-33 with (d) histogram giving the average diameter of 3.0 ± 0.6 nm. The red circle in (a) shows Ni NPs that lie in direct proximity to the support, having been "washed off" from the CTF to the carbon grid, probably at the time of sample preparation. This is an indication that at least some NPs are located on the surface.

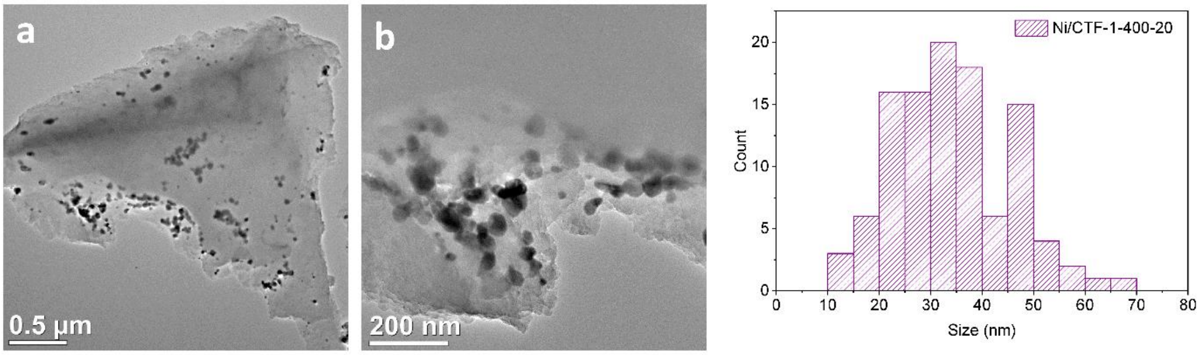

Figure S7: (a,b) TEM images of Ni/CTF-1-400-20 with histogram giving the average diameter of 35 ± 13 nm.

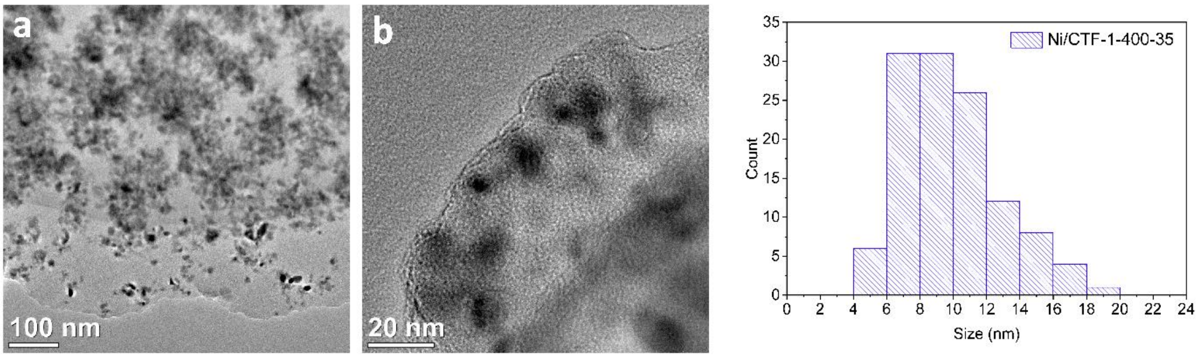

Figure S8: TEM images of Ni/CTF-1-400-35 with the average diameter of 10 ± 3 nm.

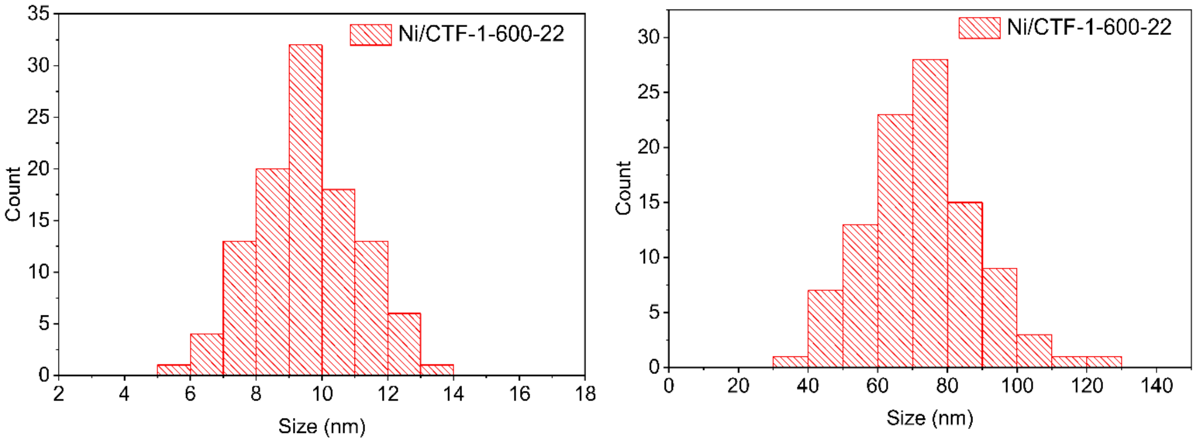

Figure S9: Nickel nanoparticle size distribution of Ni/CTF-1-600-22 with an average diameter of 10 ± 2 nm and aggregated nanoparticles with an average diameter of 72 ± 16 nm.

To further show the presence of particles on the surface, we present in Figure S10 TEM images with a “side view” of the materials so that the Ni NPs are imaged to stick out from the surface. Figure S10 clearly shows Ni nanoparticles that are sticking out over the edge of the CTF. This means at least some particles are at the surface. In Figure S10c, single nanoparticles are even somewhat bordered within the carrier but protrude with a part or a surface. This observation does not disprove that some particles might be encapsulated by the CTF. Additionally, XPS, which is a surface technique (Figure 5 and Figures S15–S18), confirms the presence of Ni on or very close to the surface of the CTF material.

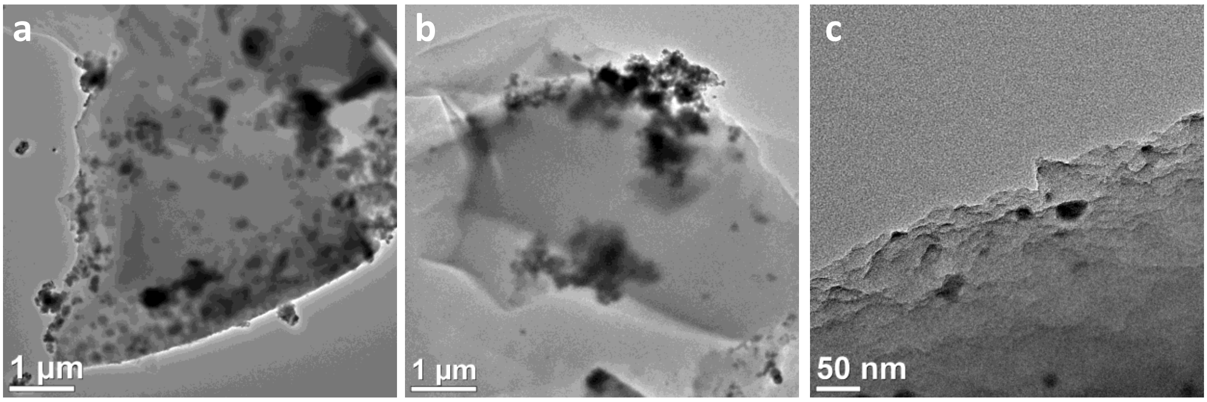

Figure S10: TEM pictures of (a) Ni/CTF-1-600-33 and (b,c) Ni/CTF-1-400-20.

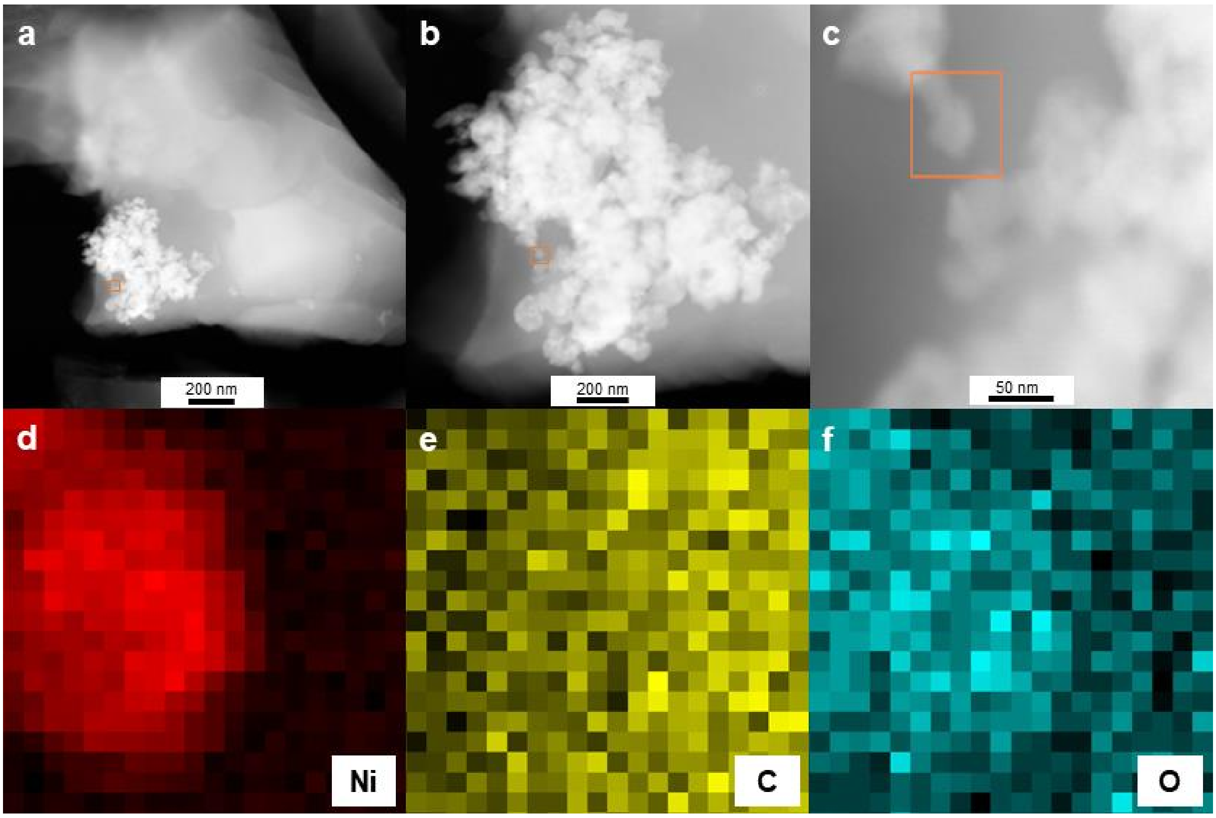

Figure S11: (a–c) STEM images at different magnifications and EDX elemental mapping of Ni/CTF-1-600-22, showing a CTF structure with supported Ni NPs. An accumulation of Ni NPs was selected and the elemental composition of the area inside the orange square was investigated. (d) Nickel is shown in red, (e) carbon is shown in yellow and (f) oxygen is shown in blue.

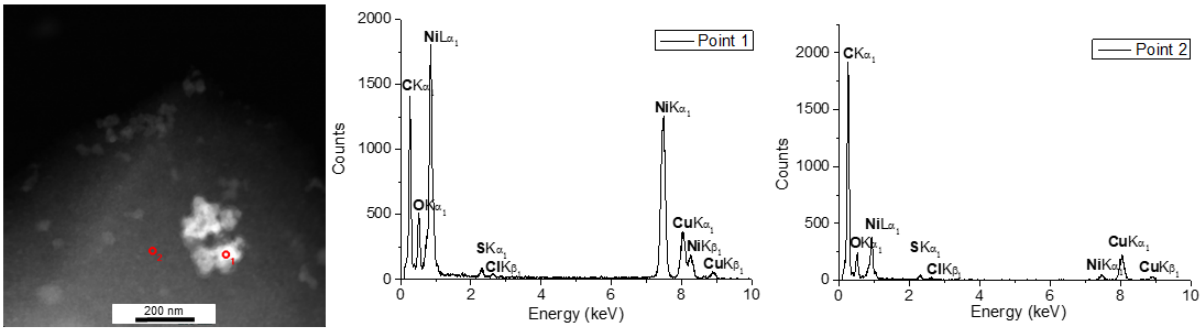

Figure S12: STEM image and point EDX analysis of a Ni NP agglomerate (point 1) and the CTF support (point 2) to verify that nickel is found not only as larger nanoparticles but also across the seemingly bare surface. An estimated atomic fraction of Ni of 64% is found, whereas 36% is found for O. This gives a ratio of Ni/O ≈ 1.8:1 (to be compared with Ni/O = 1:1 and $Ni/(OH)_2$ = 1:2, which indicates that a significant amount of Ni at point 1 is not oxidized (see the estimation details below).

Estimation of atomic Ni/O ratio

The Ni K lines were evaluated, not the Ni L line, since the latter has an unresolved overlap with the Cu L line and is therefore not reliable for concentration measurements. The Ni K and O K line intensities are measured after background subtraction. The background estimation was done by interpolation from neighboring channels, where no X-ray emission is expected. The composition of Ni and O was estimated using the Cliff–Lorimer method [6] for very thin foils, with k-factors of *k*(Ni K) = 1.508 and *k*(O K) = 1.889 [7]. The relative errors of the estimated atomic fractions and ratios are not better than 5% including systematic and statistical errors of measurement and evaluation. For the net values the difference of the two measurements was calculated and re-evaluated for mass fractions and from there to atomic fractions. By this, we assume, that the spectrum measured at point 1 also has contributions from the underlying CTF and that these contributions can be estimated from the counts measured at point 2.

Point 1 (particles above CTF):

- intensity (Ni K): 39000 +/- 1000
- intensity (O K): 8200 +/- 500
- atomic fraction Ni: 51%
- atomic fraction O: 49%
- ratio Ni/O : 1.0

Point 2 (CTF near the particles) :

- intensity (Ni K): 1200 +/- 200
- intensity (O K): 3600 +/- 300
- atomic fraction Ni: 7%
- atomic fraction O: 93%
- ratio Ni/O : 0.08

Net values for point 1, assuming the set of particles is on a CTF with identical Ni and O content:

- intensity (Ni K): 38000 +/- 1000
- intensity (O K): 4600 +/- 600
- atomic fraction Ni: 64%
- atomic fraction O: 36%
- ratio Ni/O : 1.8

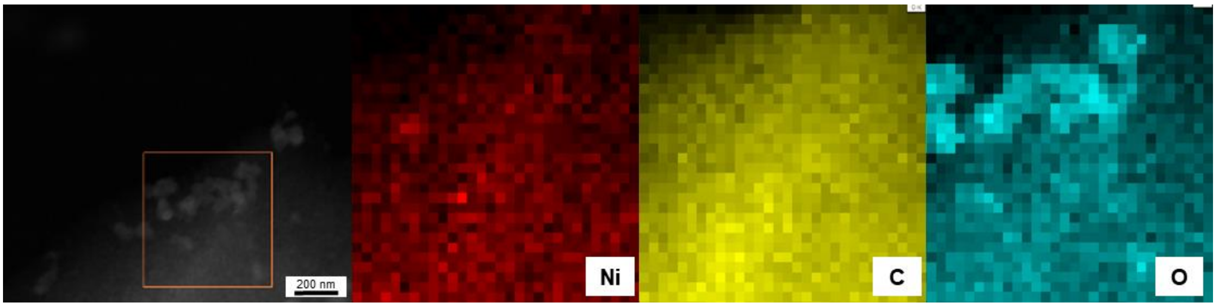

Figure S13: STEM image and EDX elemental mapping of Ni/CTF-1-600-22 showing nickel (in red), carbon (in yellow) and oxygen (in blue). The orange window in the STEM image displays the area of EDX mapping.

Porosity characterization

Table S2: Pore volumes of CTF and Ni/CTF materials.

Catalyst	CTF-1-400	Ni/CTF-1-400-20	Ni/CTF-1-400-35	CTF-1-600	Ni/CTF-1-600-22	Ni/CTF-1-600-33
Total pore volume V_{total} (cm^3/g)[a]	0.45	0.30	0.15	1.06	0.48	0.45
Micropore volume V_{mic} (cm^3/g)[b]	0.33	0.01	0.07	0.13	0.05	0.03
$V_{\text{mic}}/V_{\text{total}}$	0.73	0.03	0.46	0.12	0.10	0.06

[a]The total pore volumes were determined at p/p_0 = 0.95 from the adsorption branch for for pores ≤40 nm. [b]Micropore volume derived from t-plot analysis of the N_2 adsorption isotherm at p/p_0 = 0.2–0.5.

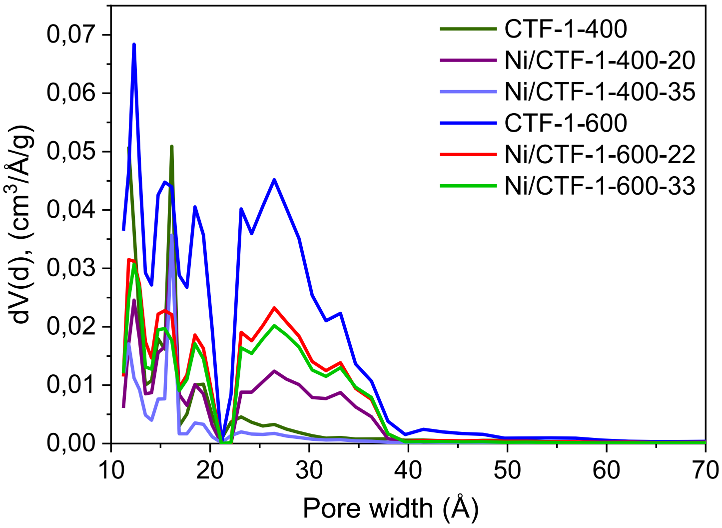

Figure S14: Pore size distribution from N_2 adsorption isotherm analysis (at 77 K).

X-ray photoelectron spectroscopy (XPS)

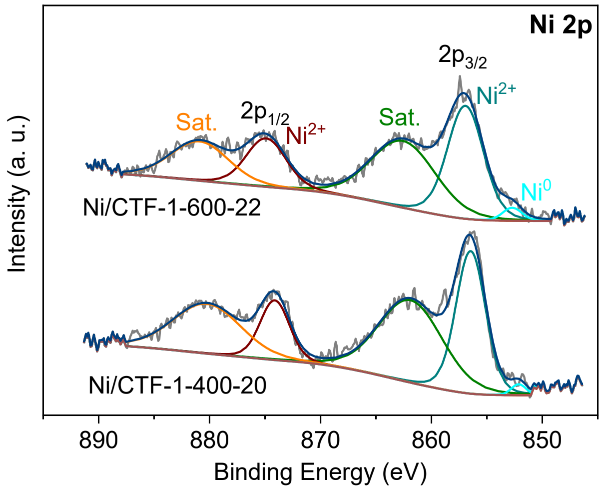

Figure S15: XPS measurement of Ni/CTF-1-400-20 and Ni/CTF-1-600-22 with the corresponding deconvoluted Ni 2p spectra.

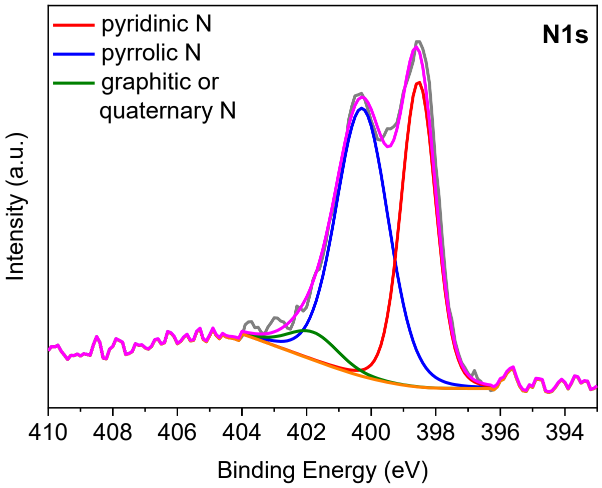

Figure S16: XPS measurement of CTF-1-400 with deconvoluted N 1s spectrum.

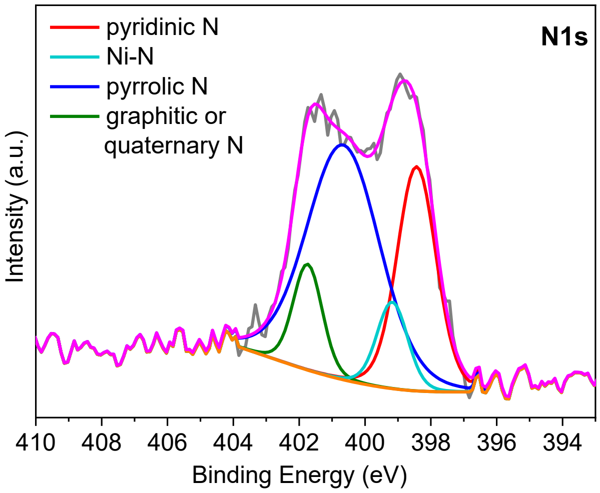

Figure S17: XPS measurement of Ni/CTF-1-400-20 with deconvoluted N 1s spectrum.

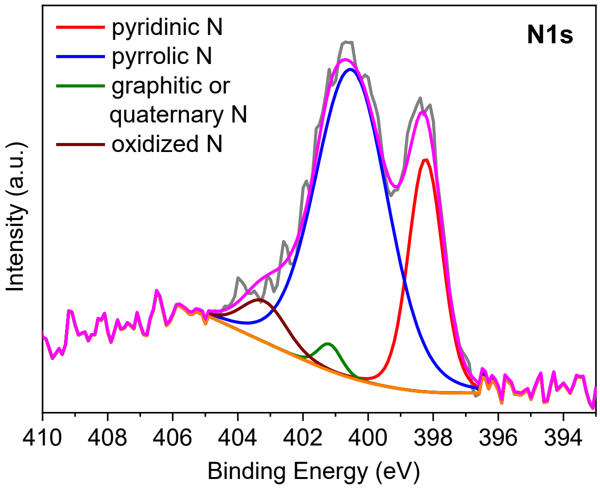

Figure S18: XPS measurement of CTF-1-600 with deconvoluted N 1s spectrum.

Tafel plots for OER and ORR

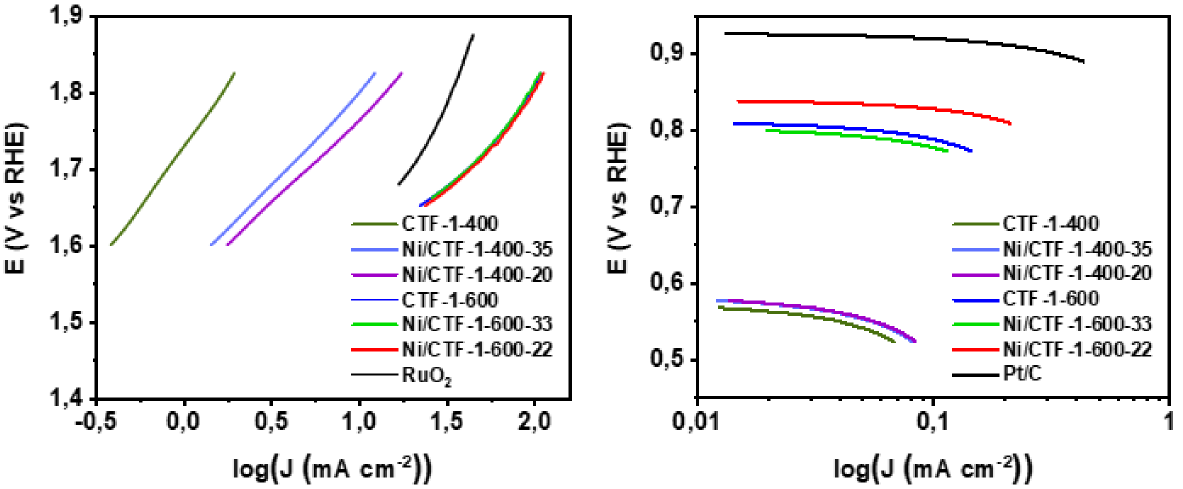

Figure S19: Tafel plots for OER (left) and ORR (right) results.

Table S3: Comparison of supported nickel/carbon material based OER catalysts.

Sample	Synthesis	Temperature (°C), time, atmosphere	Ni content (method)	KOH Electrolyte conc. (mol/L)	overpotential (at 10 mA/cm^2 vs. RHE) (mV)	Onset potential (V)	Ref.
Ni/CTF-1-600	Ionothermal, microwave rad.	230, 10 min, N_2	22 wt% (AAS)	1.0	374	1.51	This work
Ni@N-CNT-600 [a]	MOF synthesis, Pyrolysis	600, 3h, N_2	7.3 at% (XPS)	0.1	460	1.49	8
Ni@N-CNT-700	MOF synthesis, Pyrolysis	700, 3h, N_2	9.6 at% (XPS)	0.1	–	1.59	8
Ni@N-CNT-800	MOF synthesis, Pyrolysis	800, 3h, N_2	21.2 at% (XPS)	0.1	–	1.67	8
Ni/C [b]	Impregnation, pyrolysis	800, 1.5h, N_2	10.61 wt% (TGA)	0.1	420	1.59	9
Ni/NC [c]	Impregnation, pyrolysis	800, 1.5h, N_2	7.62 wt% (TGA)	0.1	390	1.56	9
Ni@graphene	MOF synthesis, annealing	600, 6h, Ar	74.10 wt% (EDX)	1.0	370	–	10

Ni@N-NC [d]	Pyrolysis of precursors	550, 3h then 700, 2h, Ar/N_2	not given	1.0	371	54	11
Ni@ketjenblack	Electrodeposition	not given	not given	1.0	340	–	12
Ni/carbon matrix	Complex grown on carbon, Pyrolysis	800, 5h, N_2	1 at% (EDX)	0.1	390	1.52	13
fcc-Ni@N-C [e]	MOF synthesis, Annealing	500, 2h, Ar	69 wt% (ICP-MS)	1.0	360	–	14
hcp-Ni@N-C	MOF synthesis, Annealing	400, 2h, Ar	71 wt% (ICP- MS)	1.0	305	–	14
Ni/N-CNTs [a]	Annealing	500, Ar then 700, 2h, Ar	1.73 wt% (XPS)	0.1	590	–	15
MWCNTs	purchased	–	–	0.1	650	–	15

Ni@single layer graphene	Chemical vapor deposition	700, 20 min, 50% H_2/Ar	32.8 wt% (ICP)	1.0 (NaOH)	~350	–	16
Ni@NC species [c]	Electrospinning, carbonization	800, 2h, N_2	14.5 wt% (TGA)	1.0	305	–	17
Ni-graphene film	Electrodeposition	50, 25 min	not given	0.1	392 @5mA cm^{-2}	1.56	18
Graphene	–	–	–	0.1	–	1.63	18**Fehler! Textmarke nicht definiert.**
Ni@NC_x [f]	MOF Synthesis, Pyrolysis	600, 1h, N_2 then 800, 1h, N_2	25.2 wt% (ICP-OES)	0.1	–	1.56	19

[a] N-CNT = N doped carbon nanotube, [b] C = carbon, [c] NC = nitrogen doped carbon, [d] N-NC= nitrogen doped nanocarbon [e] N-C = N doped carbon shells, [f] NC_x = graphitic layers coupling with a graphene sheet.

References

---

1 Kuhn, P.; Thomas, A.; Antonietti, M. *Macromolecules*, **2009**, *42,* 319–326.
2 Kuhn, P.; Forget, A.; Su, D.; Thomas, A.; Antonietti, M. *J. Am. Chem. Soc.*, **2008**, *130*, 13333–13337.
3 Hug, S.; Stegbauer, L.; Oh, H.; Hirscher, M.; Lotsch, B. V. *Chem. Mater.*, **2015**, *27*, 8001–8010.
4 Kuhn, P.; Antonietti, M.; Thomas, A. *Angew. Chem. Int. Ed.*, **2008**, *47*, 3450–3453.
5 Bhunia, A.; Dey, S.; Bous, M.; Zhang, C.; Rybinski, W.; Janiak, C. *Chem. Commun.*, **2015**, *51*, 484–486.
6 Lorimer, GW, Al-Salman, SA and Cliff, G 1977 The Quantitative Analysis of Thin Specimens: Effects of Absorption, Fluorescence and Beam Spreading in Developments in Electron Microscopy and Analysis 369–371 Ed. DL Misell The Institute of Physics Bristol and London.
7 k-factors for Ni-K and O-K are taken from the detector specific settings of the "TEM Image & Analysis" software, version 4.12, ThermoFisher Scientific, Eindhoven, The Netherlands.
8 Han, H.; Chao, S.; Yang, X.; Wang, X.; Wang, K.; Bai, Z.; Yang, L. *Int. J. Hydrogen Energy*, **2017**, *42*, 16149–16156.
9 Ren, J.; Antonietti, M.; Fellinger, T. P., *Adv. Energy Mater*., **2015**, *5*, 1401660.
10 Ai, L; Tian, T.; Jiang, J., *ACS Sustainable Chem. Eng.*, **2017**, *5*, 4771-4777.
11 Zhang, X.; Xu, H.; Li, X.; Li, Y.; Yang, T.; Liang, Y. *ACS Catal.*, **2016**, *6*, 580–588.
12 Lee, S. Y.; Jung, H.; Chae, S. Y.; Oh, H-S.; Min, B. K.; Hwang, Y. J., *Electrochimica Acta*, **2018**, *281*, 684-691.
13 Cui, C.; Ge, X.; An, T.; Li, B.; Wuu, D.; Tham, N. N.; Zhang, K.; He, Y.; Liu, Z., *Inorg. Chem. Front*., **2019**, *6*, 1873.
14 Wang, C.; Wang, Y.; Yang, H.; Zhang, Y.; Zhao, H.; Wang, Q. *Small*, **2018**, *14*, 1802895.
15 Liu, Y.; Jiang, H.; Zhu, Y.; Yang, X.; Li, C. *J. Mater. Chem. A*, **2016**, *4*, 1694–1701.
16 Cui, X.; Ren, P; Deng, D.; Deng, J.; Bao, X., *Energy Environ. Sci*., **2016**, *9*, 123.
17 Li, H.; He, Y.; Yang, Q.; Wang, J.; Yan, S.; Chen, C.; Chen, J., *J. Solid State Chem.*, **2019**, *278*, 120843.
18 Pu, Z.; Liu, Q.; Asiri, A. M.; Sun, X., *J. Appl. Electrochem*., **2014**, *44*, 1165-1170.
19 Zhu, J.; Xiao, M.; Zhang, Y.; Jin, Z.; Peng, Z.; Liu, C.; Chen, S.; Ge, J.; Xing, W. *ACS Catal*., **2016**, *6*, 6335–6342.

3.2 Highly-Efficient Oxygen Evolution Electrocatalyst Derived from Metal-Organic Framework and Ketjenblack Carbon Material

Secil Öztürk, Gun-hee Moon, Alex Spieß, Stefan Roitsch, Harun Tüysüz, Christoph Janiak

ChemSusChem **2021**, submitted.

Metal organic frameworks (MOFs) are crystalline, porous materials that are built from metal atoms/clusters and bridging organic ligands. They possess many interesting and desired properties for catalysis such as open metal sites in the skeleton, high surface area, tunable structure and uniform porosity. MOFs are recently come into focus also for electrochemical OER. MOFs are utilized in electrocatalysis as pristine MOFs, MOF composites, MOF derivatives or as support to load functional moieties. Since pristine MOFs generally have poor electrical conductivity and stability, combination of MOF and conductive supports is a promising strategy to get enhanced performance for electrocatalysis. Here, we synthesized neat Ni(Fe)-MOF-74 and Ni(Fe)-MOF/KB through one-step solvothermal reaction at 120 °C for 24h. For comparison, we also synthesized Ni(Fe)$(OH)_2$ and Ni(Fe)$(OH)_2$/KB with same procedure but without any linker addition. After intensive characterization, all materials were tested for electrochemical OER. Ni(Fe)-MOF/KB displayed a remarkable OER performance by requiring 274 mV overpotential to reach 10 mA/cm^2 and having a small Tafel slope of 40.4 mV/dec. This activity outperforms the pristine Ni(Fe)-MOF-74, Ni(Fe)$(OH)_2$, Ni(Fe)$(OH)_2$/KB and many other reported OER catalysts including commercial ones. Furthermore, this is the first time in the literature that a MOF/Ketjenblack composite is studied for OER and found to be highly efficient and promising electrocatalyst.

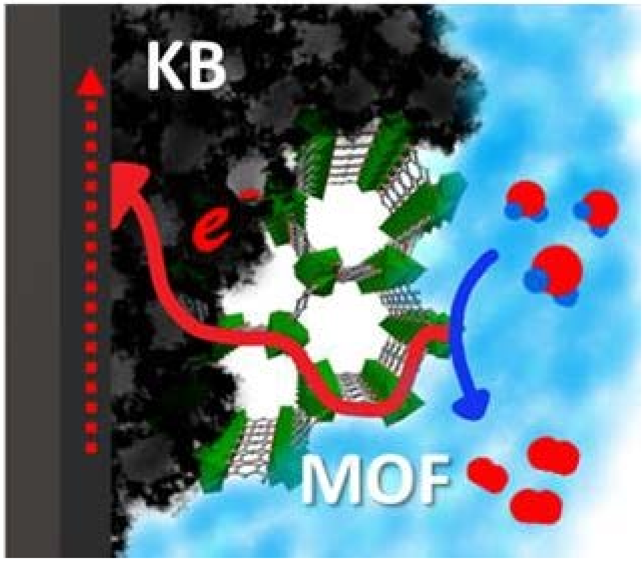

Author`s contribution to the publication:

- Comprehensive and independent literature research and planning of the research.
- Idea, concept, experimental work in the laboratory and characterization of the materials (except the work listed below).
- Drawing of all figures, graphs and tables (except the electrochemical data).
- Evaluation of all results and writing the manuscript.
- Editing of the manuscript regarding the reviewer`s comments.
- Electrochemical tests were performed, corresponding graphs were prepared and corresponding part in manuscript was written by Dr. Gun-hee Moon.
- TEM, STEM/EDX measurements were performed by Stefan Roitsch.
- SEM/EDX measurements were performed by Alex Spieß.
- Final coordination of the manuscript was done together with the comments from all co-authors.
- The manuscript draft and revised manuscript was corrected and submitted to the international journal “*ChemSusChem*” together with Prof. Dr. Christoph Janiak.

Highly-Efficient Oxygen Evolution Electrocatalyst Derived from Metal-Organic Framework and Ketjenblack Carbon Material

Seçil Öztürk,[a],† Gun-hee Moon,[b,d],† Alex Spieß,[a] Stefan Roitsch,[c] Harun Tüysüz*[b] and Christoph Janiak*[a]

Abstract: The metal-organic framework (MOFs) Ni(Fe)-MOF-74 could be prepared in-situ and in a one-pot solvothermal method with the highly conductive carbon material ketjenblack (KB). The composite material indicates a remarkable electrochemical oxygen evolution reaction (OER) performance where the overpotential at 10 mA/cm^2 and the current density at 1.7 V_{RHE} are recorded as 0.274 V_{RHE} and 650 mA/cm^2, respectively, in 1 mol/L KOH. In particular, the activation of nickel iron clusters constituting MOF structures under applying anodic bias steadily boost the OER performance, and the further enhancement is achieved by the synergetic behavior of KB. This simple strategy to design highly-efficient electrocatalysts with utilizing readily available precursors and carbon materials will leverage the products of diverse organometallic complexes into the electrode fabrication with a high energy conversion efficiency.

Introduction

The depletion of fossil fuels and their increasing environmental issues upon their burning are requiring efficient renewable energy conversion systems.[1] The photovoltaic-assisted water electrolysis is an ideal method to obtain (green) hydrogen (H_2) that can be used as fuel, building block in chemical industry like in ammonia synthesis or further conversion to methanol and methane (power-to-gas) as well as for mobile fuel cell applications.[2] Electrocatalytic water-splitting consists of two half reactions, a hydrogen evolution reaction (HER; $2H^+ + 2e^- \rightarrow H_2$, 0.00 V_{RHE}) and an oxygen evolution reaction (OER; $4\ OH^- \rightarrow 2\ H_2O + O_2 + 4e^-$, 1.23 V_{RHE}). Among both reactions, the OER is more challenging since the O=O bond formation involves a four-electron transfer with the kinetics giving rise to a high overpotential.[3,4] Therefore, functional electrode materials as electrocatalysts need to be developed to lower the high kinetic barrier of the OER and thus, to optimize the water-to-hydrogen conversion efficiency.[5] Noble metal based materials (Pt, Ir, Ru) show a good OER activity, yet suffer from scarcity and high cost.[6,7] Consequently, many studies focus on the development of non-noble metal catalysts based on earth-abundant elements, such as cobalt, iron, nickel, manganese as nanoparticles,[8,9] their oxides,[10,11,12] sulfides,[13,14] phosphides,[15,16] etc. Transition metal ions in oxides or complexed forms (e.g., hydroxide, phosphate, bipyridine, etc.) can be turned into a high-valent oxidation state through applying an anodic bias, which is responsible for cleaving water molecules.[17] One example is that Co^{2+} complexed with phosphate and $Co^{2+/3+}$ present in cobalt (oxide)hydroxide can be oxidized to unstable Co^{4+} by applying voltage, which accelerates the oxidation of water.[18,19] Recently, the research trend on the catalyst preparation for alkaline water electrolysis has moved from crystalline metal oxide to amorphous metal (oxide)hydroxide materials due to their facile synthesis and high OER activities.[20,21]
In particular, huge efforts have been devoted to investigate nickel or cobalt (oxide)hydroxides, whose activities can be easily tuned by the activation in terms of either accepting iron impurities from the electrolyte or iron elements intentionally introduced in the structure.[22,23] This hints at the advantage to combine amorphous nickel- or cobalt-based catalysts with iron in composite materials towards electrocatalytic water oxidation.

Recently, metal-organic frameworks, that are crystalline porous materials built from metal atoms/clusters and bridging organic ligands, are utilized as promising precursors or templates for the construction of new electrocatalysts.[24] The catalytic properties of open metal sites has drawn a significant attention in the field of electrochemistry covering water-splitting, oxygen reduction, carbon dioxide reduction, urea oxidation, nitrogen reduction, etc.[25,26,27,28] However, the drawbacks of MOFs are (i) low electrical conductivity,[29] (ii) mass transport problem of reactants, products, and electrolyte ions from/to pores, (iii) lack of stability especially in highly acidic or alkaline aqueous environments.[30] Therefore, electrocatalyst studies often use a MOF surface as a catalyst support or use the post-synthetic calcination (pyrolysis) of MOFs at a high temperature to yield structured metal oxide materials with a role of organic linkers as a template.[31,32,33]

In order to increase the electrical conductivity and structural stability, MOFs can be combined with more conductive materials such as graphene,[34] carbon nanotubes[35] or ketjenblack carbon (KB).[36] Among those carbon-based materials, the ketjenblack has been used as an additive or a support in batteries and fuel cells since it has a high specific surface area up to 1400 m^2/g, excellent

---

[a] S. Öztürk, A. Spieß, Prof. Dr. C. Janiak
Institut für Anorganische Chemie und Strukturchemie, Heinrich-Heine-Universität Düsseldorf
Universitätsstraße 1, 40225 Düsseldorf, Germany
E-mail: janiak@uni-duesseldorf.de
[b] Dr. G-h. Moon, PD Dr. Harun Tüysüz
Max-Planck-Institut für Kohlenforschung, Heterogeneous Catalysis and Sustainable Energy
Kaiser-Wilhelm-Platz 1, 45470 Mülheim an der Ruhr, Germany
E-mail: tueysuez@kofo.mpg.de
[c] Dr. S. Roitsch
Department für Chemie, Universität zu Köln
Greinstr. 4-6, D-50939 Köln, Germany
[d] Dr. G-h. Moon
Extreme Materials Research Center, Korea Institute of Science and Technology (KIST)
Seoul, South Korea

† These authors contributed equally to this work. * Corresponding authors
Supporting information for this article is given via a link at the end of the document.

charge transfer properties and high electrochemical stability. Until now only a few studies about MOF/KB composites can be found in the literature, however, those materials have not been implemented for OER. For instance, Wang et al. designed a polyoxometalate (POM) based MOF hybridized with KB and used this as an electrochemical sensing catalyst for nonenzymatic H_2O_2 detection.[37] In another study, Peng et al. used a POM based MOF to support Pt nanoparticles and then mixed this material with KB to form a composite which exhibits a remarkable HER performance.[38] Huang et al. developed the first non-pyrolized Fe-N coordination based MOF/KB composites as efficient and stable oxygen reduction reaction catalysts.[39] These studies indicated the potential of this new class of materials and encouraged us to investigate a MOF/KB composites for electrochemical OER.

The Ni-MOF-74 ($[Ni_2(DHTA)(H_2O)_2]$, DHTA = 2,5-dihydroxyterephthalate) made up of NiO_6 octahedra linked with DHTA (see Scheme S1, SI) is a robust MOF material that is stable in aqueous solution. It has been already shown to be a good OER electrocatalyst with the advantages of adjustable divalent metal nodes in the structure and a high density of potential open metal sites.[40] Ni-MOF-74 has one-dimensional channels with aperture diameters of about 1 nm that are large enough for diffusion of OER substrates. Moreover, it was proven that heterometallic, metal-doped Ni-MOF-74 exhibited enhanced OER activity compared to monometallic Ni-MOF-74. Especially, Fe incorporation or doping has been shown to be very effective on improving the OER performance.[41,42,43,44]

Herein, we combined physicochemical properties of iron-containing Ni-MOF-74 and KB in a composite material (denoted as Ni(Fe)-MOF/KB) via a simple one-step solvothermal method. The KB colloidal particles are a very good conductive support that can interact with MOFs via the condensation between surface hydroxyl groups but also via the van der Waals force of aromatic species or hydrogen bonds. The composite material indicated excellent performance for electrochemical OER in alkaline condition by requesting an overpotential of only 0.274 V to reach 10 mA/cm^2 and delivers a current density of 650 mA/cm^2 at 1.7 V_{RHE}.

Results and Discussion

Ni(Fe)-MOF-74 and ketjenblack (KB) composite were simply combined during the in-situ MOF synthesis as described in Scheme 1 via a one-step solvothermal method at 120 °C for 24 h from a mixture of $Ni(NO_3)_2{\cdot}6H_2O$, $Fe(OAc)_2$, 2,5-dihydroxyterephthalic acid (H_2DHTA) and KB in a DMF/EtOH/H_2O solution/dispersion. In order to introduce iron into the structure of Ni-MOF-74, $Fe(OAc)_2$ was added by aiming a molar Ni to Fe ratio of 32:1. For comparison, we also synthesized pristine Ni(Fe)-MOF-74,[45] $Ni(Fe)(OH)_2$ and $Ni(Fe)(OH)_2$/KB samples. Our previous electrocatalytic studies had revealed that the activation of nickel-based catalysts was negligible under iron-free conditions, very effective with a low iron content while an excess amount of iron decreased the OER activity.[41] Optimized Ni: Fe molar ratios of 32:1 for Ni-Fe oxide materials[41], 22:1 for Ni(Fe)-MOF-74/NF (NF = nickel foam)[42] and 53:1 for Fe_2O_3@Ni-MOF-74 were shown to be the optimized OER electrocatalysts.[46] The iron content in the synthesized Ni(Fe)-MOF-74 and $Ni(Fe)(OH)_2$ was post-synthetically quantified by flame atomic absorption spectroscopy (AAS), giving the Ni(Fe)-MOF-74 with a Ni:Fe ratio of 31:1 and the nickel(iron) hydroxide with a Ni:Fe ratio of 32:1 (Table S1, SI). Based on the AAS-determined metal wt%, the mass fractions of the metal compounds in the KB composites were calculated to be as 47.6 wt% Ni(Fe)-MOF-74 and 52.4 wt% KB for Ni(Fe)-MOF/KB and 53.4 wt% $Ni(Fe)(OH)_2$ and 46.6 wt% KB for $Ni(Fe)(OH)_2$/KB.

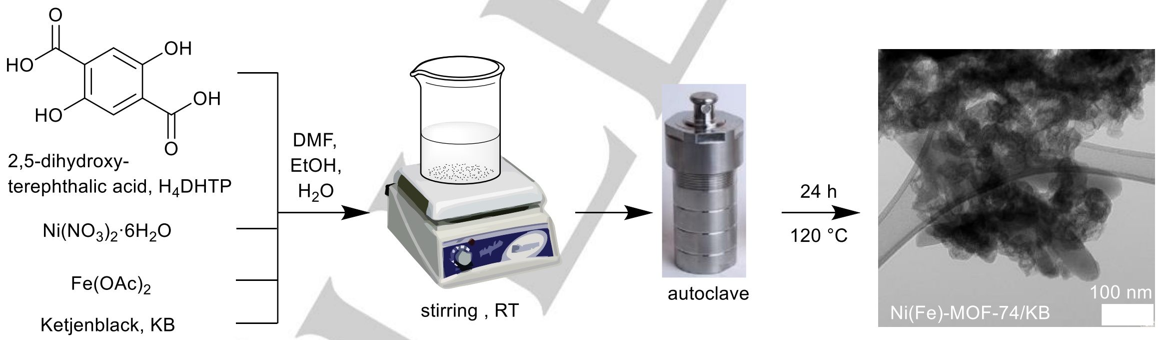

Scheme 1. Schematic illustration of the Ni(Fe)-MOF/KB composite synthesis

Powder X-ray diffraction (PXRD) patterns of Ni(Fe)-MOF-74, KB, Ni(Fe)-MOF/KB, $Ni(Fe)(OH)_2$ and $Ni(Fe)(OH)_2$/KB are compared in Figure 1a. The PXRD pattern of Ni(Fe)-MOF-74 and Ni(Fe)-MOF/KB show the same reflexes as the simulated pattern of Ni-MOF-74[47] thereby showing that the in-situ synthesis with largely amorphous KB did not affect significantly the MOF crystal growth and structure.[48] $Ni(Fe)(OH)_2$ and $Ni(Fe)(OH)_2$/KB exhibit the reflexes of α-$Ni(OH)_2$.[49] For all samples, the PXRD pattern of iron (oxide)hydroxide was not observed at all, indicating that iron was well-incorporated in the structure of Ni-MOF-74 instead of its self-agglomeration. In pristine KB, three broad peaks corresponding to (100), (002), and (101) of amorphous carbon were recorded, and no residue of the iron and nickel salts was observed in the final products (Figure S1).[50] The reflexes of α-$Ni(OH)_2$ only appeared in $Ni(Fe)(OH)_2$ and $Ni(Fe)(OH)_2$/KB, while the coordination of Ni^{2+} with the hydroxyl and carboxylic groups of DHTA directed the crystallization of Ni-MOF-74. In the Fourier transform infrared (FT-IR) spectra (Figure 1b), Ni(Fe)-MOF-74 and Ni(Fe)-MOF/KB display the same characteristic bands in the fingerprint region which are in a good agreement with the literature.[51] Several peaks at 1556, 1442, 1408, 1363, 1240, 1197, 1126, and 888 cm^{-1} originated from the DHTA linkers.[51,52] A few peaks were slightly red-shifted in Ni(Fe)-MOF/KB from Ni(Fe)-MOF-74 (Figure S2b), in particular the red-shift of C-H bending in aromatic ring indicates the existence of van der Waals force between MOF and KB caused by either C-H–π or π–π interaction.[53,54] KB has no remarkable IR signals. Ni(Fe)(OH)$_2$ and Ni(Fe)(OH)$_2$/KB show the characteristic bands of α-Ni(OH)$_2$ (at 644 and 1635 cm^{-1}).[55]

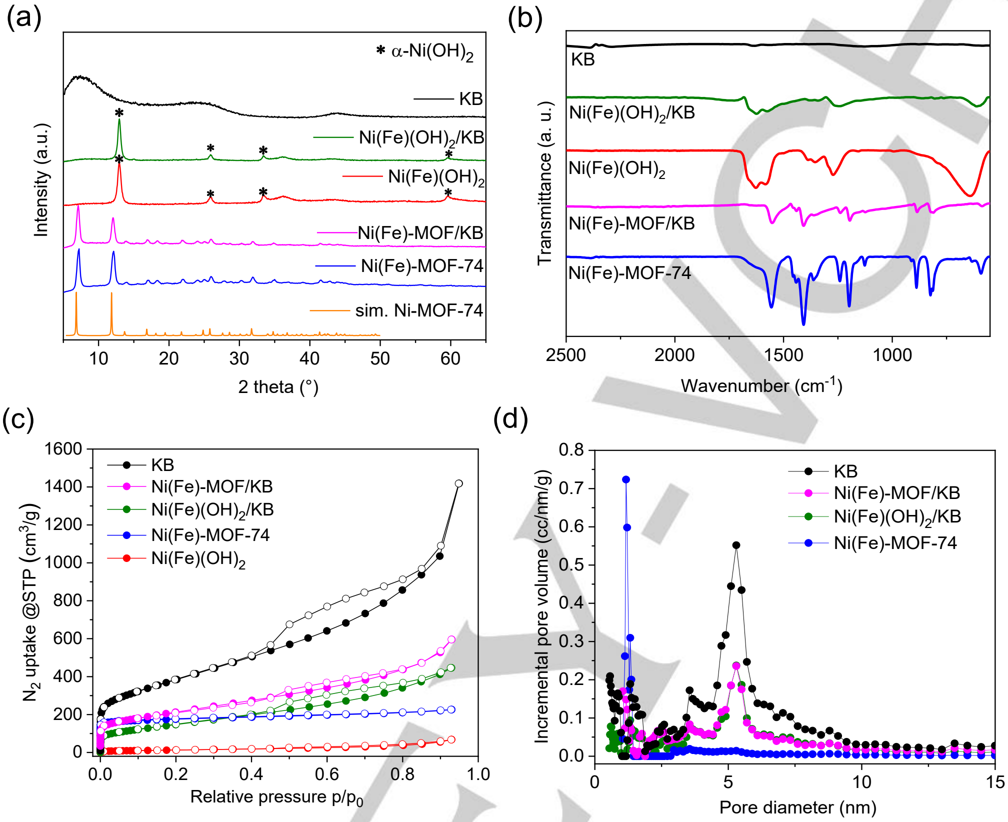

Figure 1. (a) PXRD patterns of simulated Ni-MOF-74 (CCDC number: 1494751), experimental Ni(Fe)-MOF-74, KB, Ni(Fe)-MOF/KB, Ni(Fe)(OH)$_2$ and Ni(Fe)(OH)$_2$/KB. The XRD patterns of α-Ni(OH)$_2$ are marked by * (ICDD no: 38-0715). (b) FT-IR spectra of Ni(Fe)-MOF-74, Ni(Fe)-MOF/KB, Ni(Fe)(OH)$_2$, Ni(Fe)(OH)$_2$/KB, and KB. (c) Nitrogen sorption isotherms at 77 K (solid and empty symbols are for ad- and desorption, respectively), and (d) pore size distribution of the Ni(Fe)(OH)$_2$/KB, KB, Ni(Fe)-MOF-74 and Ni(Fe)-MOF/KB.

The specific Brunauer-Emmett-Teller (BET) surface areas of the materials were derived from nitrogen-sorption isotherms at 77 K (Figure 1c). Ni(Fe)-MOF-74 has a surface area and pore volume of 684 m^2/g and 0.34 cm^3/g, respectively, which are close to the reported values (literature 820 m^2/g, 0.29 cm^3/g for NiCoFe-MOF-74).[56] Ni(Fe)-MOF-74 shows a type I isotherm with a sharp gas uptake at low relative pressure followed by a plateau revealing its microporosity.[57] KB is a porous carbon material with a BET surface area of 1399 m^2/g, a specific pore volume of 2.2 cm^3/g and mesopores around 5 ± 2 nm. KB exhibits an adsorption isotherm branch as a composite of type I and II and an H4 hysteresis loop upon desorption, both being often found for micro-mesoporous carbons.[57] As expected, the surface area of non-porous Ni(Fe)(OH)$_2$ was only 50 m^2/g. The nitrogen sorption isotherms and BET-surface areas of the composites Ni(Fe)-MOF/KB and Ni(Fe)(OH)$_2$/KB can be seen as a combination of the isotherms of the individual mass-weighted components. This superposition also holds for the pore-size distribution and cumulative pore volume curves of the individual components in the composites (Figure 1d, Figure S3). The bimodal pore size distribution of Ni(Fe)-MOF/KB with maxima at ~1 nm and ~5 nm reflects the contributions from the MOF and KB. Consequently, the apparent BET surface area and pore volume of the Ni(Fe)-MOF/KB composite with 770 m^2/g and 0.90 cm^3/g, respectively is higher than the surface area and pore volume of neat Ni(Fe)-MOF-74. Yet, the observed BET area for Ni(Fe)-MOF/KB is significantly lower than its calculated apparent BET (1059 m^2/g) as determined from the sum of the mass-weighted S(BET) of the KB (52 wt%) and MOF (48 wt%) (eq. 1):

$$\mathrm{S(BET)calc.} = \frac{\text{wt\% of KB}}{100} \times \mathrm{S(BET, KB)} + \frac{\text{wt\% of MOF}}{100} \times \mathrm{S(BET, MOF)} \qquad \text{(Ia)}$$

Also, the BET surface area of the composite Ni(Fe)(OH)$_2$/KB with 547 m^2/g, is significantly lower than the estimated value (679 m^2/g) based on the 53 wt% contribution of Ni(Fe)(OH)$_2$ and the 47 wt% contribution of KB. This can be due to pore blocking effects or the MOF or Ni(Fe)(OH)$_2$ formation in the mesopores of KB.

The high-resolution Ni 2p XPS spectra of Ni(Fe)(OH)$_2$/KB and Ni(Fe)-MOF/KB revealed that the oxidation state of Ni^{2+} is predominant, which supports the formation of Ni(II)-hydroxide (Figure S5). The peak of Fe 2p was not clear due to the strong noise and the interference of C 1s and O 1s from residual counter anions of precursors, adsorbed water and carbon dioxide, etc. hindered a further comparison.

The scanning electron microscopy (SEM) revealed that the materials have spherical nanoparticles with a homogenous particle size distribution of <0.1 µm particles for ketjenblack and a wider particle size distribution with irregular shaped particles for Ni(Fe)-MOF-74 and Ni(Fe)$(OH)_2$ in the 0.1-1 µm range (Figure S6a,b,c). In both composite materials, the particles are well covered by ketjenblack carbon. In Ni(Fe)-MOF/KB, there seems to be an intimate mixing which suppresses the aggregation between the MOF particles (Figure 2a). The irregular particles covered with wrinkled sheets in Ni(Fe)$(OH)_2$ were similar to the shape of $Ni(OH)_2$ that was already demonstrated in the literature (Figure S6c,d).[58] KB particles appeared to be randomly mixed with the Ni(Fe)$(OH)_2$ particles were predominantly observed in Ni(Fe)$(OH)_2$/KB, indicating a less intimate mixing (Fig. S6d). From SEM-elemental mapping (Figure S7) that visualizes more the surface composition, it is evident that the Fe mapping in the particles does not contrast well with the background. This suggests that the iron is incorporated inside the particles and not located near the surface.

High resolution transmission electron microscopy (HR-TEM) images reveal that the graphene-like carbon sheets of KB are well-mixed with the particles of Ni(Fe)-MOF-74 (Figure 2b-d). The scanning TEM (STEM) image and its superimposable elemental mappings visualized that nickel, iron, oxygen, and carbon were uniformly dispersed in Ni(Fe)-MOF/KB (Figure 2e), as was the case in Ni(Fe)-MOF-74 (Fig. S10a). A notable mismatch for carbon (i.e., the size of the area spotted by pink color was larger than the STEM image) in Figure 2e can be attributed to the background signal of KB. The elemental analysis obtained from the energy-dispersive X-ray (EDX) spectrum focused on the circle in Figure 2b yields an atomic ratio of Ni to Fe (32:1) going in line with SEM-EDX (Figure 2f, Table S1).

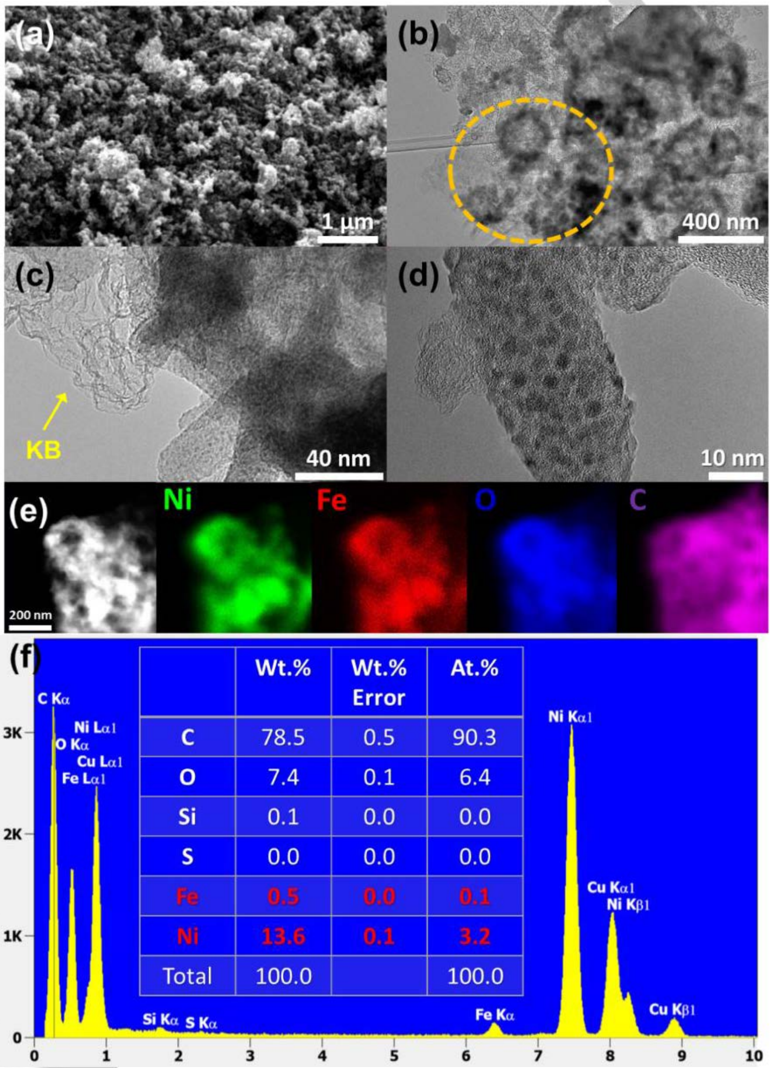

	Wt.%	Wt.% Error	At.%
C	78.5	0.5	90.3
O	7.4	0.1	6.4
Si	0.1	0.0	0.0
S	0.0	0.0	0.0
Fe	0.5	0.0	0.1
Ni	13.6	0.1	3.2
Total	100.0		100.0

Figure 2. (a) SEM image, (b-d) HR-TEM images, (e) STEM image with its elemental mapping for nickel, iron, oxygen, and carbon for Ni(Fe)-MOF/KB. The EDX scan in the encircled area in (b) gave a molar Ni:Fe ratio of 32:1 and (f) EDX spectrum with the composition for the selected area in (b) for Ni(Fe)-MOF/KB. Further TEM, HR-TEM images and STEM element mappings are given in Figure S9 and S10.

The electrocatalytic OER performance of the samples was checked and compared using a three-electrode system under rotation of the working electrode at 2,000 rpm in 1 mol/L KOH electrolyte. For the working electrode preparation, the samples were dispersed in the alcohol-water mixture in the presence of a Nafion binder by sonication and were loaded on the glassy carbon electrode (GCE) with a geometric area of 0.196 cm^2. As shown in Figure 3a, the current density of Ni(Fe)-MOF/KB from 1.5 to 1.7 V_{RHE} (i.e., the region of water oxidation, RHE = reversible hydrogen electrode) in linear sweep voltammetry (LSV) curves was much higher than that of other samples, and the enhancement effect by the introduction of KB was also clearly observed in Ni(Fe)(OH)$_2$/KB. Due to the continuous increase of OER activities with the number of LSV scans, the cyclic voltammetry (CV) with 50 mV/s from 0.7 to 1.6 V_{RHE} for 100 scans was carried out in order to reach the steady state of electrocatalysts. During CV scans, the current density collected at 1.7 V_{RHE} steadily rose for all samples except KB, which was saturated after 60 CVs (Figure 3b). The peaks from 1.2 to 1.5 V_{RHE} originated from the redox reaction of $Ni^{2+/3+}$ and were positively shifted, and at the same time the current density at 1.6 V_{RHE} was enhanced after 100 CVs (Figure S11), which are the typical sign of Fe impurity uptake from KOH electrolyte.[59] The oxidation peak of Ni(Fe)-MOF/KB, measured at the lowest voltage, was possibly due to the efficient conversion of Ni^{2+} to Ni^{3+} in terms of the interaction between KB and DHTA of the MOF. The activation of nickel-based electrocatalysts under applying anodic bias is a well-known phenomenon, being subject with either the intentionally added iron in nickel oxide structures or the adsorption of iron impurities on the nickel (oxide)hydroxide surface from the KOH electrolyte. According to the literature, the iron incorporated in active Ni sites can not only increase the conductivity but also change the electronic structure of NiOOH, lowering the kinetic barrier towards a highly efficient water oxidation.[22] In our previous report, it was also confirmed that the introduction of iron into nickel oxide and amorphous cobalt hydroxide significantly improved the OER activity, where the activation occurred under CVs and continuous application of an anodic bias, respectively.[41, 60] Consequently, the current density at 1.7 V_{RHE} and the overpotential to reach 10 mA/cm^2 were recorded as 650 mA/cm^2 and 0.274 V_{RHE}, respectively, for Ni(Fe)-MOF/KB after 100 CVs (Figure 3c). Considering the result that the current density of Ni(Fe)-MOF/KB over the typical water oxidation potential region (i.e., from 1.5 to 1.7 V_{RHE}) was three times higher than the sum of current densities for Ni(Fe)-MOF-74 and KB alone (e.g., 27 and 180 mA/cm^2 at 1.7 V_{RHE} for KB and Ni(Fe)-MOF-74, respectively), such a high OER performance should stem from the synergetic effect of KB to offset the drawbacks of Ni(Fe)-MOF-74. Moreover, the overpotential to reach 10 mA/cm^2 was much lower than that of KB and Ni(Fe)-MOF-74 (0.410 and 0.318 V_{RHE} for KB and Ni(Fe)-MOF-74, respectively). It is important to stress that carbon based materials get oxidized in higher applied voltage range under alkaline conditions and can contribute to the measured currents.[61] However, as seen in Figure 3a and 3b the activated current density at 1.7 V over KB is almost negligible in comparison to Ni(Fe)-MOF/KB. Therefore, it can be postulated that this high current density is obtained from the electrocatalytic OER.

The electrochemical kinetics on OER for the samples were evaluated by comparison of the Tafel slopes, a measure to determine how quickly the electrons are transferred against overpotential, derived from LSV curves after the activation (Figure 3d).[4] The Tafel slopes for KB, Ni(Fe)(OH)$_2$, Ni(Fe)-MOF-74, Ni(Fe)(OH)$_2$/KB, and Ni(Fe)-MOF/KB were calculated as 76.6, 77.0, 58.3, 65.8, and 40.4 mV/dec, respectively. Predictably, the Ni(Fe)-MOF/KB showed the lowest Tafel slope, and the introduction of KB was very simple but quite effective to break down the kinetic barrier for electron transfer processes.[62,63] The electrochemical impedance spectroscopy (EIS) was utilized to better understand the charge transfer behavior of samples. The diameter of the semicircle in Nyquist plots is related to the interfacial electron transfer resistance, where a small semicircle is typically observed when the charge transfer is favorable.[64] As seen in Figure 3e, the smallest semicircle was obtained in Ni(Fe)-MOF/KB, while the biggest one was exhibited in KB since the driving force for water oxidation was too weak without aid of Ni-Fe catalysts. The lowest resistance of Ni(Fe)-MOF/KB and the effect of KB on the charge transfer kinetics were consistent with the result of Tafel slopes in Figure 3d. For investigating the correlation between the surface area and the electrocatalytic activity, the polarization curves were normalized by the electrochemical active surface area (ECSA) and the BET surface area (Figure 3f). The ECSA of the catalysts was calculated by the double layer capacitance derived from CV analysis (Figure S12). As shown in Figure S9, the highest ECSA and BET surface area were obtained for KB, and the mismatch between them was severe in Ni(Fe)-MOF-74. Unexpectedly, the ECSA tended to decline as MOF was formed (i.e., Ni(Fe)(OH)$_2$ vs. Ni(Fe)-MOF-74 and Ni(Fe)(OH)$_2$/KB vs. Ni(Fe)-MOF/KB). The intrinsic properties of MOF, especially a pore size close to 1 nm and a hydrophobicity, might be disadvantageous for (i) a permeability of electrolyte ions into active sites, (ii) a diffusion of O_2 from inner pores to bulk electrolyte, and (iii) a wettability as well as low electrical conductivity. Based on Figure 3f, it was more clear to recognize the problems posed in each system, which should be overcome to achieve a high OER efficiency; (i) KB: no catalytically active centers, (ii) Ni(Fe)(OH)$_2$: low number of active sites due to lower BET and a low electrical conductivity, (iii) Ni(Fe)-MOF-74: large domain size and low electrical conductivity, and (iv) Ni(Fe)(OH)$_2$/KB: low number of active sites and accessibility to the active centers. The addition of KB in the solvothermal process prevented the formation of large MOF particles, which allowed an easy access of electrolyte ions to open metal sites, and consequently facilitated the electron transfer as well as the mass transport of O_2.

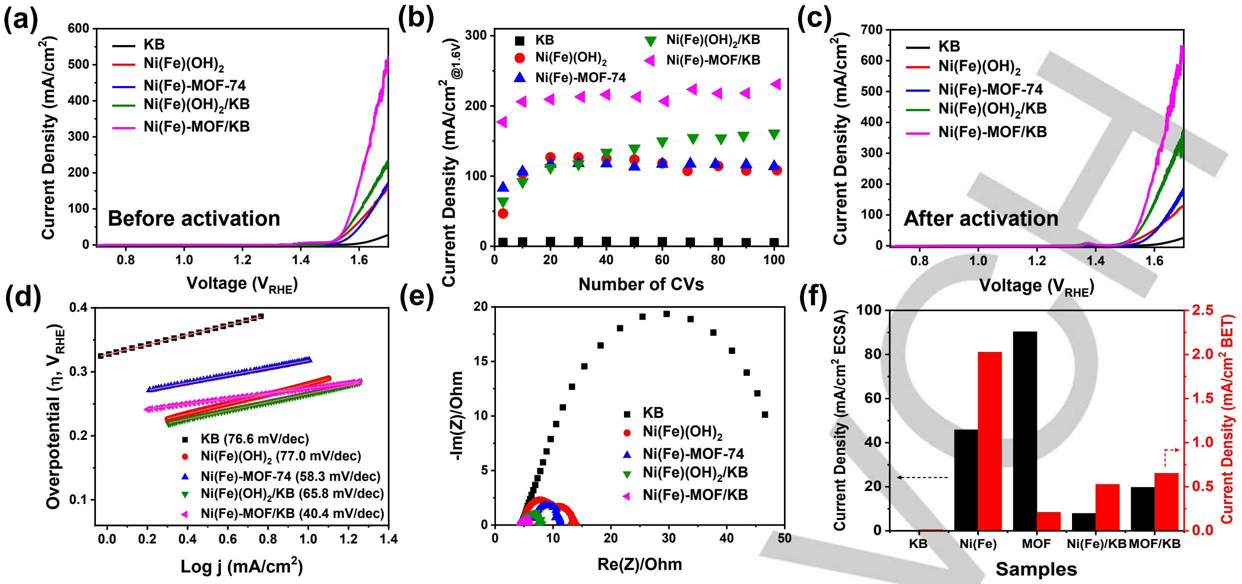

Figure 3. (a) LSV curves of KB, Ni(Fe)(OH)$_2$, Ni(Fe)-MOF-74, Ni(Fe)(OH)$_2$/KB, and Ni(Fe)-MOF/KB before 100 CVs. (b) Current density at 1.6 V_{RHE} recorded with the number of CVs. (c) LSV curves of samples after 100 CVs. (d) Tafel plots, and (e) Impedance curves of KB, Ni(Fe)(OH)$_2$, Ni(Fe)-MOF-74, Ni(Fe)(OH)$_2$/KB, and Ni(Fe)-MOF/KB. (f) Comparison of current density at 1.7 V_{RHE} derived from the current divided by the electrochemical surface area (left, black) and the N_2–sorption BET surface area (right, red) for all the tested samples.

Stability of the electrocatalyst is one of the key parameter and the durability of the most active sample, Ni(Fe)-MOF/KB, was further tested by a multistep chronopotentiometry fixed at different current densities (Figure 4a) and a chronopotentiometry fixed at 10 mA/cm^2 for 12 h (Figure 4b). In the former, when the current density was initially fixed at 20 mA/cm^2 and then was changed to 10, 20, 5, and 20 mA/cm^2 step by step, the applied voltage remained flat in each step. On the other hand, as the current density was changed from 20 to 0 mA/cm^2, the applied voltage was gradually declined over the time, which could be attributed to the alteration of the surface of the catalyst (i.e., the sequential conversion of $Ni^{4+} \rightarrow Ni^{3+} \rightarrow Ni^{2+}$). The applied voltage at –5 mA/cm^2 was slowly increased right after its sudden fall, which was possibly endorsed to active OER species which were rapidly switched to HER ones under cathodic bias.[65] Nevertheless, the applied voltage at 20 mA/cm^2 was recovered to its initial value and remained flat with time, which supports that the oxidation state of active Ni(Fe)-based species was reversibly convertible depending on the applied bias and did not damage the catalytic performance. The long-term stability of Ni(Fe)-MOF/KB fixed at 10 mA cm^{-2} in 1 mol/L KOH was confirmed for 2- and 3-electrode systems as shown in Figure 4b. The activation was observed in the initial period, and the voltage was relatively well-maintained for 12 h, which indicates very good stability of the composite material.

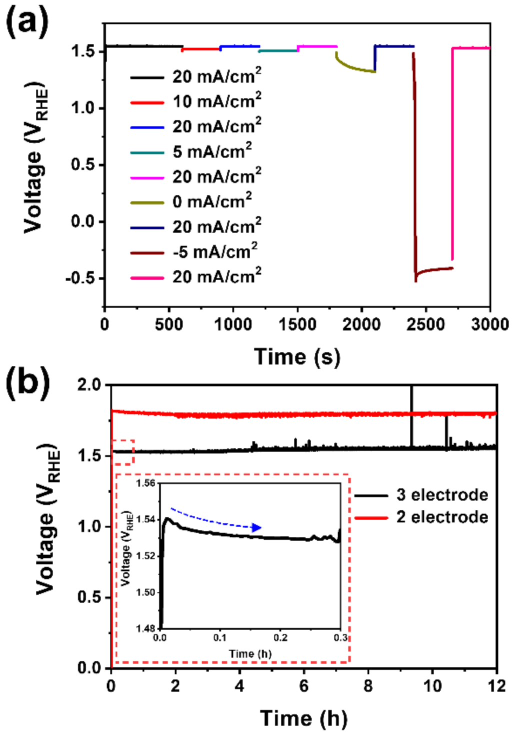

Figure 4. (a) Multistep chronopotentiometry curve and (b) chronopotentiometry curves of 2- and 3-electrode system (Ni(Fe)-MOF/KB on the GCE as working electrode: a Pt wire counter electrode, and a hydrogen reference electrode) recorded at 10 mA/cm^2. The inset in (b) is the enlargement of the curve collected in the initial period under applying bias from 3-electrode system.

Conclusion

The Ni(Fe)-MOF/KB composite could be easily prepared without special treatment via a one-step solvothermal method as a benchmark OER electrocatalyst. The iron elements were homogeneously distributed over the Ni-MOF-74, and the introduction of the highly conductive and porous carbon material ketjenblack (KB) provided the solution to overcome the intrinsic drawbacks of MOF for electrocatalysis, in particular (i) a low electrical conductivity, (ii) a predominant microporosity disturbing a permeability of electrolyte ions into pores and a mass transfer of evolved gases from inner pores to bulk electrolyte, and (iii) a poor wettability. The large-pore structure of Ni(Fe)-MOF-74 allows for good transport of reaction intermediates during the OER. Consequently, the Ni(Fe)-MOF/KB showed a very high OER activity, where the current density at 1.7 V_{RHE} and the overpotential to reach 10 mA/cm^2 were measured as 650 mA/cm^2 and 0.274 V_{RHE}, respectively, after the activation induced by iron species. The Tafel analysis and EIS result support that the introduction of KB was a very effective strategy to overcome the kinetic barrier towards an efficient 4-electron transfer process ($2H_2O \rightarrow O_2 + 4H^+ + 4e^-$). The combination of physicochemical properties MOF and ketjenblack within a composite material is very attractive for catalytic applications and the proposed protocol will serve to optimize the electrocatalytic performance of MOF-based materials not only OER but also for other electrochemical applications.

Experimental Section

Materials and Methods. The chemicals used were obtained from commercial sources and no further purification has been carried out. Ketjenblack EC 600 JD was purchased by AkzoNobel Netherlands.

Powder X-ray diffraction patterns (PXRD) measurements were performed at ambient temperature on a Bruker D2 Phaser powder diffractometer with a rotating silicon, low background sample holder, at 30 kV, 10mA for Cu Kα radiation (λ = 1.5418 Å). The diffractograms were evaluated with Match 3.11 software.

Fourier transform infrared spectra were recorded in attenuated total reflection mode (Platinum ATR-QL, Diamond) on a Bruker TENSOR 37 IR spectrometer in the range of 4000-550 cm^{-1}.

N_2-sorption measurements were performed with Quantachrome Autosorb iQ MP gas sorption analyzer at 77K. Prior to the measurement the materials were degassed under vacuum (10^{-3} mbar) at 150 °C for 24 hours. Brunauer-Emmett-Teller (BET) surface areas were determined from nitrogen adsorption isotherms applying Roquerol plot for microporous type I isotherms ($R^2 > 0.998$).We designate BET surface areas as 'apparent' for microporous materials in line with a suggestion in ref.57, where it is noted that 'the BET-area derived from a Type I isotherm must not be treated as a realistic probe accessible surface area' but 'represents an apparent surface area, which may be regarded as a useful adsorbent "fingerprint" '. Non-local density functional theory (NLDFT) calculations for the pore size distribution were performed using the `$N_2$ at 77 K on carbon, slit/cylindrical pore, NLDFT equilibrium` kernel for KB and $Ni(Fe)(OH)_2$/KB and the `$N_2$ at 77 K on carbon, cylindrical pore, NLDFT equilibrium` kernel for Ni(Fe)-MOF-74, Ni(Fe)-MOF/KB and $Ni(Fe)(OH)_2$.

Flame atomic absorption spectroscopy (AAS) was conducted with a Vario 6 from Analytic Jena. Weighted samples were stirred with concentrated HCl overnight. The solution was carefully filtered and diluted with millipore water to a volume of 25 mL for the AAS measurement.

Scanning electron microscopy (SEM) images were collected with a Jeol JSM-65 10 LV QSEM advanced electron microscope with a LaB6 cathode at 20 kV and a Bruker Xflash 410 silicon drift detector for energy-dispersive X-ray spectrometric (EDX) elemental composition analysis. The small amount of Cu, Al and Au is found in EDX spectra is due to the sample holder and the sputtering of the sample with gold prior to the investigation.

X-ray photoelectron spectroscopy (XPS) measurements were made on an ULVAC-PHI VersaProbe II microfocus X-ray photoelectron spectrometer equipped with a polychromatic aluminum Kα X-ray source (1486.8 eV). Binding energies were referenced to the carbon 1s orbital with a binding energy of 284.8 eV. Experimental XP spectra were fitted by the CasaXPS, version 2.3.19PR1.0, copyright 1999−2018 Casa Software Ltd. program.

Transmission electron microscope (TEM), high resolution transmission electron microscope (HR-TEM), as well as scanning transmission electron microscope (STEM) micrographs were recorded by using a JEM 2200-FS (JEOL) microscope operated at an acceleration voltage of 200 kV. Additional HR-TEM pictures were taken with a HF-2000 microscope (Hitachi). A carbon film supported by a standard copper grid was used as sample carrier for TEM characterization.

Synthesis of Ni(Fe)-MOF-74. Ni(Fe)-MOF-74 was synthesized according to the literature with slight modifications.[45] $Ni(NO_3)_2{\cdot}6H_2O$ (641 mg, 2.20 mmol), $Fe(OAc)_2$ (12 mg, 0.069 mmol) and 2,5-dihydroxyterephthalic acid (148 mg, 0.75 mmol) were mixed in 50 mL DMF, 3 mL EtOH and 3 mL H_2O and stirred overnight at room temperature to obtain a homogeneous solution. This mixture was transferred into an autoclave and heated to 120 °C for 24 h. Following, the sample was washed 3 times with DMF (40 mL, each) for 2 days and 5 times with MeOH (40 mL, each) for 4 days and dried at 120 °C in a vacuum oven for 24 hours. Yield: 300 mg (as-synthesized sample).

Synthesis of Ni(Fe)-MOF/KB Composite. The composite has been synthesized by the same procedure only with the addition of ketjenblack with the same weight ratio (148 mg) as the linker 2,5-dihydroxyterephthalic acid into the mixture. After overnight stirring, the mixture was transferred into the autoclave and heated to 120 °C for 24 h. Consequently, the sample was washed 3 times with DMF (40 mL, each) for 2 days and 5 times with MeOH (40 mL, each) for 4 days and dried at 120 °C in a vacuum oven for 24 hours. Yield: 507 mg.

Mass fractions of the components for Ni(Fe)-MOF/KB: 76.8 wt% Ni(Fe)-MOF-74 and 23.2 wt% KB.

Synthesis of $Ni(Fe)(OH)_2$ and $Ni(Fe)(OH)_2$/KB. $Ni(Fe)(OH)_2$ was synthesized by simply mixing $Ni(NO_3)_2{\cdot}6H_2O$ (641 mg, 2.20 mmol) and $Fe(OAc)_2$ (12 mg, 0.069 mmol) in 50 mL DMF, 3 mL EtOH and 3 mL H_2O overnight and subsequently transferring into an autoclave for heating 24 h at 120 °C. $Ni(Fe)(OH)_2$/KB was synthesized in same way only with the addition of KB (148 mg) into the mixture. Both materials were washed 3 times with DMF (40 mL, each) for 2 days and 5 times with MeOH (40 mL, each) for 4 days and dried at 120 °C in a vacuum oven for 24 h.

Yield: 137 mg for $Ni(Fe)(OH)_2$ and 310 mg for $Ni(Fe)(OH)_2$/KB.

Mass fractions of the components for $Ni(Fe)(OH)_2$/KB: 47 wt% Ni(Fe)-MOF-74 and 53 wt% KB.

Electrocatalytic activity measurement. The electrocatalytic OER test was conducted in 1 M KOH under continuous argon purging and the temperature was kept at 298 K by cooling water. The three-electrode configuration constituting a Pt wire (a counter electrode), a hydrogen reference electrode (HydroFlex, Gaskatel), and a glassy carbon electrode

(GCE) (a working electrode) was used, where the electrochemical signal was recorded by the potentiostat (Biologic SP-150). Before loading the catalysts, the GCE was polished with Al_2O_3 suspensions (5 and 0.25 μm, Allied High Tech Products, Inc.) and cleaned by sonication in distilled water. The sample (4.8 mg) was added in the solution containing 0.75 ml H_2O, 0.25 ml 2-propanol, and 50 μl Nafion solution (Aldrich, ~5% in a mixture of lower aliphatic alcohols and water), and was sonicated for 30 min to obtain a homogenous ink solution. Finally, 5.25 μl of the ink solution was dropped onto the GCE (5 mm in diameter, 0.196 cm^2), which was dried under argon atmosphere. The linear sweep voltammetry (LSV) and cyclic voltammetry (CV) were collected by scanning the potential from 0.7 to 1.7 V_{RHE} with 10 mV/s and from 0.7 to 1.6 V_{NHE} with 50 mV/s under rotating the electrode at 2,000 rpm, respectively. The impedance spectra were collected at 1.6 V_{RHE} from 10^5 to 0.5 Hz. The electrochemical active surface area (ECSA) was calculated by the equation: ECSA = C_{dl}/Cs, where C_{dl} is the double layer capacitance and C_s is the specific capacitance (0.04 mF/cm^2 for 1 M KOH electrolyte). The C_{dl} was estimated by plotting the non-Faradaic capacitive current ($j_{anode} - j_{cathode}$) from 1 to 1.1 V_{RHE} versus the scan rate (50 – 250 mV/s), whose linear slope was divided in half. In order to check the long-term stability of catalysts, the chronopotentiometry fixed at 10 mA/cm^2 was measured in 2- and 3-electrode system for 12 h.

Supporting Information (see footnote on the first page of this article):

Material sources, information on MIL-101, IR spectra, SEM images, NMR spectra, further details on gas and water vapor sorption.

Acknowledgements

H.T. thanks the Max Planck Society for the basic funding. This work was financially supported Max Planck Society and the Deutsche Forschungsgemeinschaft (DFG, German Research Foundation) grant 388390466–TRR 247 within the Collaborative Research Centre/Transregio 247 “Heterogeneous Oxidation Catalysis in the Liquid Phase”. We also sincerely thank E. Budiyanto for further HR-TEM measurements. C.J. is indebted to the DFG for funding within the priority program SPP 1928 “COORNET” (grant Ja466–43/1).

Keywords: metal organic framework • electrocatalysis • oxygen evolution reaction • ketjenblack • catalyst activation

References (see the next but one page)

Entry for the Table of Contents (Please choose one layout)

Layout 1:

FULL PAPER

Ni(Fe)-MOF/KB simply prepared via a one-step solvothermal method showed outstanding OER performance, displaying an overpotential of 0.274 V at 10 mA/cm^2 and a current density of around 650 mA/cm^2 at 1.7 V$_{RHE}$.

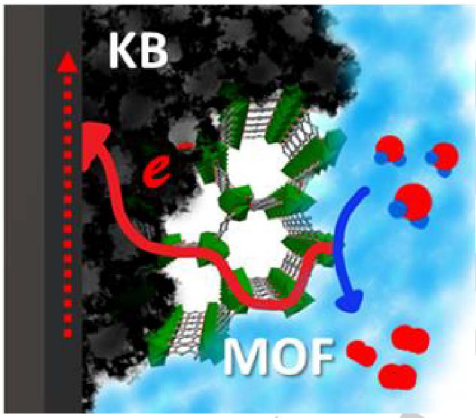

Seçil Öztürk, Gun-hee Moon, Alex Spieß, Stefan Roitsch, Harun Tüysüz and Christoph Janiak**

Page No. – Page No.

Highly-Efficient Oxygen Evolution Electrocatalyst Derived from Metal-Organic Framework and Ketjenblack Carbon Material

Layout 2:

FULL PAPER

Seçil Öztürk, Gun-hee Moon, Alex Spieß, Stefan Roitsch, Harun Tüysüz and Christoph Janiak**

Page No. – Page No.

Highly-Efficient Oxygen Evolution Electrocatalyst Derived from Metal-Organic Framework and Ketjenblack Carbon Material

Additional Author information for the electronic version of the article.

Author: Seçil Öztürk ORCID identifier 0000-0001-6236-4385

Author: Harun Tüysüz ORCID identifier 0000-0001-8552-7028

Author: Christoph Janiak ORCID identifier 0000-0002-6288-9605

---

[1] S. Chu, Y. Cui, N. Liu, *Nat. Mater.* **2017**, 16, 16–22.

[2] Z. W. Seh, J. Kibsgaard, C. F. Dickens, I. Chorkendorff, J. K. Nørskov, T. F. Jaramillo, *Science* **2017**, *355*, eaad4998.

[3] X. X. Zou, Y. Zhang, *Chem. Soc. Rev.* **2015**, *44*, 5148–5180.

[4] N. T. Suen, S. F. Hung, Q. Quan, N. Zhang, Y. J. Xu, H. M. Chen, *Chem. Soc. Rev.* **2017**, *46*, 337–365.

[5] C. C. L. McCrory, S. Jung, J. C. Peters, T. F. Jaramillo, *J. Am. Chem. Soc.* **2013**, *135*, 16977–16987.

[6] Y. Lee, J. Suntivich, K. J. May, E. E. Perry, Y. Shao-Horn, *J. Phys. Chem. Lett.* **2012**, *3*, 399–404.

[7] T. Reier, M. Oezaslan, P. Strasser, *ACS Catal.* **2012**, *2*, 1765–1772.

[8] A. Mendoza-Garcia, H. Zhu, Y. Yu, Q. Li, L. Zhou, D. Su, M. J. Kramer, S. Sun, *Angew. Chem. Int. Ed.* **2015**, *54*, 9642–9645.

[9] D. Li, H. Baydoun, C. N. Verani, S. L. Brock, *J. Am. Chem. Soc.* **2016**, *138*, 4006–4009.

[10] X. Deng, H. Tüysüz, *ACS Catal.* **2014**, *4*, 3701–3714.

[11] X. Deng, S. Öztürk, C. Weidenthaler, H. Tüysüz, *ACS Appl. Mater. Interfaces* **2017**, *9*, 21225–21233.

[12] F. Song, X. Hu, *J. Am. Chem. Soc.* **2014**, *136*, 16481–16484.

[13] J. Zhang, T. Wang, D. Pohl, B. Rellinghaus, R. Dong, S. Liu, X. Zhuang, X. Feng, *Angew. Chem. Int. Ed.* **2016**, *55*, 6702–6707.

[14] S. Anantharaj, S. R. Ede, K. Sakthikumar, K. Karthick, S. Mishra, S. Kundu, *ACS Catal.* **2016**, *6*, 8069–8097.

[15] L. A. Stern, L. Feng, F. Song, X. Hu, *Energy Environ. Sci.* **2015**, *8*, 2347–2351.

[16] S. Fu, C. Zhu, J. Song, M. H. Engelhard, X. Li, D. Du, Y. Lin, *ACS Energy Lett.* **2016**, *1*, 792–796.

[17] M. D. Kärkäs, B. Åkermark, *Dalton Trans.* **2016**, *45*, 14421–14461.

[18] Y. Surendranath, M. W. Kanan, D. G. Nocera, *J. Am. Chem. Soc.* **2010**, *132*, 16501–16509.

[19] A. Moysiadou, S. Lee, C. S. Hsu, H. M. Chen, X. Hu, *J. Am. Chem. Soc.* **2020**, *142*, 11901–11914.

[20] S. H. Yan, K. P. Abhilash, L. Y. Tang, M. Yang, Y. F. Ma, Q. Y. Xia, Q. B. Guo, H. Xia, *Small* **2019**, *15*, 1804371.

[21] S. Anantharaj, S. Noda, *Small* **2020**, *16*, 1905779.

[22] L. Trotochaud, S. L. Young, J. K. Ranney, S. W. Boettcher, *J. Am. Chem. Soc.* **2014**, *136*, 6744–6753.

[23] M. S. Burke, M. G. Kast, L. Trotochaud, A. M. Smith, S. W. Boettcher, *J. Am. Chem. Soc.* **2015**, *137*, 3638–3648.

[24] Y. Qian, I. A. Khan, D. Zhao, *Small* **2017**, *13*, 1701143.

[25] D. Zhu, M. Qiao, J. Liu, T. Tao, C. Guo, *J. Mater. Chem. A* **2020**, *8*, 8143–8170.

[26] S. Mukhopadhyay, O. Basu, R. Nasani, S. K. Das, *Chem. Commun.* **2020**, *56*, 11735–11748.

[27] P. Shao, L. Yi, S. Chen, T. Zhou, J Zhang, *J. Energy Chem.* **2020**, *40*, 156–170.

[28] J. Duan, Y. Sun, S. Chen, X. Chen, C. Zhao, *J. Mater. Chem. A* **2020**, *8*, 18810–18815.

[29] P. I. Scheurle, A. Mähringer, A. C. Jakowetz, P. Hosseini, A. F. Richter, G. Wittstock, D. D. Medina, T. A. Bein, *Nanoscale* **2019**, *11*, 20949–20955.

[30] M. D. Allendorf, A. Schwartzberg, V. Stavila, A. A. Talin, *Chem. Eur. J.* **2011**, *17*, 11372–11388.

[31] A. Mahmood, W. Guo, H. Tabassum, R. Zou, *Adv. Energy Mater.* **2016**, *6*, 1600423.

[32] Y. Lin, Z. Tian, L. Zhang, J. Ma, Z. Jiang, B. J. Deibert, R. Ge, L. Chen, *Nat. Commun.* **2019**, *10*, 162.

[33] S. M. Cao, H. B. Chen, B. X. Dong, Q. H. Zheng, Y. X. Ding, M. J. Liu, S. L. Qian, Y. L. Teng, Z. W. Li, W. L. Liu, *J. Energy Chem.* **2021**, *54*, 555–563.

[34] C. Petit, T. J. Bandosz, *Adv. Mater.* **2009**, *21*, 4753–4757.

[35] Y. Fang, X. Li, F. Li, X. Lin, M. Tian, X. Long, X. An, Y. Fu, J. Jin, J. Ma, *J. Power Sources* **2016**, *326*, 50–59.

[36] J. Li, N. Zhou, J. Song, L. Fu, J. Yan, Y. Tang, H. Wang, *ACS Sust. Chem. Eng.* **2018**, *6*, 413–421.

[37] C. Wang, M. Zhou, Y. Ma, H. Tan, Y. Wang, Y. Li, *Chem. Asian J.* **2018**, *13*, 2054–2059.

[38] H. Peng, X. Yang, Y. Ma, J. Liu, Y. Wang, H. Tan, Y. Li, *CrystEngComm* **2018**, *20*, 5387–5394.

[39] Z. H. Huang, N. H. Xie, M. Zhang, B. Q. Xu, *ChemSusChem* **2019**, *12*, 200–207.

[40] K. Tan, S. Zuluaga, Q. Gong, P. Canepa, H. Wang, J. Li, Y. J. Chabal, T. Thonhauser, *Chem. Mater.* **2014**, *26*, 6886–6895.

[41] M. Yu, G. Moon, E. Bill, H. Tüysüz, *ACS Appl. Energy Mater.* **2019**, *2*, 1199–1209.

[42] J. Xing, K. Guo, Z. Zou, M. Cai, J. Du, C. Xu, *Chem. Commun.* **2018**, *54*, 7046–7049.

[43] F. Z. Sun, G. Wang, Y. Q. Ding, C. Wang, B. B. Yuan, Y. Q. Lin, *Adv. Energy Mater.* **2018**, *8*, 1800584.

[44] F. Zheng, D. Xiang, P. Li, Z. Zhang, C. Du, Z. Zhuang, X. Li, W. Chen, *ACS Sust. Chem. Eng.* **2019**, *7*, 9743–9749.

[45] L. J. Wang, H. Deng, H. Furukawa, F. Gandara, K. E. Cordova, D. Peri, O. M. Yaghi, *Inorg. Chem.* **2014**, *53*, 5881–5883.

[46] Z. Gao, Z. W. Yu, F. Q. Liu, Y. Yu, X. M. Su, L. Wang, Z. Z. Xu, Y. L. Yang, G. R. Wu, X. F. Feng, F. Luo, *Inorg. Chem.* **2019**, *58*, 11500–11507.

[47] W. Wong-Ng, J. Kaduk, H. Wu, M. Suchomel, *Powder Diffraction* **2012**, *27*, 256–262.

[48] R. S. Forgan, *Chem. Sci.* **2020**, *11*, 4546–4562.

[49] M. Aghazadeh, M. Ghaemi, B. Sabour, S. Dalvand, *J. Solid State Electrochem* **2014**, *18*, 1569–1584.

[50] Y. Kang, Y. Yang, L. C. Yin, X. Kang, G. Liu, H. M. Cheng, *Adv. Mater.* **2015**, *27*, 4572–4577.

[51] N. E. El-Gamel, *Eur. J. Inorg. Chem.* **2015**, *8*, 1351–1358.

[52] B. Li, H. C. Zeng, *Chem. Mater.* **2019**, *31*, 5320–5330.

[53] H. Sun, D. Liu, J. Du, *Chem. Sci.* **2019**, *10*, 657–664.

[54] J. H. Deng, J. Luo, Y. L. Mao, S. Lai, Y. N. Gong, D. C. Zhong, T. B. Lu, *Sci. Adv.* **2020**, *6*, eaax9976.

[55] D. S. Hall, D. J. Lockwood, C. Bock, B. R. MacDougall, *Proc. R. Soc. A.* **2015**, *471*, 20140792.

[56] X. Wang, H. Xiao, A. Li, Z. Li, S. Liu, Q. Zhang, Y. Gong, L. Zheng, Y. Zhu, C. Chen, D. Wang, Q. Peng, L. Gu, X. Han, J. Li, Y. Li, *J. Am. Chem Soc.* **2018**, *140*, 15336–15341.

[57] M. Thommes, K. Kaneko, A. V. Neimark, J. P. Olivier, F. Rodriguez-Reinoso, J. Rouquerol, K. S. Sing, *Pure Appl. Chem.* **2015**, *87*, 1051–1069, DOI: 10.1515/pac-2014-1117.

[58] H. B. Li, M. H. Yu, F. X. Wang, P. Liu, Y. Liang, J. Xiao, C. X. Wang, Y. X. Tong, G. W. Yang, *Nat. Commun.* **2013**, *4*, 1894.

[59] D. A. Corrigan, *J. Electrochem. Soc.* **1987**, *134*, 377–384.

[60] G.-h. Moon, M. Yu, C. K. Chan, H. Tüysüz, *Angew. Chem. Int. Ed.* **2019**, *58*, 3491–3495.

[61] S. Möller, S. Barwe, J. Masa, D. Wintrich, S. Seisel, H. Baltruschat, W. Schuhmann, *Angew. Chem. Int. Ed.* **2020**, *59*, 1585–1589.

[62] G.-h. Moon, W. Kim, A. D. Bokare, N. Sung, W. Choi, *Energy Environ. Sci.* **2014**, *7*, 4023–4028.

[63] G.-h. Moon, A. Bähr, H. Tüysüz, *Chem. Mater.* **2018**, *30*, 3779–3788.

[64] P. Chen, K. Xu, T. Zhou, Y. Tong, J. Wu, H. Cheng, X. Lu, H. Ding, C. Wu, Y. Xie, *Angew. Chem. Int. Ed.* **2016**, *55*, 2488–2492.

[65] B. H. R. Suryanto, Y. Wang, R. K. Hocking, W. Adamson, C. Zhao, *Nat. Commun.* **2019**, *10*, 5599.

Supporting Information

Highly-Efficient Oxygen Evolution Electrocatalyst Derived from Metal-Organic Framework and Ketjenblack Carbon Material

Seçil Öztürk,[a,†] Gun-hee Moon,[b,d,†] Alex Spieß,[a] Stefan Roitsch,[c] Harun Tüysüz[b,] Christoph Janiak[a,]**

[a] Institut für Anorganische Chemie und Strukturchemie, Heinrich-Heine-Universität Düsseldorf, Universitätsstraße 1, 40225 Düsseldorf, Germany, Fax: +49-211-81-12287; Tel: +49-211-81-12286. E-mail: janiak@uni-duesseldorf.de

[b] Max-Planck-Institut für Kohlenforschung, Heterogeneous Catalysis and Sustainable Energy, Kaiser-Wilhelm-Platz 1, 45470 Mülheim an der Ruhr, Germany, Fax: +49-208-306-2989; Tel: +49-208-306-2371. E-mail: tueysuez@kofo.mpg.de

[c] Department für Chemie, Universität zu Köln, Greinstr. 4-6, D-50939 Köln, Germany, Fax: +49-221-470-5104; Tel: +49-221-470-4546. E-Mail: sroitsch@uni-koeln.de

[d] Extreme Materials Research Center, Korea Institute of Science and Technology (KIST), 02792 Seoul, South Korea

* To whom correspondence should be addressed (H. Tüysüz & C. Janiak)
E-mail: tueysuez@kofo.mpg.de & janiak@uni-duesseldorf.de
[†] These authors contributed equally to this work.

Emails: oeztues@uni-duesseldorf.de, moon@mpi-muelheim.mpg.de, alex.spiess@hhu.de, sroitsch@uni-koeln.de, tueysuez@kofo.mpg.de, janiak@uni-duesseldorf.de

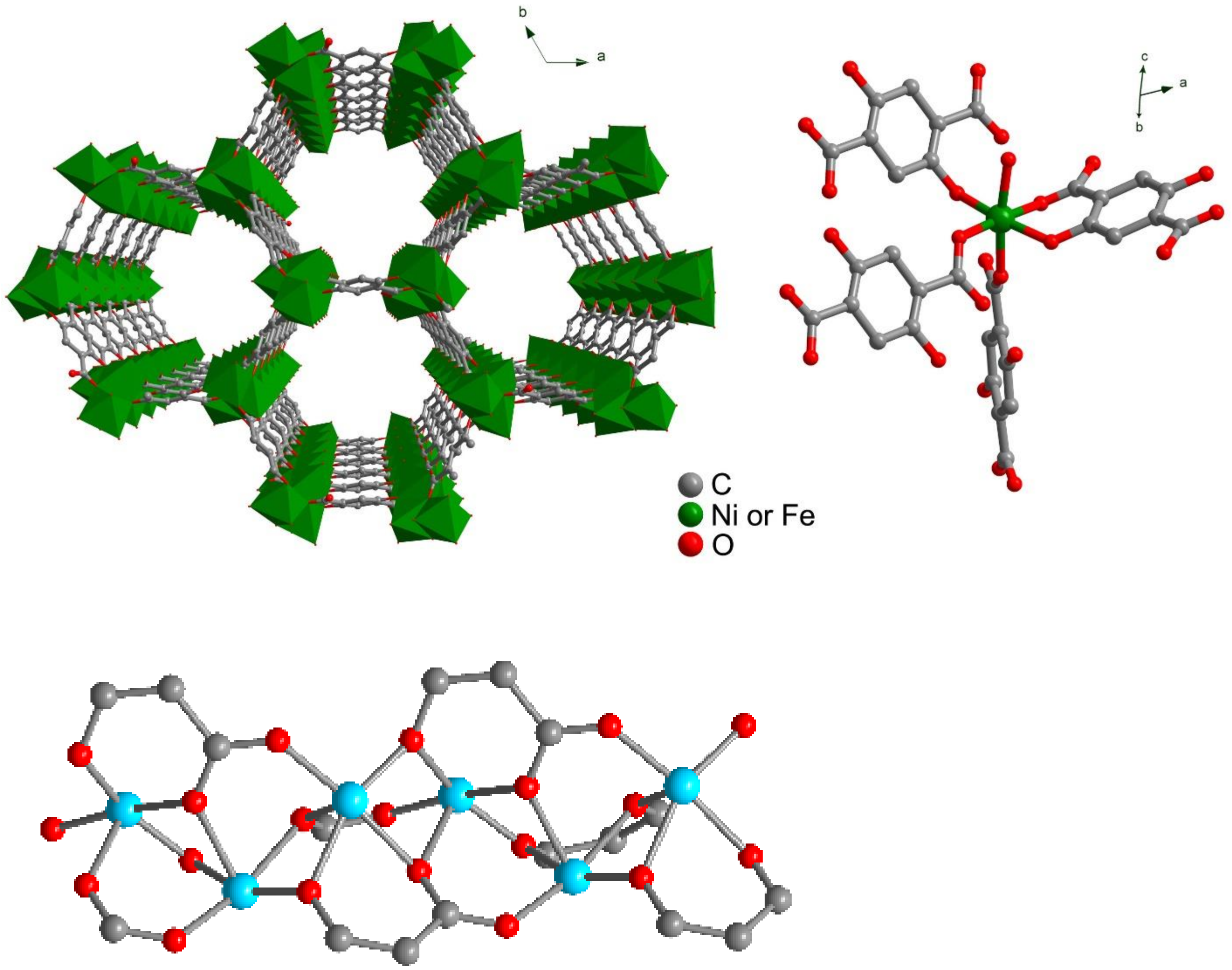

Scheme S1. Crystal structure illustration of dehydrated Ni(Fe)-MOF-74 (top left) and the coordination environment of the Ni^{2+} or Fe^{2+} centers (top right and bottom). Nickel or iron centers are penta-coordinated by the five oxygen atoms from the organic linkers and the sixth coordination site is occupied by a solvent (water or DMF). Crystal structure data taken from ref. [1], CCDC: 1494751; drawings made with the software Diamond.[2]

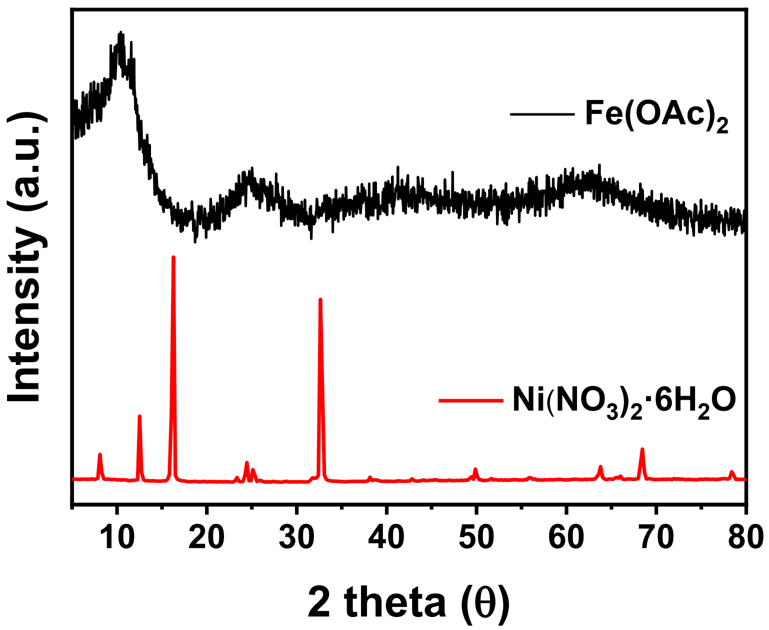

Figure S1. PXRD patterns of $Ni(NO_3)_2{\cdot}6H_2O$ and $Fe(OAc)_2$ precursors.

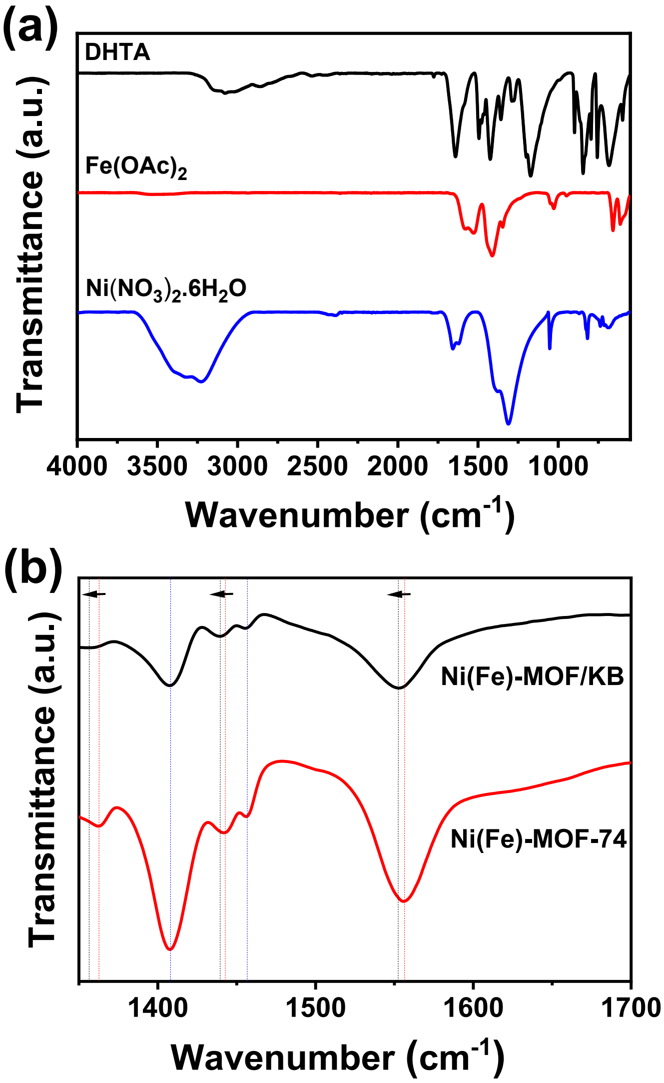

Figure S2. FT-IR spectra of (a) $Ni(NO_3)_2 \cdot 6H_2O$, $Fe(OAc)_2$, and 2,5-dihydroxyterephthalic acid (DHTA) and (b) Ni(Fe)-MOF-74 and Ni(Fe)-MOF/KB. The peak shift by KB was noted by the arrow in (b).

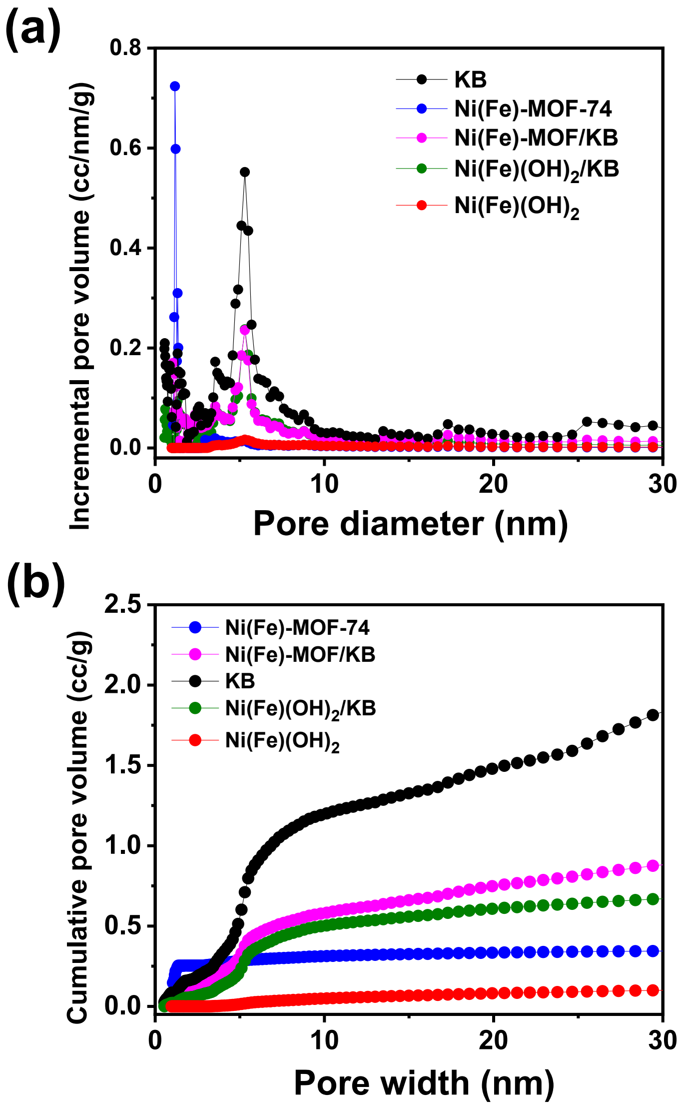

Figure S3. (a) Pore size distribution and (b) Cumulative pore volume of Ni(Fe)-MOF-74, Ni(Fe)-MOF/KB, Ni(Fe)(OH)$_2$, Ni(Fe)(OH)$_2$/KB, and KB.

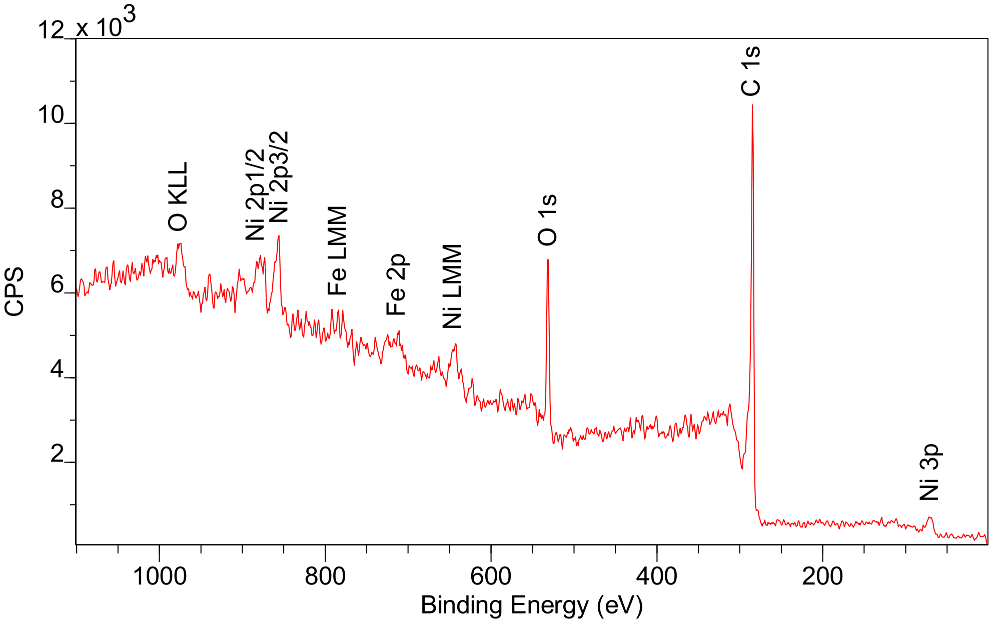

Figure S4. XPS Survey spectrum of Ni(Fe)-MOF/KB.

X-ray photoelectron spectroscopy (XPS) measurements were carried out to further investigate the surface composition and the valence state of the materials (Figure S4-S5). Figure S4 presents the full XPS survey spectrum of Ni(Fe)-MOF/KB, which confirms the presence of Ni, Fe, C and O elements.

The high-resolution Fe 2p XPS spectra show two main peaks at ~710-712 eV and 723-725 eV, which can be ascribed to Fe $2p_{3/2}$ and $2p_{1/2}$, with a satellite peak at 715-717 eV indicating the presence of Fe^{2+} species[3,4] (Figure S5a,c,e,g).

The high-resolution Ni 2p XPS spectra can be deconvoluted into four peaks as displayed in Figure S5b,d,f,h. The spectra show $2p_{3/2}$ and $2p_{1/2}$ single peaks at ~856.2-856.9 eV and ~873.9-874.6 eV, respectively, accompanied by two shake-up satellite peaks at ~861.5 eV and ~880 eV as expected for Ni^{2+}.[5,6] In $Ni(Fe)(OH)_2$ the spin-energy separation of 17.7 eV is characteristic of α-$Ni(OH)_2$ and in good agreement with literature.[6]

The Ni 2p spectrum of Ni(Fe)-MOF/KB (Figure S5d) shows a 0.6 eV and the Fe 2p spectrum shows (Figure S5c) a 1.2 eV shift to higher binding energy compared to the neat MOF, suggesting an interaction between ketjenblack carbon and the MOF.[7,8]

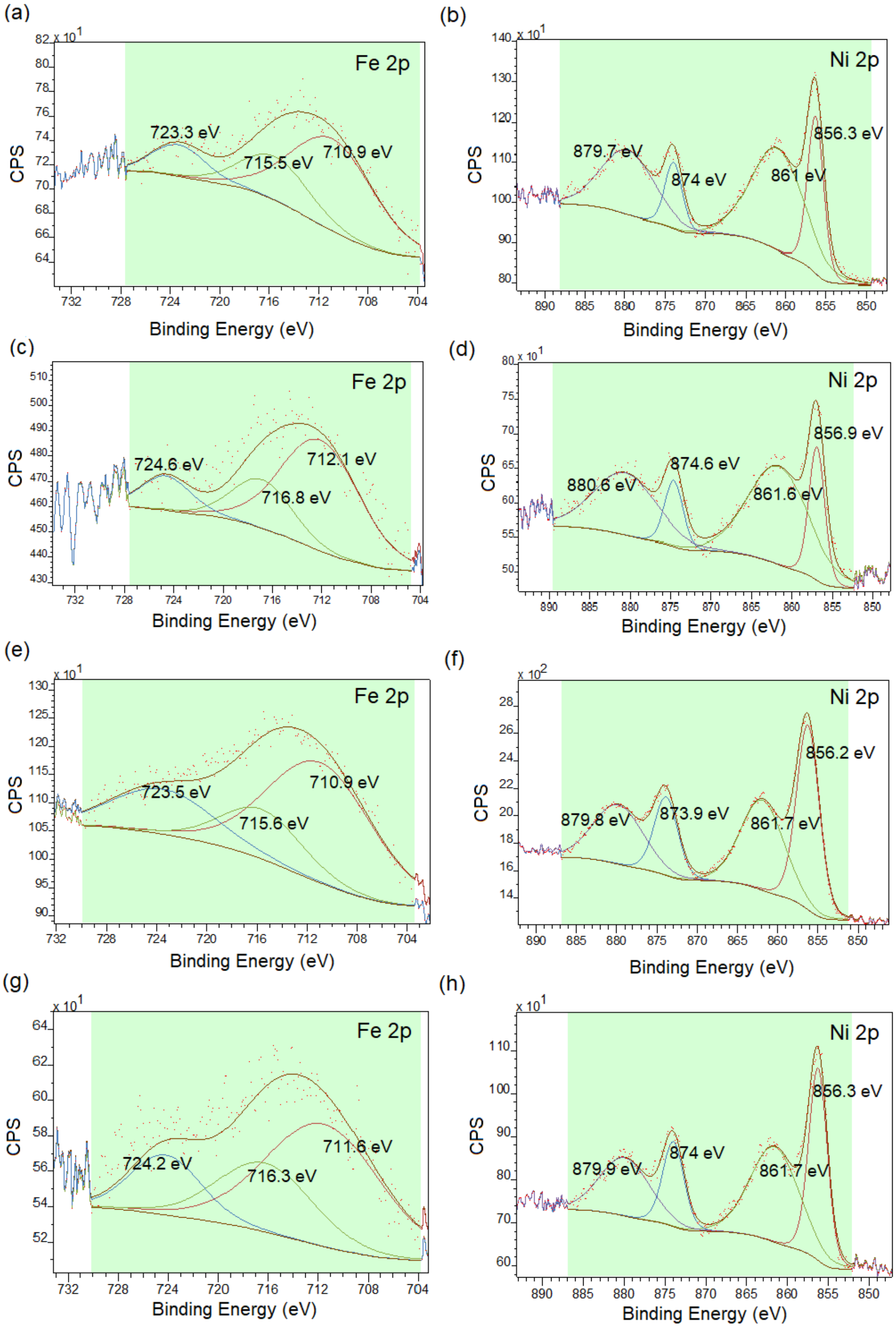

Figure S5. High-resolution Fe 2p and Ni 2p XPS spectra of a-b) Ni(Fe)-MOF-74, c-d) Ni(Fe)-MOF/KB, e-f) Ni(Fe)(OH)$_2$, g-h) Ni(Fe)(OH)$_2$/KB.

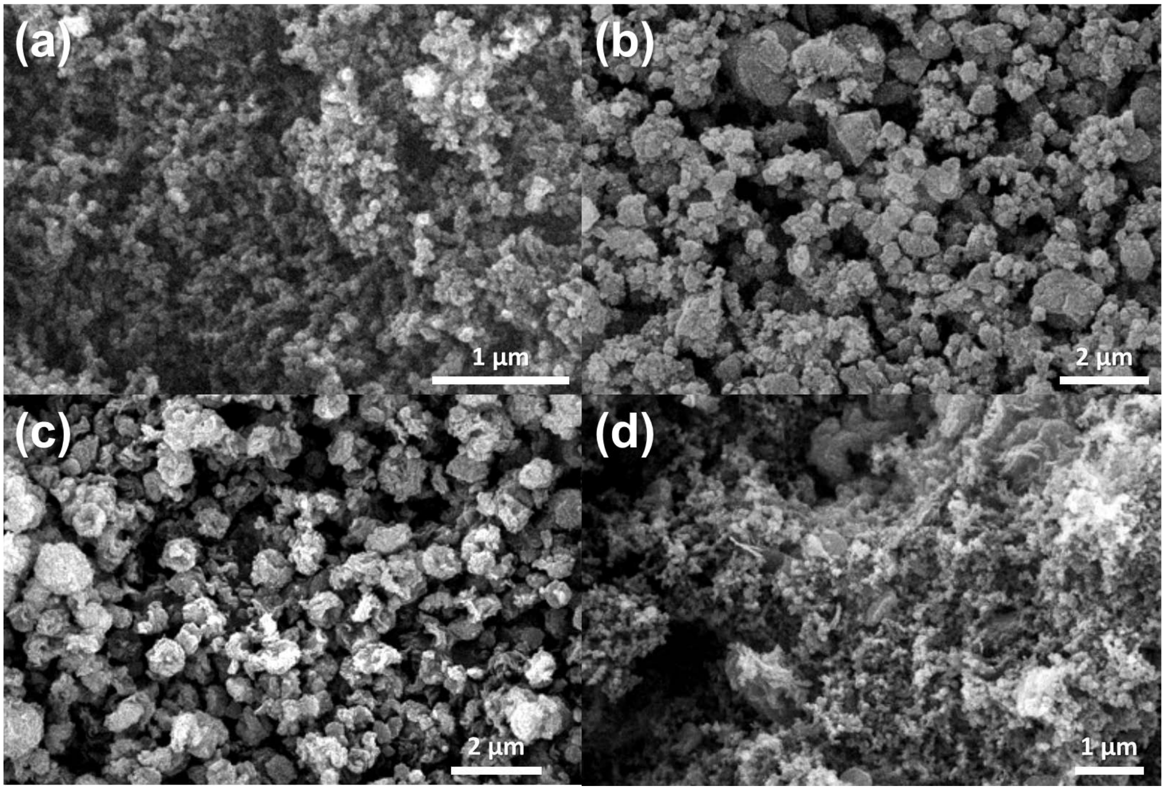

Figure S6. SEM images for (a) KB, (b) Ni(Fe)-MOF-74, (c) $Ni(Fe)(OH)_2$, and (d) $Ni(Fe)(OH)_2$/KB.

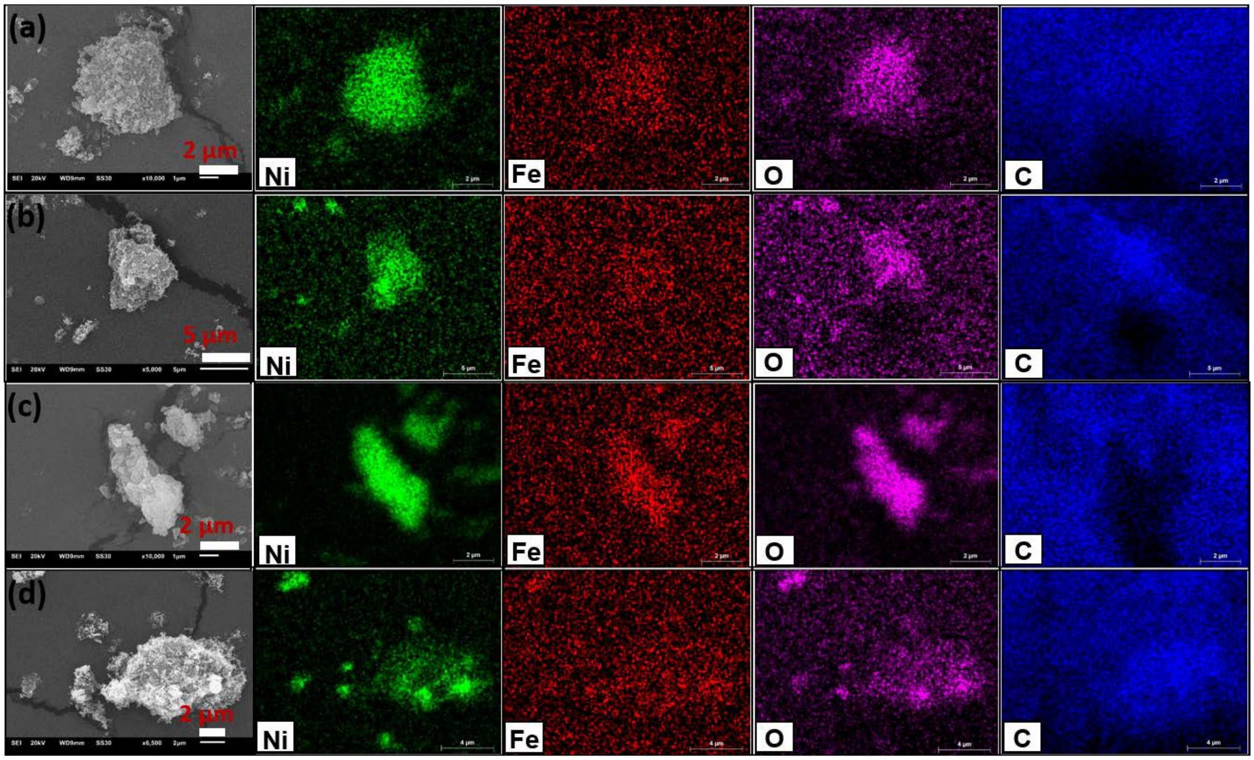

Figure S7. SEM-EDX elemental mapping of a) Ni(Fe)-MOF-74, b) Ni(Fe)-MOF/KB, c) $Ni(Fe)(OH)_2$ and d) $Ni(Fe)(OH)_2$/KB.

Table S1 SEM-EDX and AAS results of all synthesized materials.

Material	SEM-EDX		AAS [a]				theor. for Ni-only material [b]
	Molar ratio		Metal wt%		approx. Molar ratio		Ni (wt.%)
	Fe	Ni	Fe	Ni	Fe	Ni	
Ni(Fe)-MOF-74	1	34	1.08	34.27	1	31	37
Ni(Fe)-MOF/KB	1	31	0.58	16.24	1	27	
Ni(Fe)(OH)$_2$	1	31	1.33	44.81	1	32	63
Ni(Fe)(OH)$_2$/KB	1	27	0.62	24.01	1	37	

[a] Flame atomic absorption spectroscopy. Weighted samples were mixed with concentrated HCl. The solution was filtered carefully and diluted with millipore water to a volume of 25 mL for the AAS. [b] Theoretical Ni wt% calculated assuming solvent-free Ni-MOF-74 as [Ni$_2$(DHTP)] and anhydrous Ni(OH)$_2$.

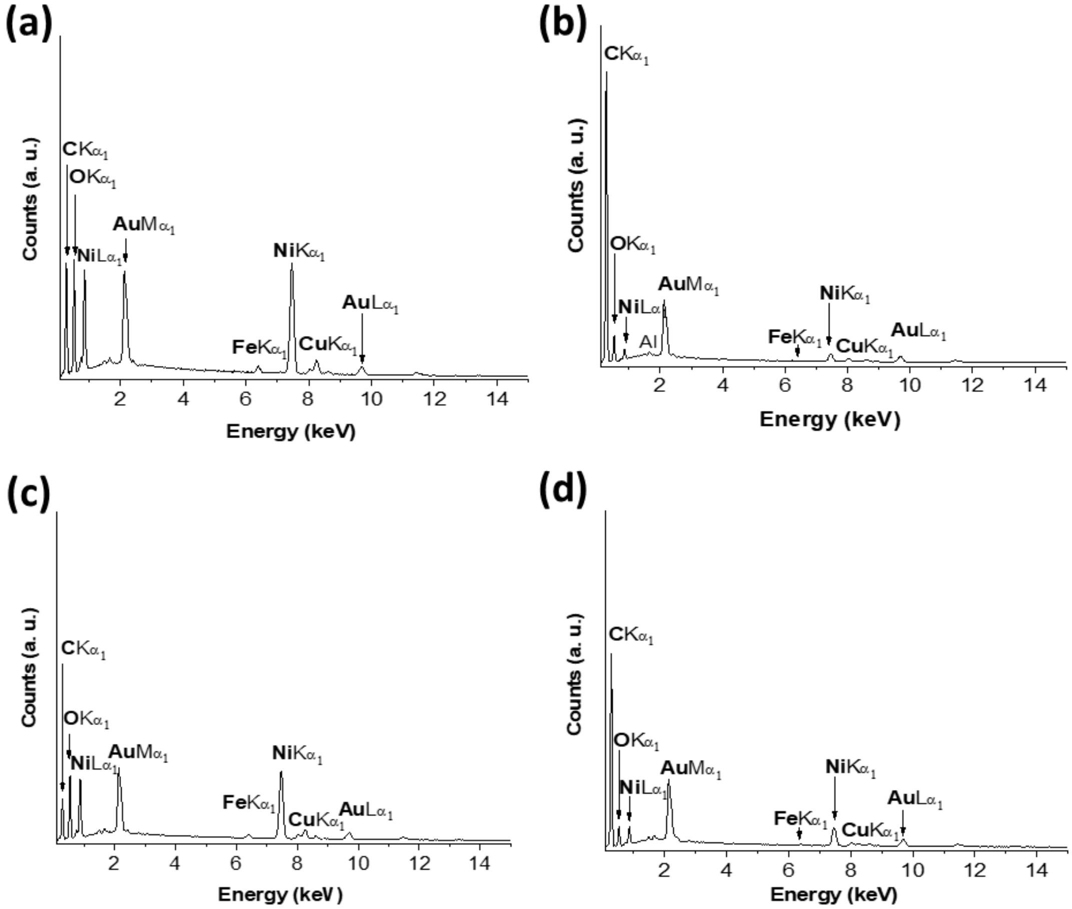

Figure S8. SEM-EDX spectra of a) Ni(Fe)-MOF-74, b) Ni(Fe)-MOF/KB, c) Ni(Fe)(OH)$_2$ and d) Ni(Fe)(OH)$_2$/KB.

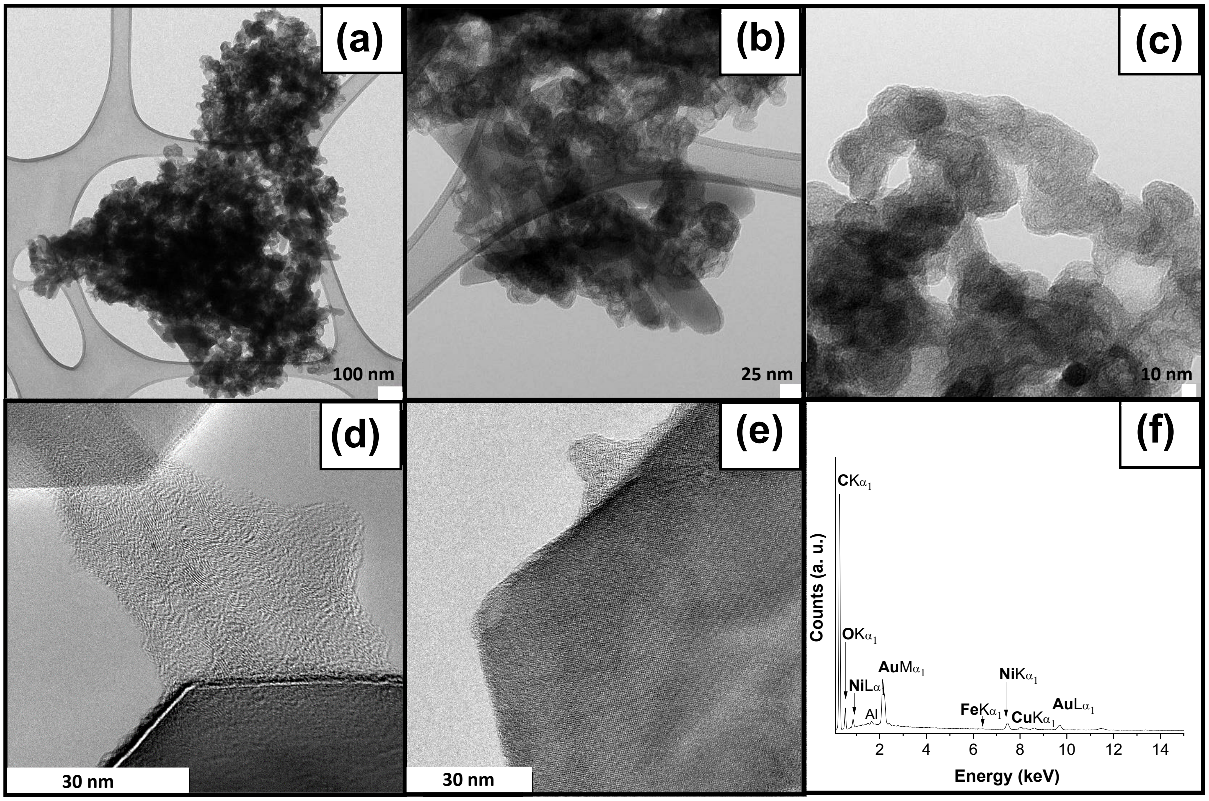

Figure S9. a-c) TEM pictures with different magnifications d, e) HR-TEM pictures f) EDX-spectrum of Ni(Fe)-MOF/KB. TEM micrographs show the crystalline, opaque Ni(Fe)-MOF-74 particles, which are surrounded by the more transparent carbon particles. The carbon is visible with its typical amorphous appearance as a thin layer at the edges of the particles. In Figure S9d, a thin carbon layer glues two MOF particles together. Here one can also observe the turbostratic structure of the carbon which is visible as irregular but has locally ordered lines.

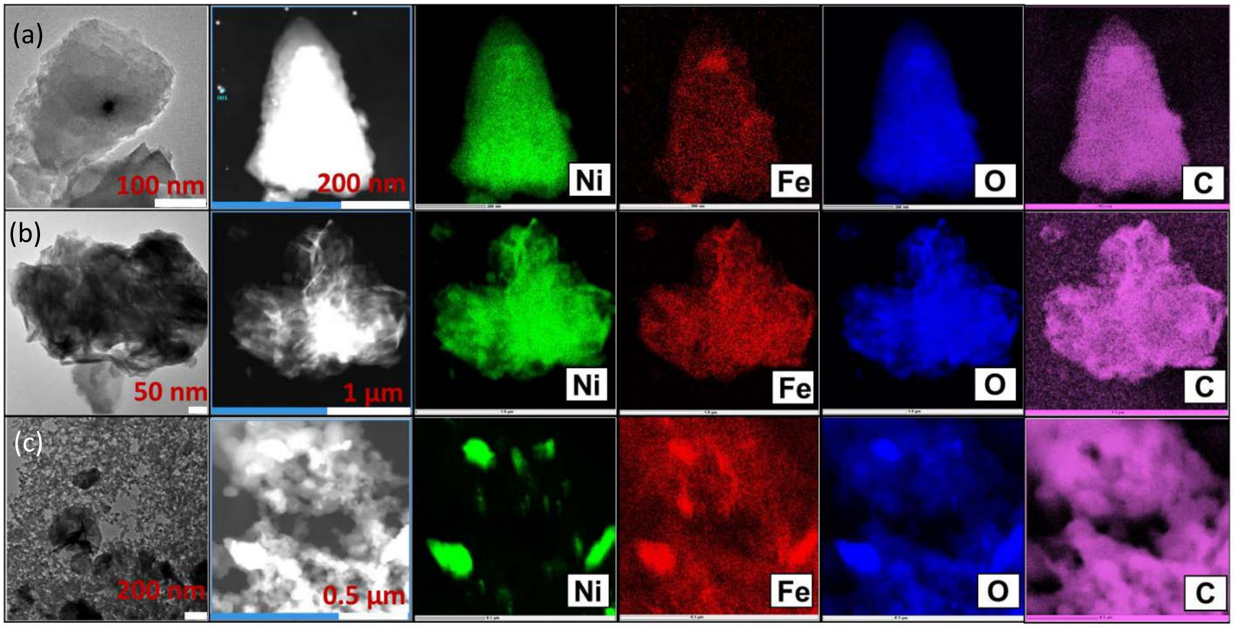

Figure S10. TEM images and STEM elemental mapping of a) Ni(Fe)-MOF-74 b) Ni(Fe)(OH)$_2$ and c) Ni(Fe)(OH)$_2$/KB.

Table S2. Comparison of OER activity of previously reported Fe-Ni-MOF-based and $Ni(OH)_2$ based catalysts.

Catalyst [a]	KOH Electrolyte [mol/L]	Overpotential at 10 mA/cm^2 [mV]	Tafel slope [mV/dec]	Ref.
$Ni(Fe)(OH)_2$/KB	1	265	66	This study
Ni(Fe)-MOF/KB	1	274	40	This study
NiFe-MOF-74 on Ni foam	1	223	72	[4]
Fe/Ni-BTC@NF	1	270	47	[9]
NiFe-UMNs	1	260	30	[10]
Ni-BDC/$Ni(OH)_2$	1	320	41	[11]
Ni-MOF@Fe-MOF	1	265	82	[12]
Fe_1Ni_2-BDC	1	260	35	[13]
α-$Ni(OH)_2$ hollow spheres	0.1	331	45	[14]
MWCNTs/ β-$Ni(OH)_2$	0.1	474	87	[8]
$Fe_{0.22}Ni_{0.78}(OH)_2$ nanosheets	1	320	35	[15]
$Ni(OH)_2$ nanosheets	1	470	60	[15]
α-$Ni(OH)_2$	1	387	53	[16]
α-$Ni(OH)_2$-rGO	1	356	50	[16]

[a] KB: ketjenblack, NF: nickel foam, UMN: ultrathin metal-organic frameworks nanosheets, BDC: 1,4-benzene dicarboxylate, MWCNT: multiwalled carbon nanotubes, rGO: reduced graphene oxide.

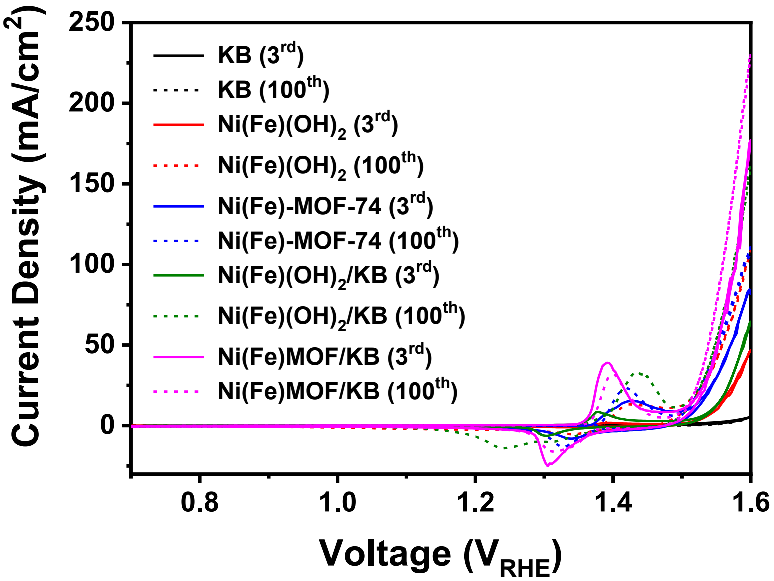

Figure S11. Comparison of CV curves collected after 3 and 100 cycles for KB, Ni(Fe)(OH)$_2$, Ni(Fe)-MOF-74, Ni(Fe)(OH)$_2$/KB, and Ni(Fe)-MOF/KB.

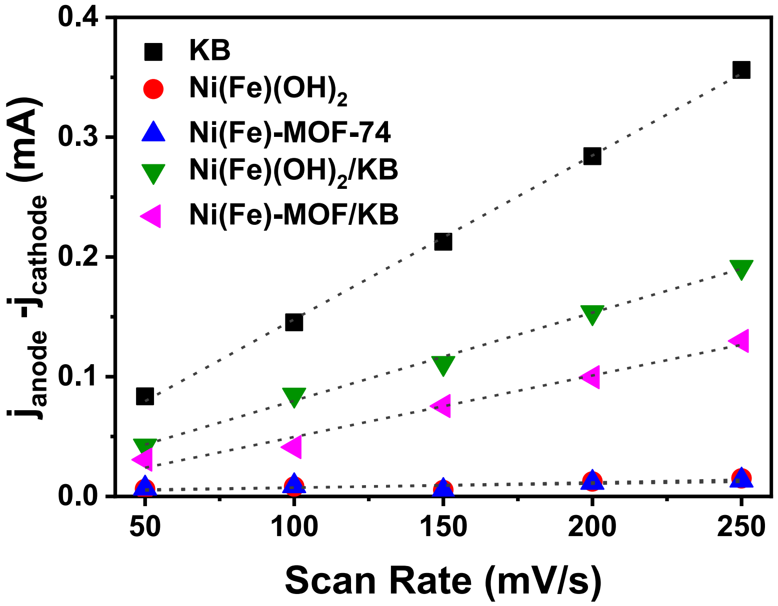

Figure S12. Capacitive current differences (j_{anode} – $j_{cathode}$) versus scan rates for KB, Ni(Fe)(OH)$_2$, Ni(Fe)-MOF-74, Ni(Fe)(OH)$_2$/KB, and Ni(Fe)-MOF/KB.

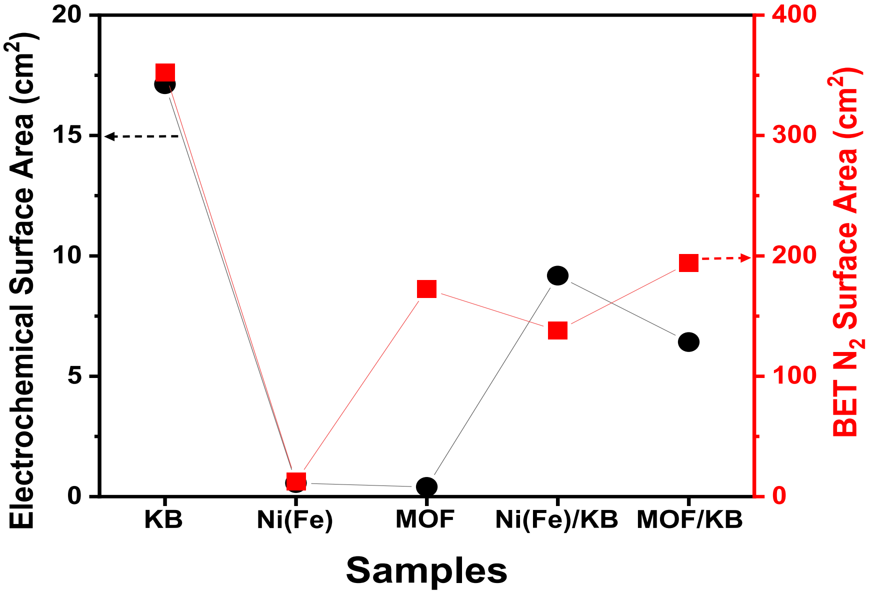

Figure S13. Comparison of the current density divided by the electrochemical surface area and the N_2 BET surface area for KB, $Ni(Fe)(OH)_2$, Ni(Fe)-MOF-74, $Ni(Fe)(OH)_2$/KB, and Ni(Fe)-MOF/KB.

References

---

[1] L. Valenzano, J. G. Vitillo, S. Chavan, B. Civalleri, F. Bonino, S. Bordiga, C. Lamberti, *Catal. Today* **2012**, *182*, 67–79.

[2] W. Wong-Ng, J. A. Kaduk, H. Wu, M. Suchomel, *Powder Diffraction* **2012**, *27*, 256–262.

[3] X. Zhao, B. Pattengale, D. Fan, Z. Zou, Y. Zhao, J. Du, J. Huang, C. Xu, *ACS Energy Lett*. **2018**, *3*, 2520–2526.

[4] J. Xing, K. Guo, Z. Zou, M. Cai, J. Du, C. Xu, *Chem. Commun*. **2018**, *54*, 7046–7049.

[5] P. Man, B. He, Q. Zhang, Z. Zhou, C. Li, Q. Li, L. Wei, Y. Yao, *J. Mater. Chem. A* **2019**, **7**, 27217–27224.

[6] H. Jiang, Y. Guo, T. Wang, P. L. Zhu, S. Yu, Y. Yu, X. Z. Fu, R. Sun, C. P. Wong *RSC Adv*. **2015**, 12931–12936.

[7] T. Fan, F. Yin, H. Wang, X. He, G. A. Li, *Int. J. Hydrogen Energy* **2017**, *42*, 17376–17385.

[8] X. Zhou, Z. Xia, Z. Zhang, Y. Ma, Y. Qu, *J. Mater. Chem. A* **2014**, *2*, 11799–11806.

[9] L. Wang, Y. Wu, R. Cao, L. Ren, M. Chen, X. Feng, J. Zhou, B. Wang, *ACS Appl. Mater. Interfaces* **2016**, *8*, 16736–16743.

[10] G. Hai, X. Jia, K. Zhang, X. Liu, Z. Wu, G. Wang, *Nano energy* **2018**, *44*, 345–352.

[11] D. Zhu, J. Liu, L. Wang, Y. Du, Y. Zheng, K. Davey, S. Z. Qiao, *Nanoscale* **2019**, *11*, 3599–3605.

[12] K. Rui, G. Zhao, Y. Chen, Y. Lin, Q. Zhou, J. Chen J. Zhu, W. Sun, *Adv. Funct. Mater.* **2018**, *28*, 1801554.

[13] J. Li, W. Huang, M. Wang, S. Xi, J. Meng, K. Zhao, J. Jin, W. Xu, Z. Wang. X. Liu, Q. Chen, L. Xu, X. Liao, Y. Jiang, K. A. Owusu, B. Jiang, C. Chen, D. Fan. L. Zhou, L. Mai, *ACS Energy Lett*. **2019**, *4*, 285–292.

[14] M. Gao, W. Sheng, Z. Zhuang, Q. Fang, S. Gu, J. Jiang, Y. Yan, *J. Am. Chem. Soc.* **2014**, *136*, 7077–7084.

[15] K. Yan, M. Sheng, X. Sun, C. Song, Z. Cao, Y. Sun, *ACS Appl. Energy Mater*. **2019**, *2*, 1961–1968.

[16] X. Zhao, X. Ding, Y. Xia, X. Jiao, D. Chen, *ACS Appl. Nano Mater.* **2018**, *1*, 1476–1483.

4. Unpublished Work

In this section the unpublished results which were also done during the doctoral thesis from May 2017 untill February 2021.

4.1 Ni-MOF-74 and Fe-Ni-MOF-74 derivatives as electrocatalysts for electrochemical oxygen evolution reaction

In this study, Ni-MOF-74 and Fe-Ni-MOF-74 with different metal ratios were synthesized and characterized. Following, all these synthesized MOFs were calcined under air atmosphere and characterized. The prepared MOF derivatives were tested for electrochemical oxygen evolution reaction.

Synthesis and characterization of Ni-MOF-74 and Fe-Ni-MOF-74 series

Ni-MOF-74 and Fe-Ni-MOF-74 with different Fe to Ni atomic ratios were synthesized according to the literature with small modifications[117], which are explained in the experimental part. The atomic ratio of iron over nickel in MOF-74 was adjusted to 1:1, 1:4, 1:8, 1:12, 1:16, 1:32, 1:64 and 0:1, respectively, by varying the amounts of Fe(II)acetate and $Ni(NO_3)_2 \cdot 6H_2O$ precursors. Total molar concentration of metal precursors was kept same. As the Fe content decreased in materials, the color changed from darker green to lighter green as visible in Figure 11.

Figure 11. Synthesized MOF-74 samples from left to right with Fe/Ni ratio of 1:1, 1:4, 1:8, 1:12, 1:16, 1:32, 1:64 and 0:1.

The materials were first characterized with Powder X-ray diffraction (PXRD) where all patterns display a very similar pattern to this of the simulated Ni-MOF-74, confirming the successful framework maintenance (Figure 12). It can be concluded that all mixed metal MOF-74 samples feature the similar crystal structure with single-metal Ni-MOF-74.

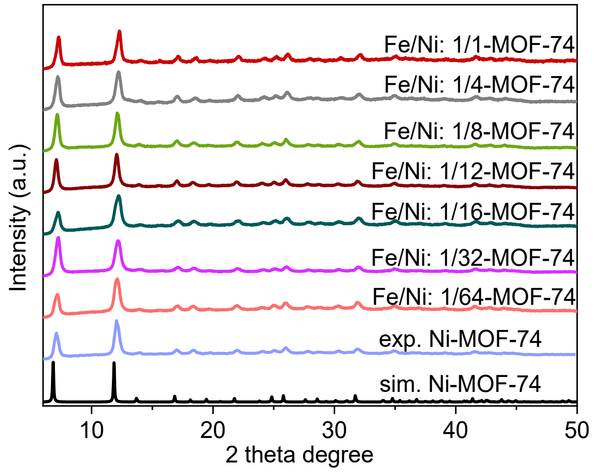

Figure 12. PXRD patterns of simulated Ni-MOF-74 (CCDC number: 1494751) and all experimental synthesized materials.

N_2-sorption measurements were performed in order to gain information about the Brunauer-Emmett-Teller (BET) surface area of the materials. All materials display similar isotherms and BET surface areas (Figure 13). The BET results were lower than expected due to the differences in the activation protocol.

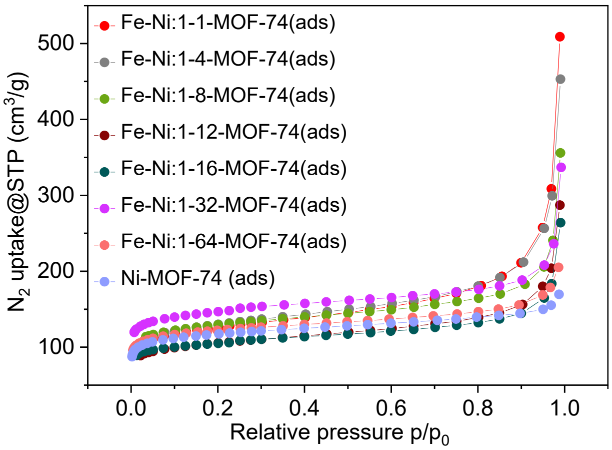

	BET surface area
Fe/Ni:1/1-MOF-74	470 m^2/g
Fe/Ni:1/4-MOF-74	486 m^2/g
Fe/Ni:1/8-MOF-74	491 m^2/g
Fe/Ni:1/12-MOF-74	398 m^2/g
Fe/Ni:1/16-MOF-74	403 m^2/g
Fe/Ni:1/32-MOF-74	561 m^2/g
Fe/Ni:1/64-MOF-74	464 m^2/g
Ni-MOF-74	445 m^2/g

Figure 13. N_2-sorption measurements and BET surface areas of all synthesized materials.

Scanning electron microscopic pictures showed that the materials consisted of particles with irregular shapes and wide particle size distributions (Figure 14). Atomic ratios of nickel and iron in the materials that are listed in Table 2 were obtained via multipoint SEM-EDX.

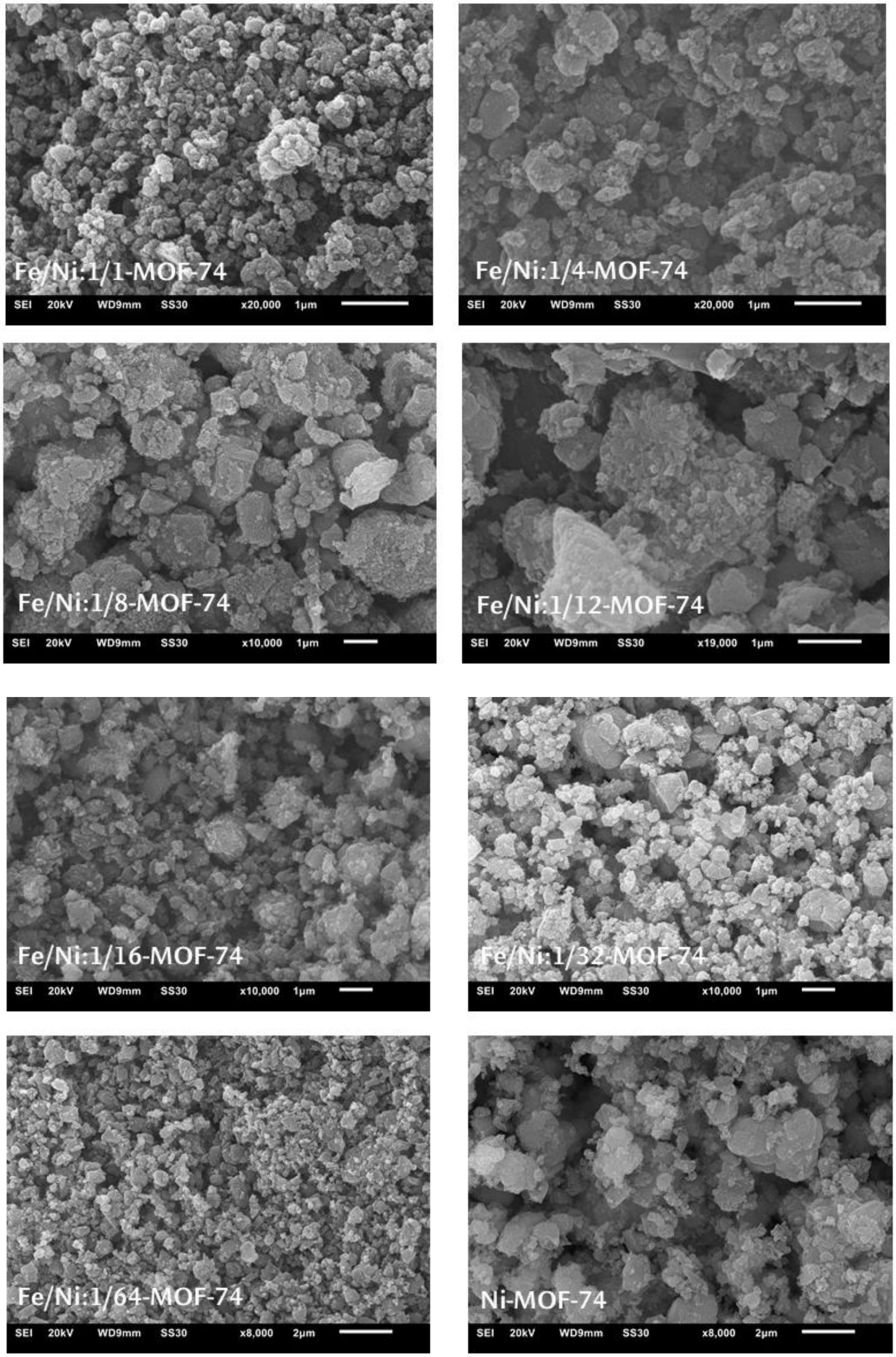

Figure 14. SEM images of Ni-MOF-74, Fe-Ni-MOF-74 with Fe/Ni ratios of 1:1, 1:4, 1:8, 1:12, 1:32 and 1:64.

Table 2. Atomic ratio of iron and nickel in materials according to SEM-EDX.

	Iron	Nickel		Iron	Nickel
Fe/Ni:1/1-MOF-74	1	1	Fe/Ni:1/16-MOF-74	1	16
Fe/Ni:1/4-MOF-74	1	4	Fe/Ni:1/32-MOF-74	1	33
Fe/Ni:1/8-MOF-74	1	8	Fe/Ni:1/64-MOF-74	1	65
Fe/Ni:1/12-MOF-74	1	13			

Preparation and Characterization of Ni-MOF-74 and Fe-Ni-MOF-74 derivatives

The synthesized Ni-MOF-74 and Fe-Ni-MOF-74 series were calcined at 350 °C for 2h under air atmosphere. The colour of the materials changed to dark brown or black after calcination (Figure 15).

Figure 15. Pictures of the calcined MOF-74 materials from left to right with the Fe: Ni ratio of 1:1, 1:4, 1:8, 1:12, 1:16, 1:32, 1:64 and 0:1.

Resulted materials were characterized with PXRD. On the left side of Figure 16, the PXRD results of the first calcined batch are presented. As shown in Figure 16, for the sample Fe-Ni-MOF-74 with the Fe/Ni ratio of 1:1, the reflexes are corresponding to $Fe_{1.7}Ni_{1.43}O_4$ (nickel iron oxide trevorite) and NiO (nickel oxide bunsenite) phases. As the Fe ratio decreases for all other materials, one sees NiO (nickel oxide bunsenite) and in some cases Ni (cubic) phases. Following the electrochemical oxygen evolution reaction investigations, in order to check the reproducibility, calcination has been repeated with the same synthesized MOF-74 batch under identical conditions with the first calcination. In Figure 16 on the right side the PXRD patterns of calcined materials are given. As it is shown, there were some differences for the Fe-Ni-MOF-74 with Fe/Ni ratios of 1:4, 1:8, 1:12 and 0:1. After this observation, we decided to change the calcination parameters by increasing the time. In Figure 17, the PXRD results of two identical calcinations at 350 °C for 5h from the same batch materials are shown. As it is seen, the reproducibility of the materials could not be achieved for all materials. No further investigations were performed because of the reproducibility problem.

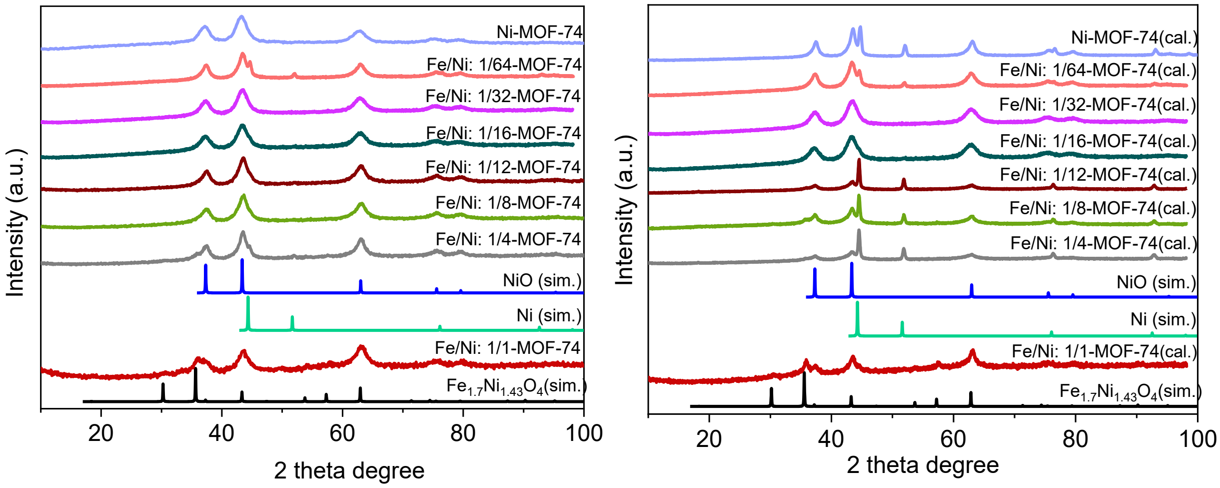

Figure 16. PXRD pattern of the materials that are calcined at 350 °C for 2h (sim. $Fe_{1.7}Ni_{1.43}O_4$ CCDC no: 1006116, sim. NiO CCDC no: 1010093, sim. Ni CCDC no: 2100637).

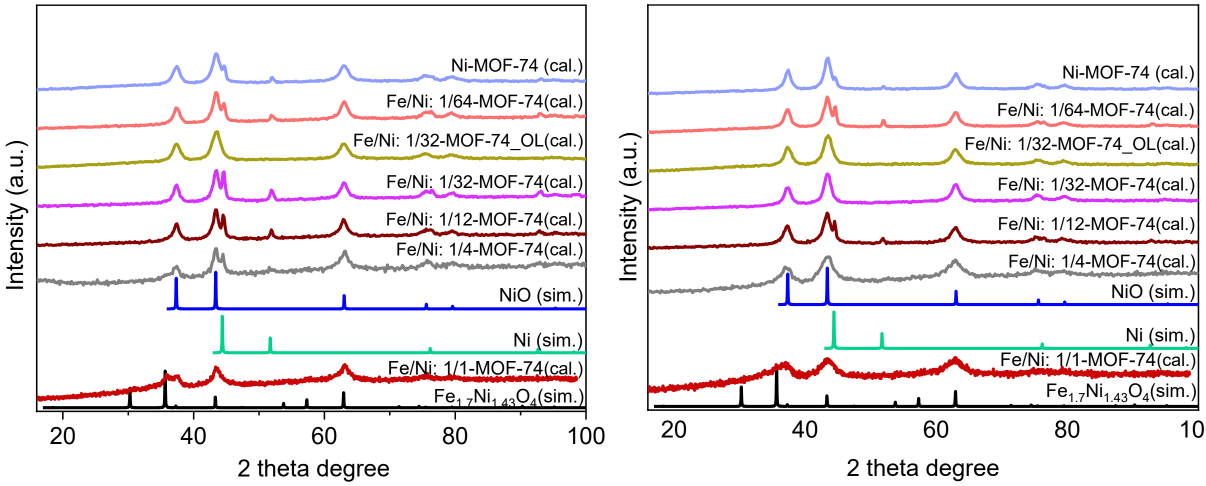

Figure 17. PXRD pattern of the materials that are calcined at 350 °C for 5h (sim. $Fe_{1.7}Ni_{1.43}O_4$ CCDC no: 1006116, sim. NiO CCDC no: 1010093, sim. Ni CCDC no: 2100637).

Electrochemical OER results of the materials

The catalytic activity toward electrochemical oxygen evolution reaction was tested with all calcined Fe-Ni-MOF-74 and Ni-MOF-74. The performance of the materials was checked with the rotating disc electrode in a three-electrode cell configuration in 1 mol/L KOH. As shown in Figure 18, the initial linear scans (LSV) of all materials posses slightly improving activities. Following the first three LSV, cyclic voltammetry (CV) measurements were performed between 0.7 and 1.6 V vs RHE in 1 mol/L KOH electrolyte and subsequently linear scans were collected after 50 CV scans. These linear scans after CV measurements showed stabilized activity of the material. The best performance was achieved with Fe-Ni-MOF-74 with Fe/Ni: 1:16 and 1:32 which required an overpotential of 348 and 349 mV to reach a current density of 10 mA/cm^2 and a current density of 78 and 75 mA/cm^2 at 1.7 V respectively. On the other hand, the lowest performance was obtained with the calcined Ni-MOF-74 that showed an overpotential of 426 mV to reach a current density of 10 mA/cm^2. All detailed electrochemical performance data of the materials are shown in Table 3.

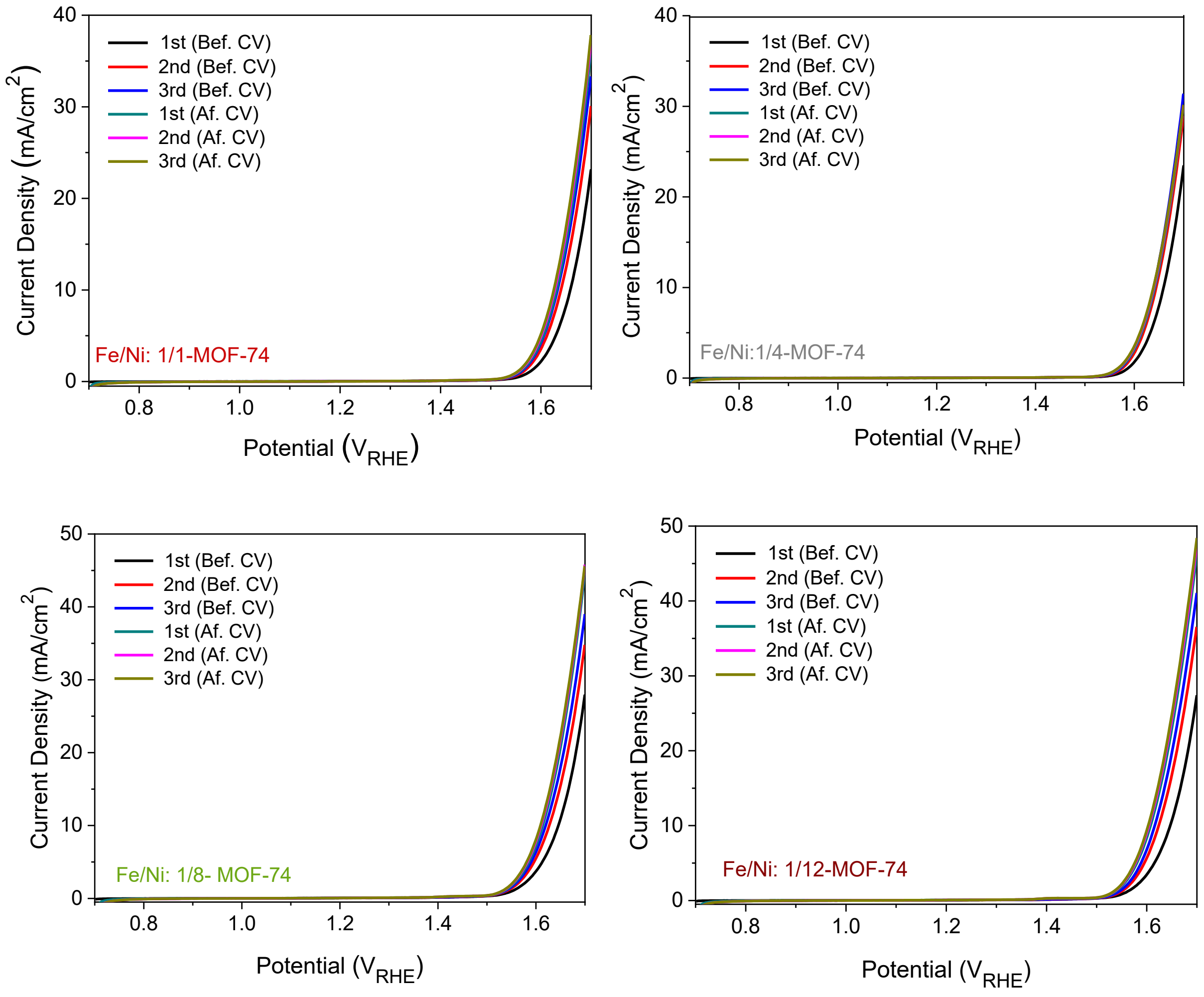

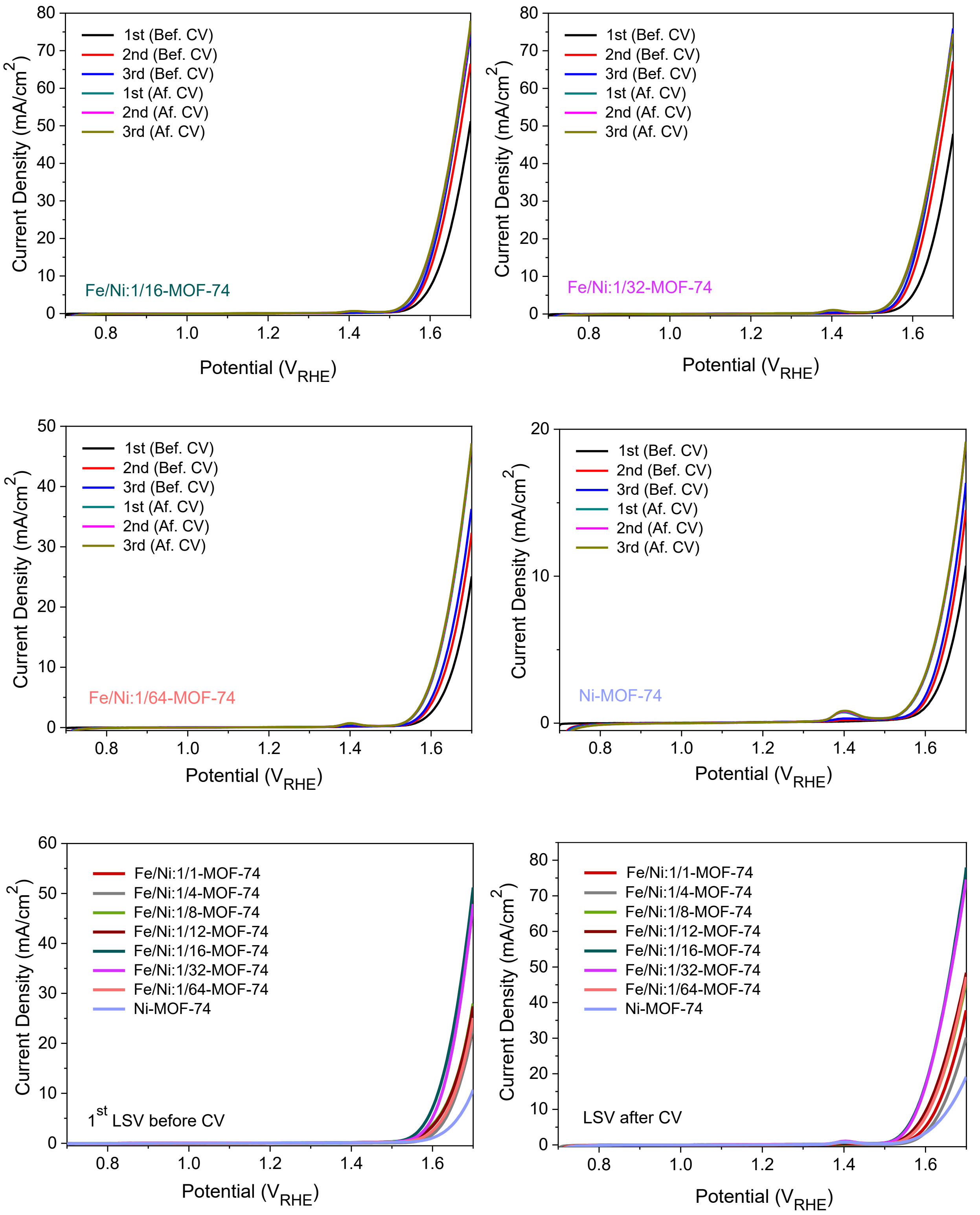

Figure 18. Initial linear scans and stabilized linear scans (after activation using cyclic voltammetry) of all synthesized materials.

Table 3. Electrochemical performance data of the all materials for electrochemical OER.

Material	**Before CV 1st LSV**		**Before CV 3rd LSV**		**After CV**	
	η at *j* = 10 mA/cm^2 (mV)	***j* at E = 1.7 V vs. RHE (mA/cm^2)**	**η at *j* = 10 mA/cm^2 (mV)**	***j* at E = 1.7 V vs. RHE (mA/cm^2)**	**η at *j* = 10 mA/cm^2 (mV)**	***j* at E = 1.7 V vs. RHE (mA/cm^2)**
Fe/Ni:1/1-MOF-74 (cal.)	428	23	403	33	395	38
Fe/Ni:1/4-MOF-74 (cal.)	429	24	409	31	408	30
Fe/Ni:1/8-MOF-74 (cal.)	415	28	389	39	378	46
Fe/Ni:1/12-MOF-74 (cal.)	416	27	385	41	372	48
Fe/Ni:1/16-MOF-74 (cal.)	383	51	357	75	348	78
Fe/Ni:1/32-MOF-74 (cal.)	393	48	359	76	349	75
Fe/Ni:1/64-MOF-74 (cal.)	424	25	399	36	379	47
Ni-MOF-74 (cal.)	466	11	441	17	426	19

4.2 Co_3O_4/CTF-1 as an electrocatalyst for electrochemical oxygen evolution reaction

In this study, CTF-1 and Co_3O_4/CTF-1 composite material was synthesized and characterized. The composite was tested for electrochemical oxygen evolution reaction.

Synthesis and characterization of CTF-1

CTF-1 is synthesized by ionothermal method according to the literature[45]. A mixture of dicyanobenzene and anhydrous zinc chloride were placed into a quartz ampoule under inert atmosphere. This ampule was evacuated, sealed and heated to 400 °C for 48h. The resulted black product was washed with several solvents and dried under vacuum. The experimental details are explained in the experimental part. CTF-1 is characterized with PXRD, N_2-sorption, elemental analysis, TGA and SEM.

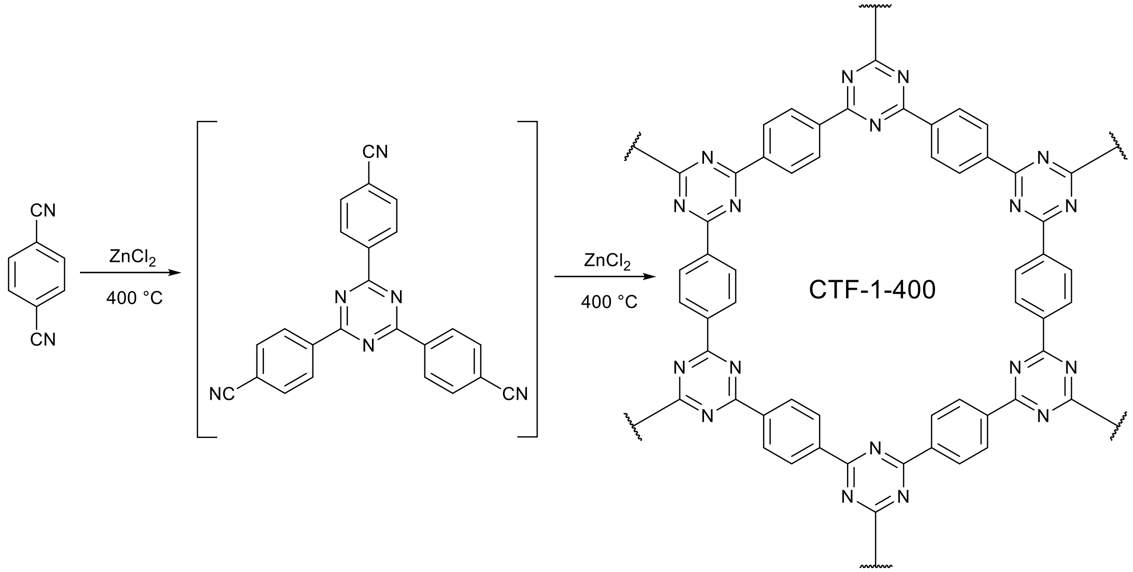

Figure 19. Schematic illustration of idealized CTF-1 structure synthesized via ionothermal method.

The PXRD pattern of CTF-1 in Figure 20 showed characteristic broad reflections at 8° and 22° 2θ corresponding to the (100) and (001) planes which are known from the literature. Prior to nitrogen sorption measurements, CTF-1 was activated by degassing at 150 °C for 15h. Nitrogen sorption data of CTF-1 showed a type I isotherm with a BET surface area of 954 m^2/g (Figure 20). The total pore volume was found to be 0.45 cm^3/g at $p/p_0 = 0.95$. Elemental analysis yielded the expected C, H and N content, in agreement with the previous literature sources (Table 4). TGA revealed the decomposition of the CTF-1 after 400 °C as visible in Figure 21. The SEM picture of CTF-1 displays the shard morphology with a wide particle size distribution. Slight impurities of chlorine and zinc have been found by EDX analysis (Figure 22).

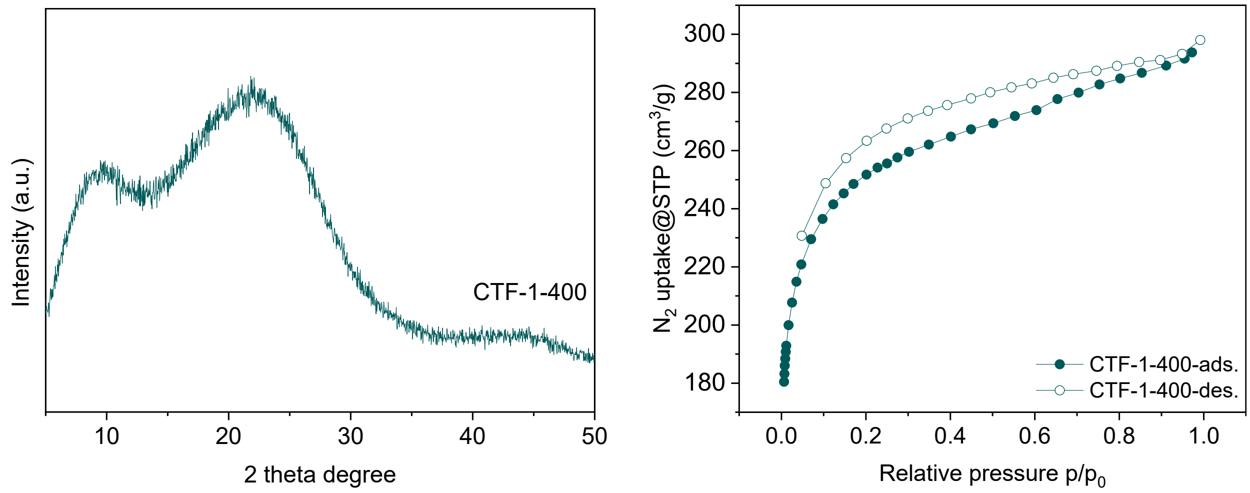

Figure 20. PXRD pattern (left) and N_2 sorption isotherm (right) of synthesized CTF-1.

Table 4. Elemental analysis of CTF-1.

Compound	**C (wt.%)**	**N(wt.%)**	**H(wt.%)**	**C/N atom**	**Rest(wt.%)**
Calculated*	74.99	21.86	3.15	4	-
CTF-1	**75.92**	**14.54**	**2.75**	**6.1**	**6.79**
Lit 1	72.03	13.82	2.96	6.08	11.9
Lit 2	66.97	12.90	2.53	6.05	17.60

* Calculation is based on idealized structure of CTF-1.

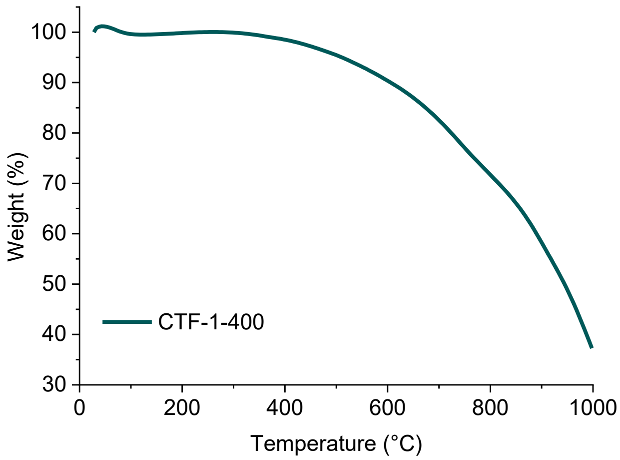

Figure 21. TGA picture of synthesized CTF-1.

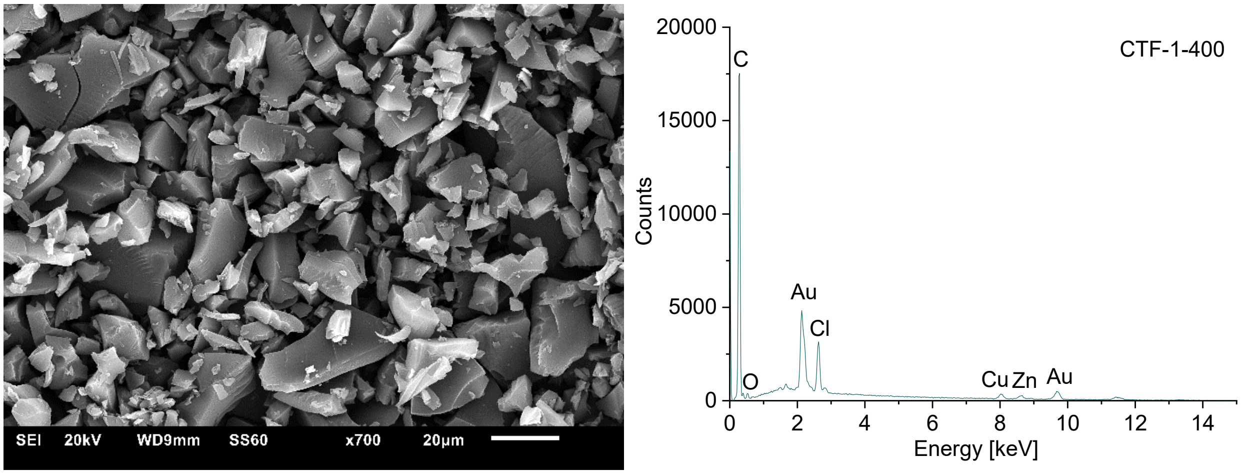

Figure 22. SEM picture (left) and EDX analysis (right) of synthesized CTF-1.

Synthesis and characterization of Co_3O_4/CTF-1

Co_3O_4/CTF-1 was synthesized according to the literature[118] (Figure 23), which is explained in the experimental part in detail.

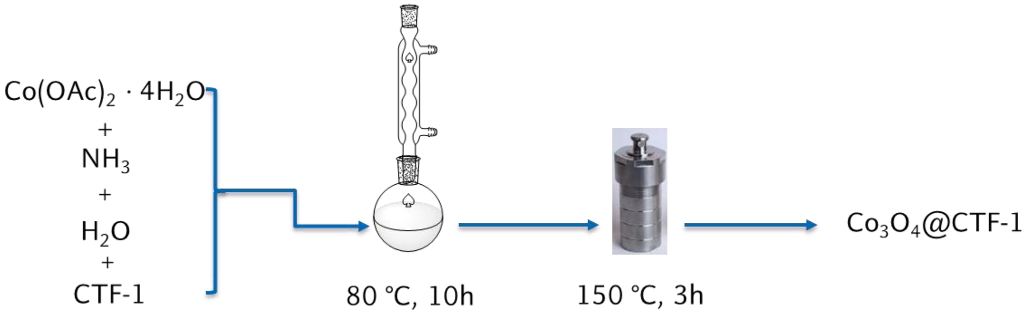

Figure 23. Schematic illustration of Co_3O_4/CTF-1 synthesis.

The composite material was first characterized with PXRD. As presented in Figure 24, the composite material shows the characteristic reflexes of Co_3O_4 (COD number:1538531) at 2θ = 31.5°, 37°, 44.8°, 59.6° and 65.3°.

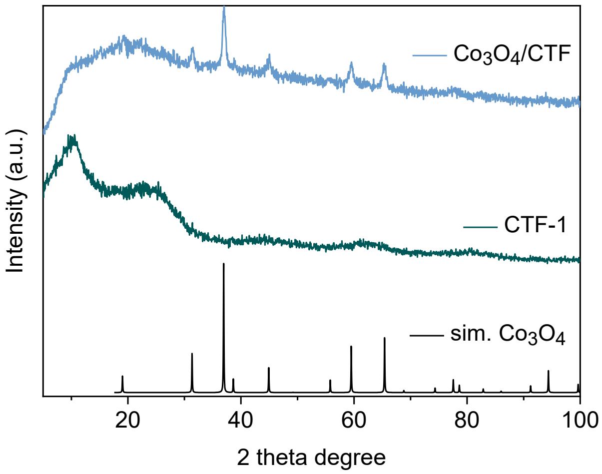

Figure 24. PXRD data of simulated Co_3O_4 (COD number: 1538531), CTF-1 and Co_3O_4/CTF-1.

The adsorption/desorption isotherms of Co_3O_4/CTF-1 are depicted in Figure 25. The BET surface area of the material was found to be 586 m^2/g. This result showed that the BET surface area of CTF-1 decreased from 954 m^2/g to 586 m^2/g as the Co_3O_4 nanoparticles were incorporated to the CTF structure.

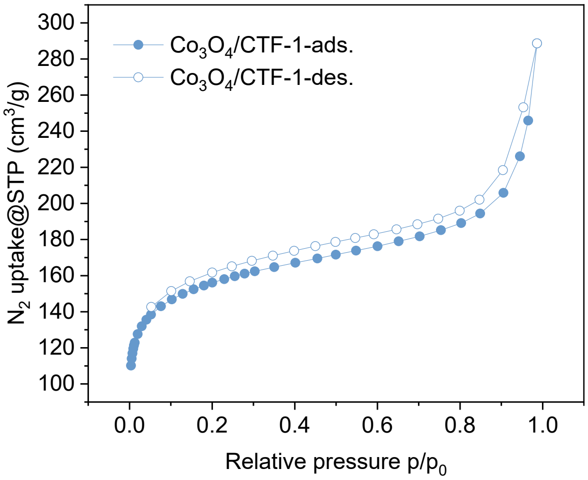

Figure 25. N_2 sorption data of Co_3O_4/CTF-1.

Electrochemical OER results of Co_3O_4/CTF-1

The catalytic activity toward electrochemical oxygen evolution reaction was tested with Co_3O_4/CTF-1. As shown in Figure 26, the initial linear scans (LSV) posses similar but slightly improving activities. Following the first three LSV, cyclic voltammetry (CV) measurements were performed between 0.7 and 1.6 V vs RHE in 1 mol/L KOH electrolyte and subsequently linear scans were collected after 50 CV scans. These linear scans after CV measurements showed stabilized activity of the material. Co_3O_4/CTF-1 required an overpotential of 435 mV to reach a current density of 10 mA/cm^2 and a current density of 16 mA/cm^2 at 1.7 V according to the first LSV. This performance improved and stabilized after CV measurements which was resulted with an overpotential of 412 mV to reach a current density of 10 mA/cm^2 and a current density of 38 mA/cm^2 at 1.7 V.

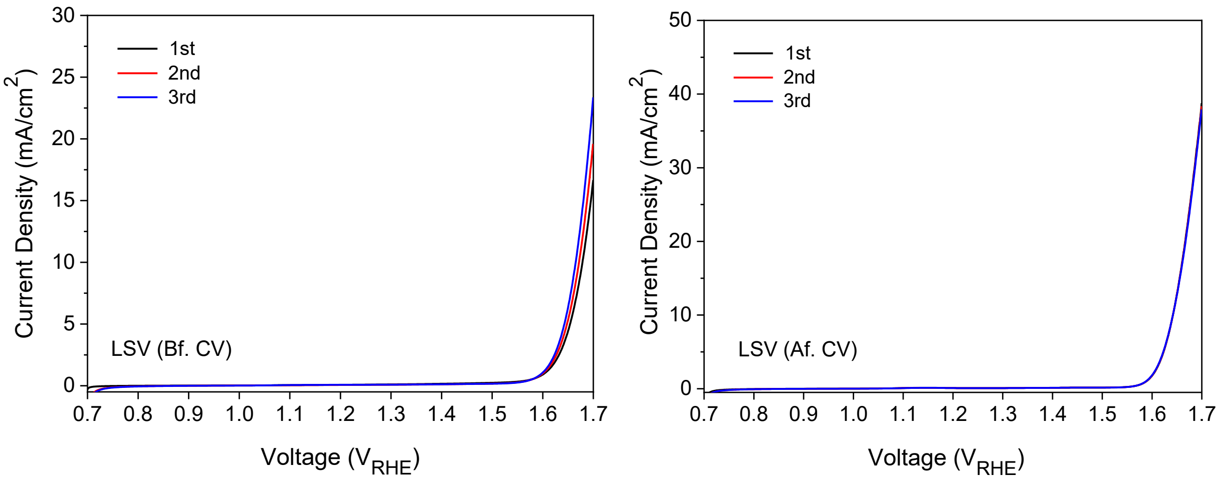

Figure 26. Initial and activated LSV curves of Co_3O_4/CTF-1.

However, the electrochemical activity of the catalyst is not sufficient when it is compared with benchmark OER catalysts (around < 0.36 V to reach a current density of 10 mA/cm^2). Therefore, no further investigation was performed for this project.

5. X-ray Photoelectron Spectroscopy (XPS) Investigations and co-Author Contributions

A contribution was made as co-author for the publications listed in the following chapters 5.1-5.4. X-ray Photoelectron Spectroscopy (XPS) measurements were performed to investigate the surface composition and the elemental chemical states of the materials for the publications in chapters 5.1-5.3. XPS results were evaluated with CasaXPS and XPS spectra together with the evaluation/interpretation of related parts for the manuscript were prepared for publication. For chapter 5.4, the covalent triazine framework (CTF-1) was synthesized in two different temperatures at 400 °C and 600 °C and fully characterized with PXRD, EA, TGA, N_2-sorption, SEM and EDX. Prepared materials together with characterization data were given to the first-author for further investigations.

5.1. Modulated synthesis of thiol-functionalized fcu and hcp UiO-66(Zr) for the removal of silver(I) ions from water

B. Moll, T. Müller, C. Schlüsener, A. Schmitz, P. Brandt, **S. Öztürk**, C. Janiak

Materials Advances, **2021**, *2*, 804–812 DOI: 10.1039/D0MA00555J

Summary:

In this work, two modified thiol-containing UiO-66 MOFs were synthesized and characterized. Mercaptoacetic acid (HMAc) was used as a modifier and the usage of different equivalent HMAc in relation to $ZrCl_4$ led to either fcu topology (10, 30 and 50 eq.) or hcp topology (100 eq). The resulted materials were used for the removal of Ag(I) from an aqueous solution. The incorporation of modulator ligands with free thiol groups resulted in enhanced uptake of Ag^+ from aqueous solutions compared to non-functionalized UiO-66. The UiO-66-Mac-50eq and UiO-66-Mac-100 eq. showed a maximum uptake of 84 mg/g and 32 mg/g respectively.

Own contribution to the publication:

- Performing XPS measurements
- Evaluation and interpretation of the XPS spectra with CasaXPS
- Graphic representation and writing the related part for the manuscript
- Review and correction of the final manuscript as a co-author

XPS measurements were performed in order to investigate the surface composition and the chemical state of the Ag for UiO-66-Mac-50eq and UiO-66-Mac-100eq. Both survey spectra displayed Ag, Zr, C, O and S in both of the materials. High resolution Ag 3d XPS spectra of UiO-66-Mac-50eq and UiO-66-Mac-100eq showed the oxidation state of silver as a mixture of predominantly Ag(0) and to a minor extent of Ag(I). Peak positions at 368.2 eV, 374.1 eV for UiO-66-Mac-50eq and 368.3 eV, 374.3 eV for UiO-66-Mac-100eq together with the 6 eV doublet splitting indicated the metallic state of silver. Another spin orbit pair with higher binding energies at 369.4 eV and 375.4 eV for UiO-66-Mac-50eq, 369.2 eV and 375.2 eV for UiO-66-Mac-100eq indicated the presence of silver (I) ions bonding with thiol groups.

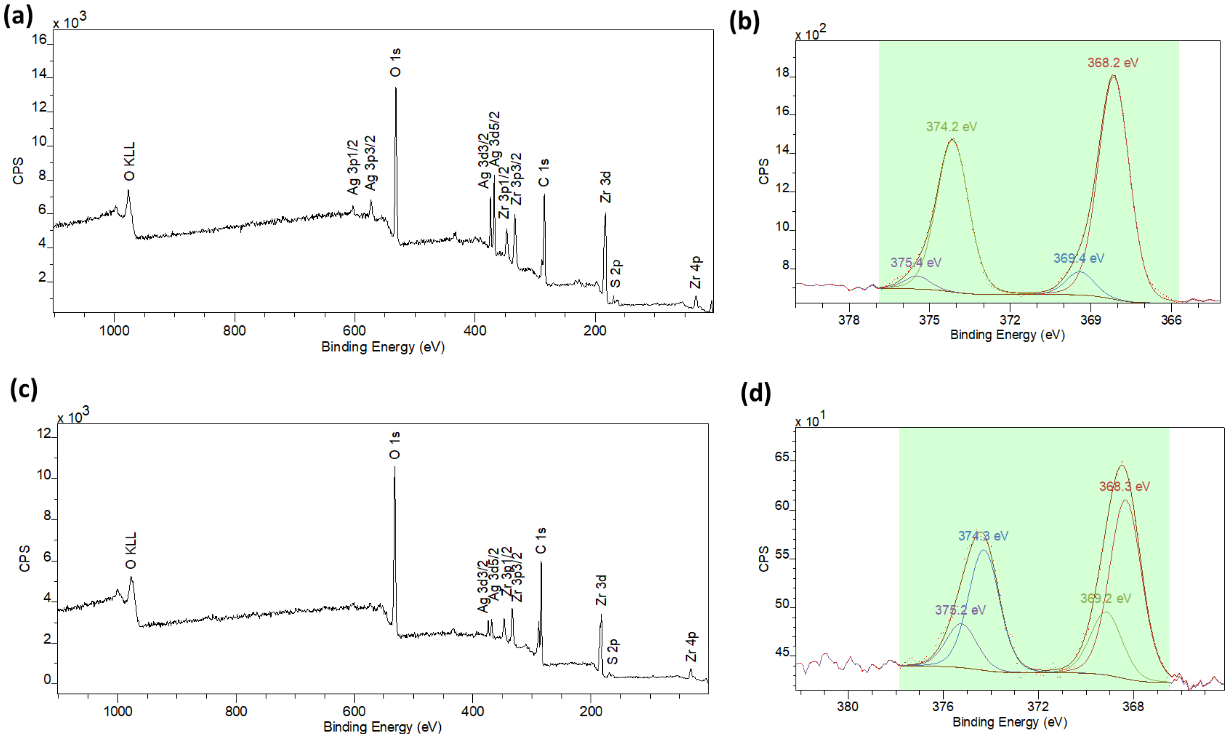

Figure 27. Survey XPS spectra of (a) UiO-66-50eq and (c) UiO-66-100eq and high resolution Ag 3d XPS spectra of (b) UiO-66-50eq and (d) UiO-66-100eq.

5.2. A mixed-valence copper(I/II) coordination polymer directed with a bifunctional soft-hard pyrazolate-carboxylate ligand

S. Menzel, S. P. Höfert, **S. Öztürk**, a: Schmitz, C. Janiak

Z. Anorg. Allg. Chem., accepted. DOI: 10.1002/zaac.2020000428

Summary:

One dimensional, mixed valent Cu(I/II) coordination polymer with the formula $[Cu^{II}\{Cu^{I})_3(Hmpba)(mpba)_2\}DMF]\cdot{\sim}3DMF$ (**1**) was obtained via solvothermal method with the presence of bifunctional ligand 4-(3,5-dimethyl-1*H*-pyrazol-4-yl)benzoic acid (H_2mpba) in *N,N*-dimethylformamide (DMF). XPS confirmed the Cu(I): Cu (II) ratio as 3:1 in the structure same as the determined formula ratio of **1**.

Own contribution to the publication:

- Performing XPS measurements
- Evaluation and interpretation of the XPS spectra with CasaXPS
- Graphic representation and writing the related part for the manuscript
- Review and correction of the final manuscript as a co-author

XPS was performed to investigate the surface composition and quantify the two different oxidation states of Cu in the **1**. The survey spectrum confirmed the presence of Cu, O, N and C in the **1**. The high resolution Cu 2p spectrum displayed the core bands at 952.9 eV and 933.1 eV for Cu 2p1/2 and Cu 2p3/2 respectively. The peaks at 933.1 eV and 934.1 eV correspond to the typical positions of Cu(I) and Cu(II) respectively and the area ratio of these peaks matched the determined Cu(I):Cu(II) ratio of 3:1 in the formula ratio of **1**.

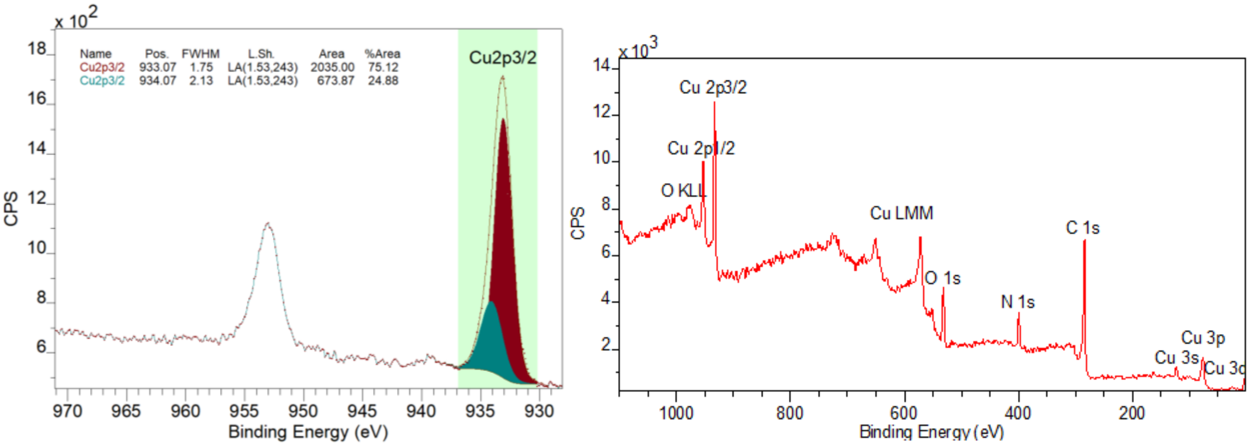

Name	Pos.	FWHM	L.Sh.	Area	%Area
Cu2p3/2	933.07	1.75	LA(1.53,243)	2035.00	75.12
Cu2p3/2	934.07	2.13	LA(1.53,243)	673.87	24.88

Figure 28. High resolution Cu 2p XPS spectrum (left) and survey spectrum (right) for $[\mathrm{Cu^{II}\{Cu^{I})_3(Hmpba)(mpba)_2\}DMF]\cdot{\sim}3DMF}$.

The fitting of the C 1s spectrum of 1 displayed three peaks centered at 284.7, 285.7 and 288.6 eV that can be assigned to C-C/C=C/C-H, C-N and –COO respectively. The N 1s spectrum showed two peaks at 399.2 and 400.1 eV that can be attributed to imine and amine nitrogen respectively. The O 1s peak observed at 531.5 eV confirmed the presence of copper bound oxygen and the peak at 532.8 eV represented the non-coordinated carboxyl oxygen.

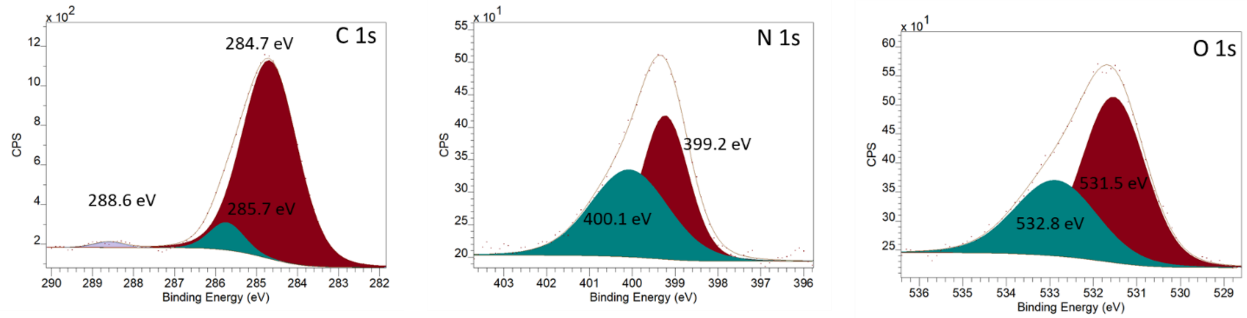

Figure 29. High resolution spectra of C 1s, N 1s and O 1s (from left to right respectively) for $[Cu^{II}\{Cu^{I})_3(Hmpba)(mpba)_2\}DMF]\cdot{\sim}3DMF$.

5.3. One-Pot Shaping: Cucurbituril−Encapsulating Metal−Organic Framework via Mechanochemistry

J. Liang, V. Gvilava, C. Jansen, **S. Öztürk**, A. Spieß, J. Lin, R. Cao and C. Janiak,

Angewandte Chemie, submitted.

Summary:

MC5@MIL-100(Fe) hybrid monoliths were prepared with reaction of 1,3,5−benzenetricarboxylic acid (H_3BTC) and $Fe(NO_3)_3.9H_2O$ in the presence of decamethylcucurbit[5]uril (MC5). The resulted composite showed increased uptake and selective capture of lead(II) cations at low concentrations.

Own contribution to the publication:

- Performing XPS measurements
- Evaluation and interpretation of the XPS spectra with CasaXPS
- Graphic representation and writing the related part for the manuscript
- Review and correction of the final manuscript as a co-author

XPS was performed in order to investigate the surface composition and the interactions between Pb and MC5@MIL-100(Fe)-23. The survey spectra of MC5@MIL-100(Fe)-23 (before lead ion adsorption) showed the presence of Fe, O, N and C, whereas Pb-MC5@MIL-100(Fe)-23 (after lead ion adsorption) displayed the Fe, O, N, C and Pb as expected. High resolution XPS spectrum of Pb 4f for Pb-MC5@MIL-100(Fe)-23 indicated the core peaks at 139.3 eV and 144.2 eV that are assigned to Pb(II). Compared to pure $Pb(NO_3)_2$, 0.3 eV shift to lower binding energy for Pb 4f confirmed the modest interactions between Pb(II) ions and MC5 cages in the hybrid.

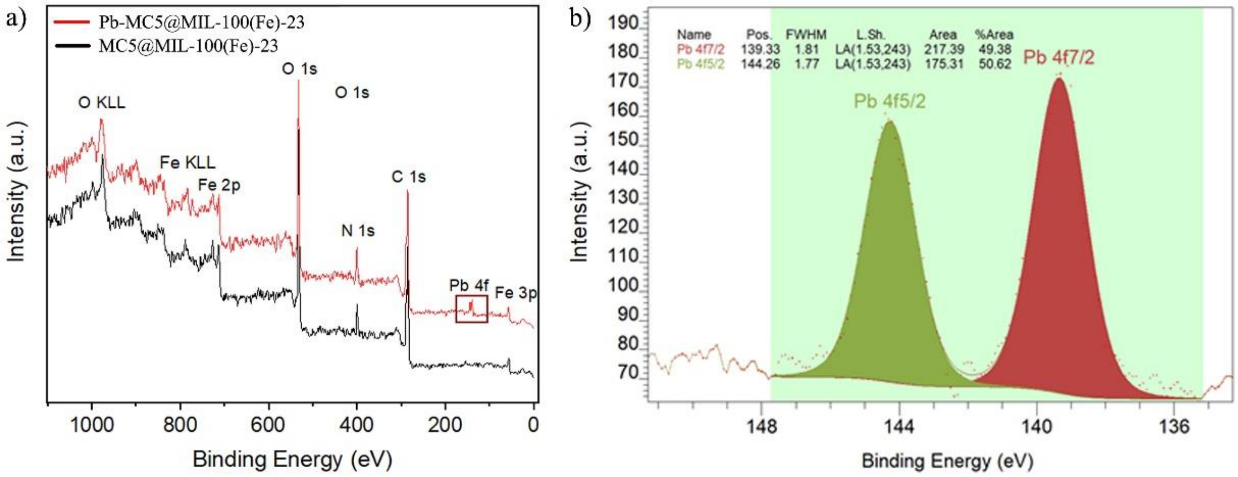

Figure 30. a) XPS survey spectra of MC5@MIL−100(Fe)−23 before and after adsorption of Pb(II) at 15 ppm (Pb−MC5@MIL−100(Fe)−23). b) High resolution Pb 4f XPS spectra of Pb−MC5@MIL−100(Fe)−23.

5.4. Comparative evaluation of different MOF and non-MOF porous materials for SO_2 adsorption and separation

P. Brandt, A. Nuhnen, **S. Öztürk**, G. Kurt, J. Liang and C. Janiak

Advanced Sustainable Systems, accepted, DOI: 10.1002/adsu.202000285

Summary:

A comparative experimental study of SO_2 adsorption by porous materials including MOFs and CTFs was carried out. Microporous materials with pore size of 4-8 Å or nitrogen heterocycles were found to be optimal for SO_2 uptake at low pressure range. Zeolite Y and CTF-1-600 showed the most promising SO_2/CO_2 selectivity.

Own contribution to the publication:

- Synthesis of CTF-1-400 and CTF-1-600.
- Characterization of synthesized CTFs with PXRD, TGA, N_2-sorption, EA, SEM and EDX.
- Review and correction of the final manuscript as a co-author

Chapter 3.1 can be referred for the characterization data of these materials since materials from the same batch were used.

6. Overall Summary

Herein, the work results obtained during the doctoral research focusing on the investigation of covalent triazine framework (CTF) and metal organic framework (MOF) based materials in order to constitute efficient elecrocatalysts for electrochemical oxygen evolution reaction (OER) are summarized.

In the first main research area, CTF based materials were synthesized, characterized, and investigated as electrocatalysts for electrochemical OER. Because of several advantages like easy synthesis, high thermal and chemical stability, cheap and readily available starting materials, high surface area and porosity, CTFs are great of interest in many applications. Nevertheless, CTFs are little investigated for electrocatalysis, especially for oxygen evolution reaction. The attractive properties of CTFs, such as tunable surface area and porosity, high thermal stability combined with the framework inherent nitrogen moieties within that can provide coordination or support for metal species, build the base of the motivation to study them as OER electrocatalysts. As a part of the cooperation with Prof. Dr. Xiao-Yu Yang, electrocatalytic investigations were done in Wuhan University of Technology in China. To the best of our knowledge, until the time the manuscript with the title “Nickel nanoparticles supported on a covalent triazine framework as electrocatalyst for oxygen evolution reaction and oxygen reduction reaction”, which can be found in Section 3.1, was submitted, there were no reports about nickel/CTF catalysts for OER in the literature. The first successful preparation of nickel/CTF materials with high catalytic OER performance and stability, which are even superior than commercial catalyst, can be great of use to the scientific community to further investigate CTFs as potential candidates for OER.

To start with, CTF-1 was synthesized ionothermally and fully characterized using powder X-ray diffraction (PXRD), nitrogen sorption at 77 K, thermogravimetric analysis (TGA), elemental analysis (EA) and scanning electron microscopy (SEM) combined with energy dispersive x-ray spectroscopy (EDX). Benefiting from the tunability of CTF-1, the synthesis was done under two different temperatures, at 400 °C and 600 °C, respectively. CTF-1-600 showed primarily differences in higher BET surface area, higher total pore volume, less nitrogen content and higher conductivity compared to CTF-1-400. Afterwards, the nickel nanoparticles are supported on the precious synthesized CTFs via fast and efficient microwave radiation within 10 min in the presence of an ionic liquid as reaction medium. In total, four composite materials with differentiating nickel amounts on either CTF-1-400 or CTF-1-600 have been characterized by PXRD, nitrogen sorption, transmission electron microscopy (TEM), SEM, x-ray photoelectron spectroscopy (XPS) and flame atomic absorption spectroscopy (AAS). The use of CTF as support for nickel nanoparticles yielded advantages in terms of metal-support interactions where the nitrogen atoms in the framework of the CTF act as anchor points yielding nickel loadings of 20 up to 35 wt % in prepared composite materials according to AAS. All composites showed lower BET surface areas and pore volumes than their corresponding pristine CTF materials which can be attributed to the incorporation of nickel into the voids of the CTF-1. According to XPS, both metallic Ni and Ni^{2+}have been observed and Ni^{2+} is believed to arise from the combination of nickel coordinated with nitrogen from the CTF framework and the oxidation of nickel. In addition to other nitrogen moieties, pyridinic nitrogen and graphitic or quaternary nitrogen have been found in the composite that are known to improve the activity of N-modified carbon materials in literature. Intensive TEM, SEM and STEM studies proved the existence of nickel on the support material CTF. Consequently, all CTF and composite materials were tested for electrochemical OER and oxygen reduction reaction (ORR). In general, the materials based on CTF-1-600 showed much higher OER activity than those based on CTF-1-400. Pristine CTF-1-400 showed almost no activity, whereas Ni supported composites namely Ni/CTF-1-400-20 and Ni/CTF-1-400-35 showed higher activities with overpotentials of 532 mV and 569 mV to reach 10 mA/cm^2 respectively to compared to pristine CTF-1-400. On the other hand, pristine CTF-1-600, Ni/CTF-1-600-22 and Ni/CTF-1-600-33 showed similar OER activities by requiring 376 mV, 376 mV and 374 mV to reach 10 mA/cm^2 respectively. This high electrocatalytic OER performance of CTF-1-600 based materials also outperformed the commercial RuO_2 catalyst which requires 403 mV to reach a current density of 10 mA/cm^2 under the same conditions. The higher electrocatalytic activity of CTF-1-600 over the CTF-1-400 materials is attributed to the better conductivity of the former together with its higher porosity and surface area which enhance the exposure of active sites and improves the ion and charge transfer. CTF-1-600, as a metal-free electrocatalyst, features a better performance than many N-doped carbon materials in the literature too. Yet, the presence of nickel has no significant effect on CTF-1-600 for OER. Accelerated durability tests (ADT) also showed high stability of CTF-1-600 and Ni/CTF-1-600-22 which showed only a very slight change in the performance after 2000 cycles. The same materials were also tested for electrochemical ORR. CTF-1-400, Ni/CTF-1-400-20 and Ni/CTF-1-400-35 displayed similar ORR polarization curves and half-wave potentials of 0.573 V, 0.570 V and 0.576 V, respectively. This showed that the presence of nickel has no significant effect on CTF-1-400 for ORR. On the other hand, CTF-1-600 based materials again showed better performance than CTF-1-400 based materials. The half-wave potential of Ni/CTF-1-600-22 (0.775 V) was larger than that of CTF-1-600 (0.724 V) and Ni/CTF-1-600-33 (0.729 V) indicating a faster dynamic process for ORR and closest to the performance of commercial Pt/C catalyst (0.890 V) for ORR. The good performance of Ni/CTF-1-600-22 is comparable to several nickel/carbon materials from the literature. Here, the highest conductivity of Ni/CTF-1-600-22 coincided with the highest ORR activity. Again ADTs proved the high stability of CTF-1-600 and Ni/CTF-1-600-22.

In the second main research area, MOF based materials were synthesized, characterized and tested for electrochemical OER. As crystalline, porous hybrid materials constructed from organic linkers and inorganic metal clusters, MOFs are potential candidates for electrocatalysis together with many other application areas. The nearly unlimited chemical tunability together with their high surface area and porosity, pristine MOFs as well as MOF composites and MOF derivatives can be promising OER electrocatalysts. In addition, MOFs can be also utilized as support for other catalytically active species. Various pristine MOFs were already investigated for electrochemical OER. Nevertheless, the low electron conductivity of many MOFs hinder their catalytic performance. Conductivity can be improved by developing composites of MOFs together with conductive supports, such as graphene oxide or porous carbon materials. Following this concept, motivation of this research was to prepare MOF composites together with highly electro-conductive ketjenblack (KB) carbon and investigate the OER performance of the resulting materials. Ketjenblack is a porous carbon that combines a high surface area and good electro-conductivity. There are only a few studies that combined KB and MOF and used this composite in different applications. To the best of our knowledge, the study with the title “Highly-Efficient Oxygen Evolution Electrocatalyst Derived from Metal-Organic Framework and Ketjenblack Carbon Material” in Section 3.2, is the first report that investigated a MOF/KB composite as an OER electrocatalyst. In this research, electrochemical tests were performed in Max-Planck Institut für Kohlenforschung in cooperation with Priv. -Doz. Dr. Harun Tüysüz. As a result of this study, MOF/KB composite is proved to be a highly efficient OER electrocatalyst which is superior to many reported OER electrocatalysts and also to the benchmark catalysts. This study helps to initialize many future projects of new composite materials based on ketjenblack with different MOFs as OER catalysts.

First, Ni-MOF-74 was found to be a good candidate to start with due to the advantages of adjustable divalent metal nodes in the structure, a high density of open metal sites and one-dimensional channels with aperture diameters of 1 nm. Since iron doping has been shown to be very effective on improving the OER performance of Ni based materials, we followed this strategy in our study. We first synthesized pristine Ni(Fe)-MOF-74 and Ni(Fe)-MOF/KB via a simple one-step solvothermal method at 120 °C for 24h. For comparison, we also followed the same synthesis procedure only without addition of linker which yielded $Ni(Fe)(OH)_2$ and $Ni(Fe)(OH)_2$/KB. All synthesized materials were characterized in detail with PXRD, Fourier transform infrared (FT-IR), nitrogen sorption at 77 K, AAS, XPS, TEM, SEM (-EDX) and STEM. According to the AAS results the total metal loading was 35 wt% for Ni(Fe)-MOF-74, 17 wt% for Ni(Fe)-MOF/KB, 46 wt% for Ni(Fe)$(OH)_2$ and 25 wt% for Ni(Fe)$(OH)_2$/KB. Additionally, the mass fractions of the metal compounds in the composites were calculated as 47.6 wt% Ni(Fe)-MOF-74 and 52.4 wt% KB for Ni(Fe)-MOF/KB and 53.4 wt% Ni(Fe)$(OH)_2$ and 46.6 wt% KB for Ni(Fe)$(OH)_2$/KB. The BET surface areas of the materials were 684 m^2/g for Ni(Fe)-MOF-74, 770 m^2/g for Ni(Fe)-MOF/KB, 50 m^2/g for Ni(Fe)$(OH)_2$, 547 m^2/g for Ni(Fe)$(OH)_2$/KB and 1399 m^2/g for KB. The nitrogen sorption isotherms, BET surface areas and also pore size distributions of the composites can be seen as a combination of the individual mass-weighted components. XPS Ni 2p and Fe 2p high resolution spectra of Ni(Fe)-MOF-74, Ni(Fe)-MOF/KB, Ni(Fe)$(OH)_2$ and Ni(Fe)$(OH)_2$/KB displayed peaks of Ni^{2+} and Fe^{2+} for all materials. Compared to the XPS Ni 2p spectra of Ni(Fe)-MOF-74, a shift of 0.6 eV to higher binding energy region was seen for Ni(Fe)-MOF/KB, revealing the interaction between ketjenblack carbon and the MOF. Similarly, compared to XPS Fe 2p spectra of Ni(Fe)-MOF-74, there is 1.2 eV shift to higher binding energy region of Ni(Fe)-MOF/KB. A similar interaction behavior has been also observed for Ni(Fe)$(OH)_2$/KB due to the shift to higher binding energy. However, this shift was 0.1 eV for Ni 2p spectra and 0.7 eV for Fe 2p spectra indicating less interactions of Ni(Fe)$(OH)_2$ with KB compared to Ni(Fe)-MOF-74 with KB. TEM and SEM investigations revealed that the Ni(Fe)-MOF-74 particles are surrounded by spherical KB carbon and in some occasions it is visible that this carbon layer glues MOF particles together. After detailed characterization, all materials were tested for electrochemical OER. Among all materials, Ni(Fe)-MOF/KB displayed a remarkable OER performance by requiring 274 mV overpotential to reach 10 mA/cm^2, 650 mA/cm^2 current density at an applied voltage of 1.7 V_{RHE} and having a small Tafel slope of 40.4 mV/dec. This activity outperforms the pristine Ni(Fe)-MOF-74, Ni(Fe)$(OH)_2$, Ni(Fe)$(OH)_2$/KB and many other reported OER catalysts including commercial ones. Both composite materials, namely Ni(Fe)-MOF/KB and Ni(Fe)$(OH)_2$/KB, showed better OER performance than their individual components. This enhanced performance can be attributed to the iron elements that homogeneously distributed over the Ni-MOF-74, and the introduction of the highly conductive and porous carbon material ketjenblack (KB) that provided the solution to overcome the intrinsic drawbacks of MOF for electrocatalysis, in particular (i) a low electrical conductivity, (ii) a predominant microporosity disturbing a permeability of electrolyte ions into pores and a mass transfer of evolved gases from inner pores to bulk electrolyte, and (iii) a poor wettability. The stability test also displayed the very good stability of Ni(Fe)-MOF/KB during 12 hours. As a result, this methodology for MOF-based OER electrocatalyst with high activity does not require any energy-intensive procedures or noble metals and can be applied for water splitting systems based on solar cells, photoelectrochemical cells, and photocatalysis.

7. Experimental Part

7.1 General

All chemicals were purchased from commercial suppliers and used without further purification, unless stated otherwise. Utilized solvents were obtained from chemical sources and used as received. MOFs were synthesized using an oven from Memmert which is equipped with programmable temperature ramps.

Table 5. List of all used chemicals and solvents.

Chemicals	Purity	Source
$Co(OAc)_2.4H_2O$	> 99.9 %	Sigma-Aldrich
1,4-Dicyanobenzene	> 98 %	Sigma-Aldrich
2,5-dihydroxyterephthalicacid	> 98 %	TCI
$Fe(CO_2CO_3)_2$	> 99.9 %	Sigma-Aldrich
$Ni(NO_3)_2.6H_2O$	> 99.9 %	Sigma-Aldrich
Zinc chloride	> 98 %	Alfa Aesar
Solvents		
Acetone	> 99 %	Fischer Chemicals
Ammonia	25 %	VWR
N,*N*-Dimethylformamide	> 99.5 %	Fisher Chemical
Ethanol	> 99.8 %	Fisher Chemical
HCl	37 %	VWR
Tetrahydrofuran (THF)	> 99.7 %	Fischer Chemicals

7.2 Analytical Methods

Powder X-ray diffraction

Powder X-ray diffraction (PXRD) patterns were collected at ambient temperature on a Bruker D2 phaser diffractometer (300 W, 30 kV, 10 mA) using Cu Kα1/α2 radiation with $\lambda = 1.5418$ Å at 30 kV covering $5° < 2\theta < 100°$. The diffractograms were obtained on a low background flat silicon sample holder. The evaluation of the diffractograms was done with Match software.

Nitrogen sorption analysis

The nitrogen sorption measurements were carried out at 77K with a Quantachrome NOVA 4000e gas sorption analyzer with the NovaWin 11.03 software. The samples were first degassed under vacuum at the desired temperature for 15 hours. BET surface areas were calculated from the nitrogen adsorption isotherms applying Roquerol plot. Total pore volumes were determined from the nitrogen sorption isotherm at around $p/p_0 = 0.95$.

Thermogravimetric analysis

The thermogravimetric analyses were carried out on a TG 209 F3 Tarsus from Netzsch with a ramping rate of 5 K/min under N_2 flow.

Elemental analysis

Elemental (CNH) analyses were carried out with a PerkinElmer 2400 series 2 elemental analyser.

Scanning electron microscopy

Scanning electron microscopic (SEM) images were recorded on a Jeol JSM-6510LV QSEM equipped with a LaB_6 cathode. The microscope was also equipped with a Bruker Xflash 410 silicon drift detector and the Bruker ESPRIT software for energy dispersive X-ray (EDX) analysis which is used to record EDX spectra and EDX mapping. The samples were prepared for SEM by coating with a gold layer through sputtering for 20 seconds.

7.3 Synthesis of Materials

All synthetic procedures described here are related to the unpublished results. The synthesis procedures from the cumulative part are described in the corresponding publications.

Synthesis of Ni-MOF-74

The synthetic procedure was followed according to the literature[117]. Ni-MOF-74 was synthesized according to the literature with slight modifications. $Ni(NO_3)_2 \cdot 6H_2O$ (132 mg, 0.45 mmol) and 2,5-dihydroxyterephthalicacid (30 mg, 0.15 mmol) were mixed in 10 ml DMF, 0.6 ml EtOH and 0.6 ml H_2O and stirred at room temperature to obtain a homogeneous solution. This mixture was transferred into an autoclave and heated to 120 °C for 24h. After that, the sample was washed with DMF and EtOH for several days and dried at 100 °C for 24 h.

Synthesis of Fe-Ni-MOF-74

The synthesis of Fe-Ni-MOF-74 with different atomic metal ratios were done under the same conditions as the synthesis of Ni-MOF-74. Typically, $Fe(OAc)_2$ and $Ni(NO_3)_2 \cdot 6H_2O$ with different molar ratios (total molar concentration was 0.45 mmol) were mixed with 2,5-dihydroxyterephthalicacid (0.15 mmol) in 10 ml DMF, 0.6 ml EtOH and 0.6 ml H_2O and transferred to an autoclave after it was homogeneous solution. Then, it was heated to 120 °C for 24h. Following the reaction, materials were washed first with DMF and then EtOH for several days. Later they were dried under vacuum at 100 °C for 24 h.

Synthesis of MOF Derivatives

The obtained Ni-MOF-74 and Fe-Ni-MOF-74 with different metallic molar ratios were placed in porcelain crucibles and transferred to an electric muffle furnace to be heated either at 350 °C for 2h, 350°C for 5h or 500 °C for 4h under air atmosphere.

Synthesis of CTF-1

The synthetic procedure was followed according to the literature[45]. CTF-1 was synthesized by the ionothermal method. First 1.28 g (10 mmol) dicyanobenzene and 6.8 g (50 mmol) anhydrous $ZnCl_2$ were mixed in a Duran® glass ampoule under inert atmosphere. This ampule was evacuated by vacuum and then flame sealed. The ampule was heated in an oven at 400 °C for 48h and then cooled down to ambient temperature. Resulted black product was first grounded and then washed with Millipore® water for 72h. Washing process continued with diluted HCl (0.1 mol/L), Milipore water, tetrahydrofuran (THF) and acetone. Following the washing, the resulted product was dried under high vacuum at 120 °C for 12h.

Synthesis of Co_3O_4/CTF-1

The synthetic procedure was followed according to the literature[118]. $Co(OAc)_2.4H_2O$ (250 mg) was first dissolved in water (30 ml) and then 1.5 ml ammonia (20%) was added. Following 250 mg CTF-1 was added to this solution. This mixture was heated to 80 °C for 10 h then it was transferred into autoclave which was hold at 150 °C for 3h. The resulted product was washed first with H_2O and then with EtOH for several times and afterwards dried at 60 °C for 12h.

References

---

[1] International Energy Agency, *World Energy Outlook* **2010**

[2] T. J. Meyer, *Acc. Chem. Res.* **1989**, *22*, 163-170.

[3] A. J. Bard, M. A. Fox, *Acc. Chem. Res.* **1995**, *28*, 141-145.

[4] M. G. Walter, E. L. Warren, J. R. McKone, S. W. Boettcher, Q. Mi, E. A. Santori, N. S. Lewis, *Chem. Rev.*, **2010**, *110*, 6446-6473.

[5] R. de Levie, *Journal of Electroanalytical Chemistry*, **1999**, *476*, 92-93.

[6] R. L. Leroy, *Int. J. Hydrogen Energy*, **1983**, *8*, 401-417.

[7] S. Farid, S. Ren, C. Hao, *Inorganic Chemistry Communications*, 2018, *94*, 57-74.

[8] Y. Lee, J. Suntivich, K. J. May, E. E. Perry, Y. Shao-Horn, *J. Phys. Chem. Lett.*, **2012**, *3*, 399-404.

[9] T. Nakagawa, N. S. Bjorge, R. W. Murray, *J. Am. Chem. Soc.*, **2009**, *131*, 15578-15579.

[10] Q. Shi, C. Zhu, D. Du, Y. Lin, *Chem. Soc. Rev.*, **2019**, *48*, 3181-3192.

[11] S. Anantharaj, K. Karthick, M. Venkatesh, T. V. S. V. Simha, A. S. Salunke, L. Ma, H. Liang, S. Kundu, *Nano Energy*, **2017**, *39*, 30-43.

[12] R. Chen, H. Y. Wang, J. Miao, H. Yang, B. Liu, *Nano Energy*, **2015**, *11*, 333-340.

[13] Y. Meng, W. Song, H. Huang, Z. Ren, S. Y. Chen, S. L. Suib, *J. Am. Chem. Soc.*, **2014**, *136*, 11452-11464.

[14] L: Zhang, J. Xiao, H. Wang, M. Shao, *ACS Catal.*, **2017**, *7*, 7855-7865.

[15] M. Tahir, N. Mahmood, L. Pam, Z. F. Huang, Z. Lv, J. Zhang, F. K. Butt, G. G. Shen, X. Zhang, S. X. Dou, J. J. Zou, *J Mater. Chem. A*, **2016**, *4*, 12940-12946.

[16] F. Song, L. Bai, A. Moysiadou, S. Lee, C. Hu, L. Liardet, X. Hu, *J. Am. Chem. Soc.*, **2018**, *140*, 7748-7759.

[17] Y. Wang, T. Zhou, K. Jiang, P. Da, Z. Peng, J. Tang, B. Kong, W. B. Cai, Z. Yang, G. Zheng, *Adv. Energy Mater.*, **2014**, *4*, 1400696.

[18] D. A. Corrigan, R. M. Bendert, *J. Electrochem. Soc.*, **1989**, *136*, 723-728.

[19] Y. Li, P. Hasin, Y. Wu, *Adv. Mater.* **2010**, *22*, 1926-1929.

[20] A. J. Bard and L. R. Faulkner, Electrochemical methods: fundamentals and applications, Wiley, 1980.

[21] J. O. Bockris, A. K. N. Reddy and M. Gamboa-Aldeco, Modern Electrochemistry 2A. Fundamentals of Electrodics, Kluwer Academic, New York, 2000.

[22] S. Anantharaj, S. R. Ede, K. Karthick, S. S. Sankar, K. Sangeetha, P. E. Karthik, S. Kundu, *Energy Environ. Sci.*, **2018**, *11*, 744.

[23] C. C. L. McCrory, S. Jung, I. M. Ferrer, S. M. Chatman, J. C. Peters, T. F. Jaramillo, *J. Am. Chem. Soc.*, **2015**, *137*, 4347 -4357.

[24] K. S. W. Sing, D. H. Everett, R. A. W. Haul, L. Moscou, R. A. Pierotti, J. Rouquérol, T. Siemieniewska, *Pure Appl. Chem.* **1985**, *57*, 603-619.

[25] G. Q. Lu, X. S. Zhao, *Nanoporous Materials: Science and Engineering, Vol. 4*, Impirial College Press, London, UK, **2006.**

[26] Z. Chang, D. S. Zhang, Q. Chen, X. H. Bu, *Phys. Chem. Chem. Phys.* **2013**, *15*, 5430-5442.

[27] R. Dawson, E. Stöckel, j. R. Holst, D. J. Adams, A. I. Cooper, *Energy Environ. Sci.*, **2011**, *4*, 4239-4245.

[28] P. Kaur, J. T. Hupp, S. T. Nguyen, *ACS Catal.*, **2011**, *1*, 819-835.

[29] C. Xu, W. Zhang, J. Tang, C. Pan, G. Yu, *Front Chem.*, **2018**, *6*, 592.

[30] S. Dalapati, S. Jin, J. Gao, Y. Xu, A. Nagai, D. Jiang, *J. Am. Chem. Soc.* **2013**, *135*, 17310-17313.

[31] D. Yuan, W. Lu, D. Zhao, H. C. Zhou, *Adv. Mater.*, **2011**, *23*, 3723-3725.

[32] X. Chen, N. Huang, J. Gao, H. Xu, F. Xu, D. Jiang, *Chem. Commun.*, **2014**, *50*, 6161-6163.

[33] X. Zou, H. Ren, G. Zhu, *Chem. Commun.*, **2013**, *49*, 3925-3936.

[34] R. Dawson, A. I. Cooper, D. J. Adams, *Progress in Polymer Science*, **2012**, *37*, 530-563.

---

[35] A. P. Cote, A. I. Benin, N. W. Ockwig, M. O'Keeffe, A. J. Matzger, O. M. Yaghi, *Science*, **2005**, *310*, 1166-1170.

[36] H. M. El-Kaderi, J. R. Hunt, J. L. Mendoza-Cortes, A. P. Cote, R. E. Taylor, M. O'Keeffe, O. M. Yaghi, *Science*, **2007**, *316*, 268-272.

[37] P. Kuhn, M. Antonietti, A. Thomas, Angew. *Chem., Int. Ed.*, **2008**, *47*, 3450-3453.

[38] Y. Xu, S. Jin, H. Xu, A. Nagai, D. Jiang, *Chem. Soc. Rev.*, **2013**, *42*, 8012-8031.

[39] T. Ben, S. Qiu, *CrystEngComm*, **2013**, *15*, 17-26.

[40] M. P. Tsyurupa, V. A. Davankov, *React. Funct. Polym.*, **2006**, *66*, 768-779.

[41] W. G. Toland (California Research Corporation), US 3060179, **1962**.

[42] G. H. Miller (Texaco Inc.), US 3775380, **1973**.

[43] J. Artz, *ChemCatChem*, **2018**, *10*, 1753-1771.

[44] C. Krishnaraj, H. S. Jena, K. Leus, P. Van Der Voort, *Green Chem*, **2020**, *22*, 1038-1071.

[45] P. Kuhn, A. Forget, D. Su, A. Thomas, M. Antonietti, *J. Am. Chem. Soc.*, **2008**, *130*, 13333-13337.

[46] S. Ren, M. J. Bojdys, R. Dawson, A. Laybourn, Y. Z. Khimyak, D. J. Adams, A. I. Cooper, *Adv. Mater.*, **2012**, *24*, 2357-2361.

[47] S. Dey, A. Bhunia, D. Esquivel, C. Janiak, *J. Mater. Chem. A.*, **2016**, *4*, 6259-6263.

[48] S. Y. Yu, J. Mahmood, H. J. Noh, J. M. Seo, S. M. Jung, S. H. Shin, Y. K. Im, I. Y. Jeon, J. B. Baek, *Angew. Chem., Int. Ed.*, **2018**, *57*, 8438-8442.

[49] P. Kuhn, A. Thomas, M. Antonietti, *Macromolecules*, **2009**, *42*, 319-326.

[50] L. Hao, S. Zhang, R. Liu, J. Ning, G. Zhang, L. Zhi, *Advanced Materials*, **2015**, *27*, 3190-3195.

[51] Y. Zhao, K. X. Yao, B. Teng, T. Zhang, Y. Han, *Energy Environ. Sci.*, **2013**, *6*, 3684-3692.

[52] S. Ren, M. J. Bojdys, R. Dawson, A. Laybourn, Y. Z. Khimyak, D. J. Adams, A. I. Cooper, *Adv. Mater.* **2012**, *24*, 2357-2361.

[53] A. Bhunia, V. Vasylyeva, C. Janiak, *Chem. Commun.* **2013**, *49*, 3961-3963.

[54] A. Bhunia, I. Boldog, A. Moller, C. Janiak, *J. Mater. Chem. A*, **2013**, *1*, 14990-14999.

[55] W. Zhang, C. Li, Y.-P. Yuan, L.-G. Qiu, A.-J. Xie, Y.-H. Shen, J.-F. Zhu, *J. Mater. Chem.* **2010**, *20*, 6413-6415.

[56] W. Zhang, F. Liang, C. Li, L. G. Qiu, Y. P. Yuan, F. M. Peng, X. Jiang, A. J. Xie, Y. H. Shen, J. F. Zhu, *J. Hazard. Mater*. **2011**, *186*, 984-990.

[57] J. Liu, E. Zong, H. Fu, S. Zheng, Z. Xu, D. Zhu, *J. Colloid Interface Sci*. **2012**, *372*, 99-107.

[58] A. Bhunia, S. Dey, M. Bous, C. Zhang, W. von Rybinski, C. Janiak, *Chem. Commun*. **2015**, *51*, 484-486.

[59] X. Wang, C. Zhang, Y. Zhao, S. Ren, J X. Jiang, *Macromol. Rapid Commun.*, **2016**, *37*, 323-329.

[60] S. Dey, S. Bügel, S. Sorribas, A. Nuhnen, A. Bhunia, J. Coronas, C. Janiak, *Front. Chem*. **2019**, *7*, 693.

[61] H. Liao, H. Ding, B. Li, X. Ai, C. Wang, *J. Mater. Chem A.*, **2014**, *2*, 8854-8858.

[62] Y. Li, S. Zheng, X. Liu, P. Li, L. Sun, R. Yang, S. Wang, Z. S. Wu, X. Bao, W. Q. Deng, *Angew. Chem. Int. Ed.*, **2018**, *57*, 7992-7996.

[63] J. Roeser, K. Kailasam, A. Thomas, *ChemSusChem*, **2012**, *5*, 1793-1799.

[64] X. Jiang, P. Wang, J. Zhao, *J. Mater. Chem. A*, **2015**, *3*, 7750-7758.

[65] L. Li, W. Fang, P. Zhang, J. Bi, Y. He, J. Wang, W. Su, *J. Mater. Chem. A* **2016**, *4*, 12402-12406.

[66] A. Bhunia, D. Esquivel, S. Dey, R. Fernandez-Teran, Y. Goto, S. Inagaki, P. van der Voort, C. Janiak, *J. Mater. Chem. A* **2016**, *4*, 13450-13457.

[67] S. Kuecken, A. Acharjya, L. Zhi, M. Schwarze, R. Schomäcker, A. Thomas, *Chem. Commun*. **2017**, *53*, 5854-5857.

[68] R. K. Yadav, A. Kumar, N. J. Park, K. J. Kong, J. O. Baeg, *J. Mater. Chem. A* **2016**, *4*, 9413-9418.

[69] F. Niu, L. Tao, Y. Deng, H. Gao, J. Liu, W. Song, *New J. Chem*. **2014**, *38*, 5695-5699.

[70] J. Liu, Y. Hu, J. Cao, *Catal. Commun*. **2015**, *66*, 91-94.

---

[71] L. Ji, Y. Hu, H. Ju, C. Wang, M. R. Gao, Q. Yang, J. Zhu, S. H. Yu, H. L. Jiang, *J. Mater. Chem. A* **2017**, *5*, 23170-23178.

[72] S. Gopi, M. Kathiresan, *Polymer* **2017**, *109*, 315-320.

[73] Y. Wang, J. Chen, G. Wang, Y. Li, Z. Wen, *Angew. Chem. Int Ed*., **2018**, *57*, 13120-13124.

[74] R. Palkovits, M. Antonietti, P. Kuhn, A. Thomas, F. Scheth, *Angew. Chem. Int. Ed*. **2009**, *48*, 6909-6912.

[75] S. Hug, M. E. Tauchert, S. Li, U. E. Pachmayr, B. V. Lotsch, *J. Mater. Chem*., **2012**, *22*, 13956-13964.

[76] C. E. Chan-Thaw, A. Villa, P. Katekomol, D. Su, A. Thomas, L. Prati, *Nano Lett*., **2010**, *10*, 537-541.

[77] M. Siebels, C. Schlüsener, J. Thomas, Y. X. Xiao, X. Y. Yang, C. Janiak, *J. Mater. Chem. A*, **2019**, *7*, 11934-11943.

[78] K. Kamiya, R. Kamai, K. Hashimoto, S. Nakanishi, *Nat. Commun*. **2014**, 5, 5040.

[79] K. Iwase, T. Yoshioka, S. Nakanishi, K. Hashimoto, K. Kamiya, *Angew. Chem. Int. Ed*. **2015**, *54*, 11068-11072.

[80] Q. Zuo, P. Zhao, W. Luo, G. Cheng, *Nanoscale* **2016**, *8*, 14271-14277.

[81] S. R. Batten, N. R. Champness, X.-M. Chen, J. Garcia-Martinez, S. Kitagawa, L. Ohrstrom, M. O'Keeffe, M. P. Suh, J. Reedijk, J. *Pure Appl. Chem.,* **2013**, 85*,* 1715–1724.

[82] C. Janiak, J. K. Vieth, *New J. Chem*., **2010**, 34, 2366–2388.

[83] B. F. Hoskins, R. Robson, *J. Am. Chem. Soc.,* **1989**, 111, 5962–5964.

[84] B. F. Hoskins, R. Robson, *J. Am. Chem. Soc.,* **1990**, 112, 1546–1554.

[85] O.M. Yaghi, H. Li, *J. Am. Chem. Soc.* **1995**, 117, 10401–10402.

[86] M. Kondo, T. Yoshitomi, H. Matsuzaka, S. Kitagawa, K. Seki, *Angew. Chem. Int. Ed,.* **1997**, 36, 1725–1727.

[87] S.S Chui, S- M.-F. Lo, J. P. H. Charmant, A. G. Orpen, I. D. Williams, *Science,* **1999**, 283, 1148–1150.

[88] O. M. Yaghi, H. Li, M. Eddaoudi, M. O'Keeffe, *Nature,* **1999**, 402, 276–279.

[89] H. Furukawa, N. Ko, Y. B. Go, N. Aratani, S. B. Choi, E. Choi, A. Ö. Yazaydin, R. Q. Snurr, M. O'Keeffe, L. Kim, O. M. Yaghi, *Science,* **2010**, 329, 424–428.

[90] A. Schneemann, S. Henke, I. Schwedler, R. A. Fischer, *ChemPhysChem* **2014**, *15*, 823-839.

[91] A. J. Fletcher, K. M. Thomas, M. J. Rosseinsky, *J. Solid State Chem*. **2005**, *178*, 2491-2510.

[92] W. Xuan, C. Zhu, Y. Liu, Y. Cui, *Chem. Soc. Rev*., **2012**, *41*, 1677–1695.

[93] S. Horike, S. Shimomura and S. Kitagawa, *Nature Chem*., **2009**, *1*, 695–704.

[94] N. Stock and S. Biswas, *Chem. Rev*., **2012**, 112, 933–969.

[95] M. P. Suh, H. J. Park, T. K. Prasad, D.-W. Lim, *Chem. Rev.* **2012**, *112*, 782-835.

[96] J. A. Mason, M. Veenstra, J. R. Long, *Chemical Science* **2014**, *5*, 32-51.

[97] K. Sumida, D. L. Rogow, J. A. Mason, T. M. McDonald, E. D. Bloch, Z. R. Herm, T.-H. Bae, J. R. Long, *Chem. Rev.* **2012**, *112*, 724-781.

[98] A. Nuhnen, D. Dietrich, S. Millan, C. Janiak, *ACS Appl. Mater. Interfaces*, **2018**, *10*, 33589-33600.

[99] P. Horcajada, R. Gref, T. Baati, P. K. Allan, G. Maurin, P. Couvreur, G. Férey, R. E. Morris, C. Serre, *Chem. Rev.* **2012**, *112*, 1232-1268.

[100] L. E. Kreno, K. Leong, O. K. Farha, M. Allendorf, R. P. Van Duyne, J. T. Hupp, *Chem. Rev.* **2012**, *112*, 1105-1125.

[101] M. D. Allendorf, A. Schwartzberg, V. Stavila, A. A. Talin, *Chemistry - A European Journal* **2011**, *17*, 11372-11388.

[102] V. Stavila, A. A. Talin, M. D. Allendorf, *Chem. Soc. Rev.* **2014**, *43*, 5994-6010.

[103] Jeremias, F.; Khutia, A.; Henninger, S. K.; Janiak, C. *J. Mater. Chem.* **2012**, *22*, 10148-10151.

[104] J. Y. Lee, O. K. Farha, J. Roberts, K. A. Scheidt, S. B. T. Nguyen, J. T. Hupp, *Chem. Soc. Rev.* **2009**, *38*, 1450-1459.

[105] Q Yang, Q. Xu, S. H. Yu, H. L. Jiang, *Angew. Chem. Int. Ed*., **2016**, *55*, 3685-3689.

---

[106] L. Zeng, X. Guo, C. He, C. Duan, *ACS Catal*., **2016**, *6*, 7935-7947.

[107] A. Mahmood, W. Guo, H. Tabassum, R. Zou, *Adv. Energy Mater*. **2016**, *6*, 1600423-1600449.

[108] C. Liao, Y. Zuo, W. Zhang, J. Zhao, B. Tang, A. Tang, Y. Sun, J. Xu, *Russ. J. Electrochem*., **2012**, *49*, 983–986.

[109] X. Sun, G. Gao, D. Yan and C. Feng, *Appl. Surf. Sci*., **2017**, *405*, 52–59.

[110] H. Zhong, K. H. Ly, M. Wang, Y. Krupskaya, X. Han, J. Zhang, J. Zhang, V. Kataev, B. Buchner, I. M. Weidinger, S. Kaskel, P. Liu, M. Chen, R. Dong, X. Feng, *Angew. Chem. Int. Ed*. **2019**, *58*, 10677–10682.

[111] S. Zhao, Y. Wang, J. Dong, C.T. He, H. Yin, P. An, K. Zhao, X. Zhang, C. Gao, L. Zhang, J. Lv, J. Wang, J. Zhang, A. M. Khattak, N. A. Khan, Z. Wie, J. Zhang, S. Liu, H. Zhao, Z. Tang, *Nature Energy*, **2016**, 1, 16184.

[112] F. Yin, G. Li, H. Wang, *Catal. Commun*., **2014**, *54*, 17-21.

[113] M. Jahan, Z. Liu, K. P. Loh, *Adv. Funct. Mater.* **2013**, *23*, 5363-5372.

[114] H. Wang, F. X. Yin, B. H. Chen, X. B. He, P. L. Lv, C. Y. Ye, D. J. Liu, *Appl. Catal. B*, **2017**, 205, 55–67.

[115] S. Bhattacharyya, C. Das, T. K. Maji, *RSC Adv*., **2018**, *8*, 26728-26754.

[116] Y. Hou, J. Li, Z. Wen, S. Cui, C. Yuan, J. Chen, *Nano Energy* **2015** ,*12*, 1-8.

[117] L. J. Wang, H. Deng, H. Furukawa, F. Gandara, K. E. Cordova, D. Peri, O. M. Yaghi, *Inorg. Chem.* **2014**, *53*, 5881-5883.

[118] S. Chen, Y. Zhu, D. Xu, W. Peng, Y. Li, G. Zhang, F. Zhang, X. Fan, *Chemelectrochem*, **2018**, *5*, 717-721.